Study of a Wideband Sinuous Feed for Reflector Antenna Applications

by

Ngoy Mutonkole

Thesis presented in partial fulfilment of the requirements for the degree of Master of Engineering in Electrical and Electronic Engineering in the Faculty of Engineering at Stellenbosch University

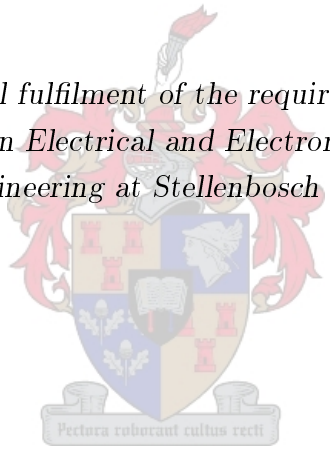

Department of Electrical and Electronic Engineering,
University of Stellenbosch,
Private Bag X1, Matieland 7602, South Africa.

Supervisor: Dr. Dirk I.L. de Villiers

December 2013

Declaration

By submitting this thesis electronically, I declare that the entirety of the work contained therein is my own, original work, that I am the sole author thereof (save to the extent explicitly otherwise stated), that reproduction and publication thereof by Stellenbosch University will not infringe any third party rights and that I have not previously in its entirety or in part submitted it for obtaining any qualification.

Date: December 2013 .....

Abstract

Study of a Wideband Sinuous Feed for Reflector Antenna Applications

N. Mutonkole

Department of Electrical and Electronic Engineering,
University of Stellenbosch,
Private Bag X1, Matieland 7602, South Africa.

Thesis: MEng (EE)

December 2013

This thesis presents a thorough study of the printed sinuous antenna and its characterisation as a feed for reflector antenna applications. Two different techniques are used in this study, namely a parametric study and an efficient surrogate based optimisation strategy.

A planar sinuous antenna over a reflecting ground plane, with no absorber lining, is designed following a parameter study from which effective design guidelines are derived. The designed prototype displays a bandwidth ratio of more than $3:1$ from $1.9-6.2$ GHz, at a measured return loss of 10 dB, representing a significant improvement over the octave band previously achieved with a similar antenna.

An optimisation based approach is followed in formally investigating a conical sinuous antenna over a reflecting ground plane. An efficient surrogate based optimisation strategy, in which the antenna's response is approximated by a Kriging model, is used. The search for optimal design parameters as well as improvements in the accuracy of the Kriging model is accomplished by using expected improvement as the infill sampling criterion. The antenna is optimised for return loss, aperture efficiency for a prime-focus paraboloid reflector as well as cross-polarisation and results from the optimisation are used to derive effective design guidelines and performance limitations. The investigations are conducted for the $2-6$ GHz band and the obtained results can be easily applied for designs with wider bandwidths. Simulation results reveal improved return loss, aperture efficiency and cross-polarisation performances compared to what has previously been reported for this antenna.

Uittreksel

Study of a Wideband Sinuous Feed for Reflector Antenna Applications

N. Mutonkole

Departement Elektriese en Elektronies Ingenieurswese,
Universiteit van Stellenbosch,
Privaatsak X1, Matieland 7602, Suid Afrika.

Tesis: MIng (EE)

Desember 2013

Hierdie tesis bied 'n deeglike studie van die gedrukte stroombaanbord sinuous antenna, sowel as die karakterisering daarvan as voer vir reflektor antenna toepassings. Twee verskillende tegnieke word gebruik, naamlik 'n parametriese studie en 'n surrogaat-gebaseerde optimering strategie.

Effektiewe doeleindes vir die ontwerp is van 'n parameter studie afgelei, waarvolgends 'n planêre sinuous antenna met 'n weerkaatsingsgrondvlak ontwerp is sonder enige absorberende materiale. Die prototipe vertoon beter as 'n $3:1$ bandwydte van 1.9 GHz tot 6.2 GHz teen 'n gemete weerkaatsingskoëffisiënt van beter as -10 dB, wat dui op 'n aansienlike verbetering teenoor die oktaaf bandwydte wat voorheen met 'n soorgelyke antenna bereik is.

'n Optimering-gebaseerde benadering is gebruik om ondersoek in te stel in die gebruik van 'n koniese sinuous antenna met 'n weerkaatsingsgrondvlak. 'n Doeltreffende surrogaat-gebaseerde optimeering strategie is gebruik, waar die antenna se weergawe deur 'n Kriging model benader word. Die verwagte verbetering is gebruik as maatstaf in die soektog vir optimale ontwerpsparameters, sowel as om die akkuraatheid van die Kriging model te verbeter. Die antenna is geoptimeer vir sy weerkaatsingskoëffisiënt, stralingsvlak effektiwiteit for 'n paraboloïed antenna sowel as kruispolarisasie. Resultate van die optimering is gebruik om effektiewe riglyne vir die ontwerp en grense vir die werkverrigting op te stel. Die antenna is ondersoek vir die 2 tot 6 GHz frekwensieband en die resultate wat verkry is kan maklik op ontwerpe met selfs wyer bandwydtes toegepas word. Simulasie resultate dui op 'n verbetering in weerkaatsingskoëffisiënt, stralingsvlak effektiwiteit en kruispolarisasie in vergelyking met wat berig is vir hierdie antenna.

Acknowledgements

My first words of gratitude go to *Dirk*, my supervisor, for being so helpful and supportive from the time I expressed interest in doing a masters under his guidance. I have been greatly inspired by your humble nature, brilliance and attention to detail. Thanks for enduring all the, sometimes not so smart, questions I had, for all the good ideas and the intellectual freedom I enjoyed throughout the project. Thanks for all the invaluable lessons and for making me a better researcher (by several orders of magnitude). I couldn't have asked for a better supervisor!

Many thanks to all my colleagues in the penthouse: *Dr. Braam Otto, Dr. Renier Marchand, Dr. André Young, Nicholas Thompson, JP, Vereese, Lee, Jacki* and *Necmi* for setting the right working environment. Thanks to *Braam* for all the FEKO related help and for letting me run a few simulations on the CHPC cluster, *André* for all the advice on technical stuff and *Nicholas* for sorting out most of my computer related issues.

Many thanks to my compadres in E 206: *Samaneh Movahedian, Shamim Omar Nassar, David Prinsloo and Theunis Beukman* for all the help and discussions, and for accommodating my coffee habits. Thanks to *Theunis* for all the useful ideas and for insisting on focussing on the big picture during our collaboration. Thanks to *Shamim* for being either technical or caring depending on the circumstance and for being such an inspiration! Thanks to *David* for being a consistent source of problem solving ideas ever since my skripsie days (thanks for every thing...). Thanks to *Samaneh* for being my very good friend and for all the awesome discussions (unrelated to engineering)! I appreciate all you have done for me and wish you guys all the best with the rest of your studies.

My family for always being supportive and for everything that I am today. This is for you!

I also want to thank *Juliane Müller* for promptly replying to all my emails and for detailed discussions that made my encounter with Expected Improvement and Kriging much easier to handle. *Ryno Beyers*, for his help with complex programming tasks, translating my abstract and generously handling the admin side of our planned trip to the European Microwave Week in Germany.

A big thank you to Mr. *Wessel Croukamp* for manufacturing the antenna model, *Antenna Magus* for the personal license to their antenna software.

Last but not least, financial assistance from the National Research Foundation (NRF) of South Africa is hereby acknowledged. This project would not have been possible without the NRF and I hereby wish to thank all the staff in charge of the SKA bursaries at the NRF for a hassle-free two years.

Dedications

To José, my mom, Helène and Thérèse my aunts and to my siblings: Mimo, Pypo, Yannick, Jolaine and Erico.

In memory of my late father Dr. Mutonkole: Thanks for ensuring we all got an education!

Contents

List of Figures

List of Tables

Nomenclature

ARE	Average Relative Error
ANN	Artificial Neural Networks
ATA	Allen Telescope Array
BOR_1	Body Of Revolution type−1
CDF	Cumulative Distribution Function
CEM	Computation ElectroMagnetics
DACE	Design and Analysis of Computer Experiments
DIRECT	DIviding RECTangles
EM	ElectroMagnetics
EI	Expected Improvement
GA	Genetic Algorithm
GP	Gaussian Process
HPBW	Half-Power Beam Width
HPC	High Performance Computation
KKT	Karush - Kuhn - Tucker
LHS	Latin Hypercube Sampling
LNA	Low Noise Amplifier
LP	Log Periodic
LPDA	Log Periodic Dipole Array
LSA	Local Sensitivity Analysis
MLCS	Multi-Level Coordinate Search
MLE	Maximum Likelihood Estimates
MoM	Method of Moments
MRE	Mean Relative Error
MSE	Mean Square Error
NSGA-II	Non-dominated Sorting Genetic Algorithm-II
PDF	Probability Density Function
PoI	Probability of Improvement
PSO	Particle Swarm Optimisation
QRFH	Quadruple Ridged Flared Horn

QSC	Quasi-Self Complementary
RBF	Radial Basis Function
RRSE	Root Relative Square Error
SBO	Surrogate Based Optimisation
SKA	Square Kilometre Array
SM	Space Mapping
SQP	Sequential Quadratic Programming
SVM	Support Vector Machine
UWB	Ultra - Wide Band
X-Pol	Cross - polarisation
XPD	Cross - polarisation Discrimination

Chapter 1

Introduction

> Nothing I guess, I do not think that the wireless waves I have discovered will have any practical application.
>
> Heinrich Hertz, 1886-87

Several aspects of our lives are deeply intertwined with applied electromagnetics. One aspect of applied electromagnetics that has come to redefine modern civilisation, is telecommunication. Indeed, telecommunication defines the way modern business, transportation, astronomy and even medicine are conducted, generally achieving what was previously thought impossible in a cost effective manner. At the core of the revolution in telecommunications, is the rapid development of antennas for a multitude of applications. Antennas constitute the front end of any telecommunication system and have been studied since the experiments of Heinrich Hertz.

The increasing number of commercial applications of ultra-wideband (UWB) communication as well as advances in radio astronomy, such as the Square Kilometre Array (SKA) [4] and MeerKAT [5] radio telescope projects, have renewed interest in antennas with wide instantaneous bandwidth. The advantages of such antennas are fast data rates for UWB communication[1] and large survey speeds[2] for radio telescopes as well as reduced cost as only one feed is required to cover a large bandwidth.

UWB communications mostly use wideband antennas as direct radiating elements while wideband antennas are used as feeds for reflector systems in modern radio astronomy.

1.1 State of the Art Wideband Feeds

Wideband feeds for high fidelity applications such as radio astronomy are required to achieve performances (radiation characteristics as well as input reflections) similar to a corrugated horn over a very wide bandwidth.

[1] A direct result of the Shannon-Hartley theorem where channel capacity is directly proportional to bandwidth.

[2] Also directly proportional to bandwidth.

The performance characteristics of a corrugated horn are:

1. Almost Gaussian, circularly symmetric radiation pattern with a controllable beamwidth.
2. Very little pattern variation with frequency.
3. Very low side lobes and cross-polarisation levels.
4. Constant phase centre with frequency.

Several log-periodic (LP) feeds have been developed over the years to meet the above requirements. These include the eleven feed [6] designed for the $2-13$ GHz band, the quasi self-complimentary (QSC) feed [7] designed for $0.4-4$ GHz, the log periodic dipole array feed for the ATA radio telescope [8] with over a decade bandwidth, the conical sinuous antenna [9] experimentally demonstrated for the $1-3$ GHz bandwidth, but could easily be extended to cover over a decade bandwidth and the quad-ridge flared horn antenna with a demonstrated bandwidth ratio of up to $7:1$ [10]. A summary of the mentioned feeds is given in Table 1.1 [10].

Table 1.1: Performance summary of wideband single pixel reflector antenna feeds.

Feed	Pattern features	Impedance	Bandwidth
Eleven feed	Circular beam with constant beamwidth, stable phase centre, mediocre relative x-pol	200 Ω diff.	7 : 1
QSC feed	Circular beam with constant beamwidth, stable phase centre, poor relative x-pol	200 Ω diff.	10 : 1
ATA feed	Circular beam with constant beamwidth, large phase centre variation, poor relative x-pol	200 Ω diff.	10 : 1
Sinuous feed	Beamwidth variation, elliptical beam, stable phase centre, poor relative x-pol	260 Ω diff.	3 : 1
QRFH feed	Beamwidth stability, small phase centre variation, mediocre relative x-pol	50 Ω	5 : 1 to 7 : 1

It is clear from Table 1.1 above, that all mentioned feeds have short comings as far as achieving performances similar to a corrugated horn is concerned. There is thus need to further investigate and improve upon these wideband feeds, especially in the context of the SKA where potential cost savings are in the hundreds of millions of dollars if a single pixel feed is used to cover the entire SKA-High bandwidth.

1.2 About the Thesis

The focus of this thesis is on the formal investigation of a sinuous antenna and its characterisation as a feed for a paraboloid and offset Gregorian reflector systems. This entails

a thorough analysis of the fundamental design parameters and a determination of the performance limitations of the feed.

The study is carried out in a two step process. First, a planar, unidirectional sinuous antenna without absorber lining is studied by means of a thorough parametric study to determine the influence of each parameter, as well as the influence of interactions amongst design parameters, on the system's response. The design guidelines thus derived, are used to design an antenna with an ideal simulated aperture efficiency larger than 65% when used as a feed for a prime focus paraboloid and over 60% for an offset Gregorian reflector system. Strut and feed blockage effects are ignored in calculating the feed's efficiency for a prime focus paraboloid reflector, while edge diffraction effects from the rim of the sub-reflector are included in aperture efficiency calculations of the offset Gregorian system. The antenna has a bandwidth ratio of over $3:1$ measured at a return loss of 10 dB and a mean aperture efficiency of 62.4% calculated from measured $E-$ and $H-$plane radiation patterns. The efficiencies are calculated for a subtended half-angle of $55°$.

Secondly, an efficient scheme is developed to optimise the conical sinuous antenna [9] as well as perform parametric studies for different goals including aperture efficiency, return loss and cross-polarisation, the results of which are used to establish proper design guidelines and performance limitations of the conical sinuous antenna.

The contributions of this work can be summarised as follows:

- Design guidelines and a comprehensive study of the planar and conical sinuous antennas. Design limitations are also discussed.
- An efficient strategy for optimisation and parametric studies that is general enough to be used to accurately model a deterministic system whose inputs ($\leqslant 20$ variables) and corresponding output are known. This technique can also be used on noisy data, such as measurements, by applying a simple averaging procedure, such as moving averages, as a pre-processing step.
- Extension of the bandwidth of a unidirectional printed planar sinuous antenna with no absorber lining from an octave to a bandwidth ratio of over $3:1$ [11].

1.3 Thesis Layout

The thesis begins with a discussion of the theory behind the sinuous antenna. Important definitions and figures of merits for reflector antennas are then given and a discussion of the simulation setup of all electromagnetic (EM) models is discussed in chapter 2. Chapter 3 focuses on the study of a planar sinuous antenna while the mathematical framework and design strategy for the efficient optimisation and parametric study of the conical sinuous antenna (or any other input-output system) is thoroughly discussed in chapter 4. The optimisation and design limitations of a conical sinuous antenna are given in chapter 5 and finally a conclusion to the work is given in chapter 6.

Chapter 2

Theoretical Background

In this chapter, a general theory of the sinuous antenna is presented. This includes a description of the different implementations of the sinuous antenna as well as a brief assessment of their performances. Figures of merit for characterising a feed for reflector antenna applications are described as well as a brief discussion of the numerical methods used to design the antennas in this thesis.

2.1 Sinuous Antenna Theory

2.1.1 The Sinuous Antenna

The sinuous antenna was first described by R.H. DuHamel in his 1987 patent [12]. This antenna belongs to the class of frequency-independent antennas in that its shape is defined by angles rather than lengths [13]. The sinuous antenna consists of an even number of N arms, fed two-by-two, with a phase difference with respect to one another, whose geometry is given by the sinuous curve, defined by (2.1.1) [12]

$$\phi(r) = (-1)^p \alpha_p \sin \frac{\pi \ln \dfrac{r}{R_H}}{\ln \tau_p} \tag{2.1.1}$$

where ϕ and r are the spherical coordinates of any point along the curve, τ_p is the growth rate from cell to cell and R_H is the minimum radius, determining the antenna's high frequency limit. The antenna's angular width is given by α. The sinuous curve is rotated through $\pm\delta$ to form the sinuous arm shown in Fig. 2.1b. Each sinuous arm consists of p radiating cells. The sinuous arm is then rotated in $360/N$ degree increments to form an N arm sinuous antenna, an example of which is shown in Fig. 2.1c for $N = 4$.

It is well known that an antenna structure's log-periodicity contributes significantly to its wideband performance [14]. To take advantage of this fact, the antenna's growth rate τ_p is kept constant (i.e. $\tau_p = \tau$), thus achieving a wideband log-periodic frequency-independent structure. The active region (i.e. radiating cells) of the antenna is located at about a wavelength from the feed, where fields are in phase and thus radiation occurs. Also, it is known that self-complementary antennas have the added advantage of having a constant input impedance independent of frequency [15]. Self-complementarity implies

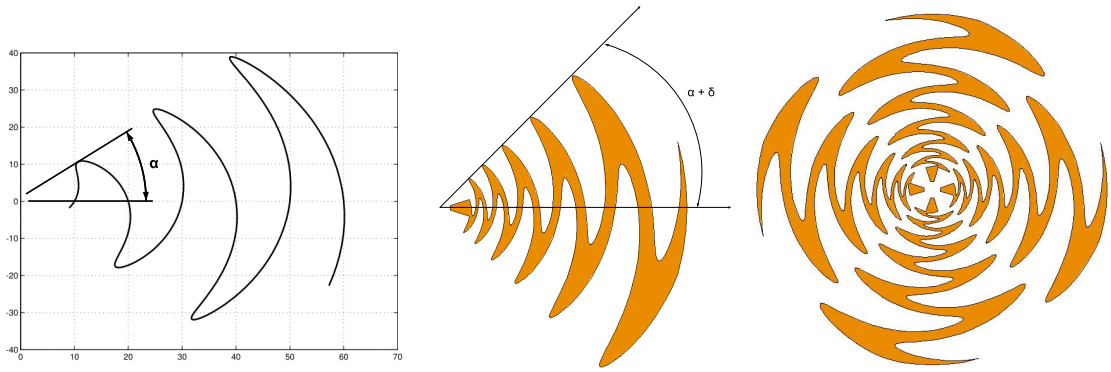

(a) Sinuous curve (b) Sinuous arm (c) Planar Sinuous Antenna

Figure 2.1: Sinuous curve, sinuous arm and four-arm sinuous antenna with associated feed structure

that, for a planar structure, interchanging metallic and dielectric parts does not change the antenna's geometry. A self-complementary sinuous antenna is illustrated in Fig. 2.2.

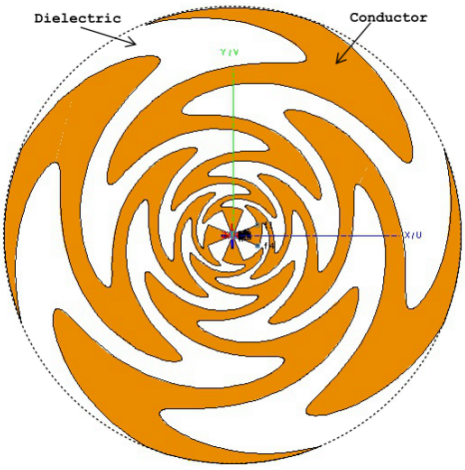

Figure 2.2: Self-complementary sinuous antenna

The sinuous antenna consists of an even number of arms N. The number of arms in an antenna limits the number of possible propagation modes to $m = N - 1$. The input impedance of one arm with respect to ground for a self-complementary antenna is given by Deschamp's formula [12]:

$$Z_m = \frac{30\pi}{\sin\dfrac{m\pi}{N}} \frac{1}{\sqrt{(1+\epsilon_r)/2}} \tag{2.1.2}$$

where ϵ_r is the relative permittivity of the dielectric medium between sinuous arms and m, the excitation mode.

The voltage excitation of each arm for a normal mode is given by:

$$V_{n,m} = A_m e^{j2\pi mn/N} \tag{2.1.3}$$

where $n = 1, 2..., N$, is the arm number and $m = 1, 2, ..., N-1$, is the propagation mode [12]. For instance, in a four-arm antenna the excitation phases are $\{0°, 90°, 180°, 270°\}$

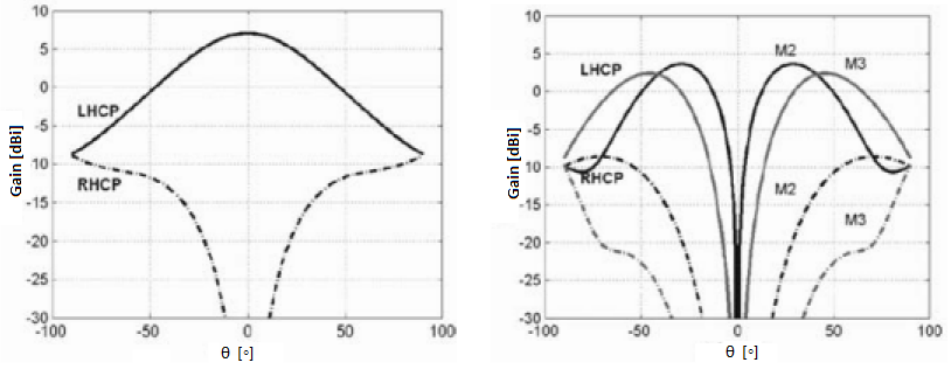

Figure 2.3: Mode patterns for a circularly polarised sinuous antenna. Left: Mode $m = 1$. Right: Modes $m = 2, 3$ [1].

from the first to the fourth arm respectively for mode $m = 1$. i.e. Arms 1 and 3 are fed differentially, ditto for arms 2 and 4. It is worth noting that all modes $m > 1$ result in a pattern null at broadside [1, 12, 16] as shown in Fig. 2.3. This may be useful for direction finding and tracking purposes, but for applications as a feed for reflector systems, the antenna is driven in mode $m = 1$.

Theoretically, the frequency independence of the sinuous antenna implies that it consists of infinitely large conductors, with infinite conducting surfaces, and infinitesimal feed points. This is however not practically feasible and thus cut-off radii need to be defined to limit the frequency of operation. The high frequency cut-off radius, R_H, and the low frequency radius R_L are given by the equations below:

$$R_H = \frac{\lambda_H}{4(\alpha + \delta)} \tag{2.1.4}$$

$$R_L = \frac{\lambda_L}{4(\alpha + \delta)} \tag{2.1.5}$$

where λ_H and λ_L are the high and low frequency wavelengths respectively. Truncating the antenna poses problems that need to be overcome, namely the end-reflection and transition problems. A smooth transition from transmission line mode to radiation, in the region around the feed point, is achieved by typically making R_H in (2.1.4) smaller by a factor of 2. End reflection effects are a direct result of truncating the antenna's outward growth (i.e R_L is finite) and are mitigated by making R_L in (2.1.5) larger by typically 20%.

While it is possible to design a sinuous antenna with an arbitrary even number of N arms, the focus of this thesis lies in the design of an antenna with $N = 4$. Although a design with $N > 4$ provides several options as far as propagating polarisations are concerned, its feed network is usually bulky and quite complex. A design with $N = 4$ produces two orthogonal sets of linearly polarised electromagnetic (EM) waves. This design has the advantage of a less complicated feed structure and other forms of polarisation can be achieved through a bit of signal processing at the feed. For instance, circular polarisation can be obtained by using a 90° hybrid coupler at the feed.

It is worth noting that there are several variations of the printed sinuous antenna that arise as a result of projecting the basic planar sinuous antenna onto some suitable

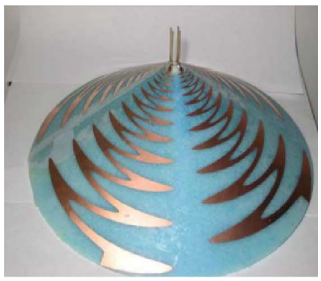

(a) Conical projection [9].

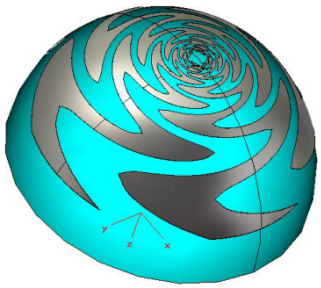

(b) Hemispherical projection [17].

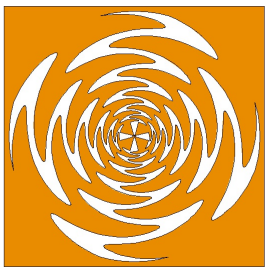

(c) Sinuous slot antenna

Figure 2.4: Sinuous antenna variations.

geometry. A projection onto a hemisphere is presented in [17], while an account of the more popular conical projection is given in [9, 12]. The hemispherical projection in [17] shows performance limitations in terms of radiation pattern and bandwidth compared to the planar antenna. The conical projection, however, is advantageous in that it has improved front-to-back ratio and is shown [9] to be a good candidate for achieving unidirectional radiation over a very wide bandwidth. Both the conical and Hemispherical projections of the sinuous antenna are shown in Fig. 2.4. Other variations of the sinuous antenna include the so-called sinuous slot antenna [18, 19, 20], where each sinuous arm is a slot carved out of a metallic surface. The sinuous slot antenna has the advantage of having a lower input impedance compared to the printed antenna, due to Babinet's principle [21]. Different variations of the sinuous antenna are shown in Fig. 2.4.

The designs in this thesis involve only printed sinuous antennas which are evaluated as feeds in a reflector antenna, either paraboloid or offset Gregorian. The figures of merit (i.e. various efficiencies) for feeds in a reflector antenna configuration are described in the next section.

2.2 Characterisation of Reflector Antenna Performance

Reflector antennas have been in use since the discovery of EM wave propagation by Heinrich Hertz in 1888. Several types of reflectors are used in practice including plane, corner, prime-focus paraboloid, Cassegrain and offset Gregorian reflectors. Radiation in corner and plane reflectors is explained by simple image theory [22], while radiation, in prime-focus paraboloid, Cassegrain and offset Gregorian reflectors, is a direct result of the geometrical relationship between the curved reflecting surface and its focal point. The curved reflecting surface(s) in these antennas is(are) either parabolic, hyperbolic or a combination of the two. Because of the fact that all waves reflected from a parabola or hyperbola pass through its focus, paraboloid, Cassegrain or offset Gregorian antennas, shown in Fig. 2.5, have a much larger gain compared to corner or plane reflector antennas, and they are thus used in high performance applications such as satellite communication and radio astronomy. The focus of the next discussion is on the performance of prime-focus paraboloid, Cassegrain or offset Gregorian reflector antennas.

2.2.1 Figures of Merit

A widely accepted measure of how well a reflector antenna works is the effective area of the reflector given by (2.2.1)

$$A_{eff} = \eta_{ap} A_{ph} \tag{2.2.1}$$

where η_{ap} is the feed's aperture efficiency and A_{ph} is the physical area of the dish at the aperture ($\pi D^2/4$, with D being the aperture's projected diameter). The aperture efficiency can be broken up into sub-efficiencies according to (2.2.2) for prime focus paraboloid reflectors [2],

$$\eta_{ap} = \eta_{BOR_1}\eta_{sp}\eta_{ill}\eta_{ph}\eta_{pol} \tag{2.2.2}$$

where η_{BOR_1} is the BOR_1 (Body Of Revolution type-1) efficiency; η_{sp}, the *spillover* efficiency; η_{ill}, the *illumination* or *taper* efficiency; η_{ph}, the *phase* efficiency and η_{pol}, the *polarisation* efficiency. The aperture efficiency formulation in (2.2.2) is ideal in that effects of aperture blockage, by the feed and supporting struts, are ignored.

The radiated far field function of an antenna can be expressed as (2.2.3).

$$\boldsymbol{G}(\theta,\phi) = G_\theta(\theta,\phi)\hat{\theta} + G_\phi(\theta,\phi)\hat{\phi}. \tag{2.2.3}$$

The ϕ-variation of the far field function, in (2.2.3), is periodic with a period of 2π, and can thus be expanded into a Fourier series to give (2.2.4).

$$\boldsymbol{G}(\theta,\phi) = \sum_{n=0}^{\infty}[A_n(\theta)sin(n\phi) + B_n(\theta)cos(n\phi)]\hat{\theta} + \sum_{n=0}^{\infty}[C_n(\theta)cos(n\phi) - D_n(\theta)sin(n\phi)]\hat{\phi}. \tag{2.2.4}$$

Far field results are calculated or measured at discrete ϕ angles in the $[0, 2\pi]$ range for each θ angle as

$$G_\theta(\theta, k{\cdot}\Delta\phi), G_\phi(\theta, k{\cdot}\Delta\phi), k = 0, 1, 2, \ldots, N-1$$

where N is the number of ϕ-cut planes and $\Delta\phi = 2\pi/N$.

Therefore, Fourier coefficients in (2.2.4) are obtained by the inverse discrete Fourier transform as in (2.2.5)

$$\begin{aligned}
A_n(\theta) &= \frac{2}{N}\sum_{k=0}^{N-1} G_\theta(\theta, k{\cdot}\Delta\phi)\sin(kn\Delta\phi) \\
B_n(\theta) &= \frac{2}{N}\sum_{k=0}^{N-1} G_\theta(\theta, k{\cdot}\Delta\phi)\cos(kn\Delta\phi) \\
C_n(\theta) &= \frac{2}{N}\sum_{k=0}^{N-1} G_\phi(\theta, k{\cdot}\Delta\phi)\cos(kn\Delta\phi) \\
D_n(\theta) &= \frac{2}{N}\sum_{k=0}^{N-1} G_\phi(\theta, k{\cdot}\Delta\phi)\sin(kn\Delta\phi)
\end{aligned} \tag{2.2.5}$$

where $n = 0, 1, \ldots,(N-1)/2$ [23].

We will now proceed to describe the efficiencies in (2.2.2).

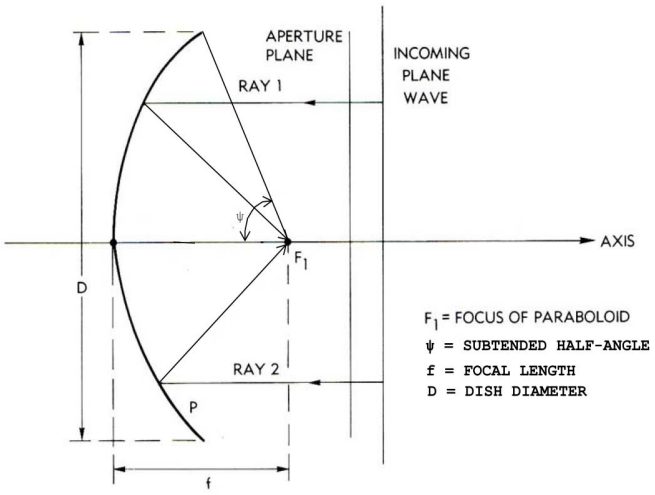

(a) Paraboloid reflector geometry

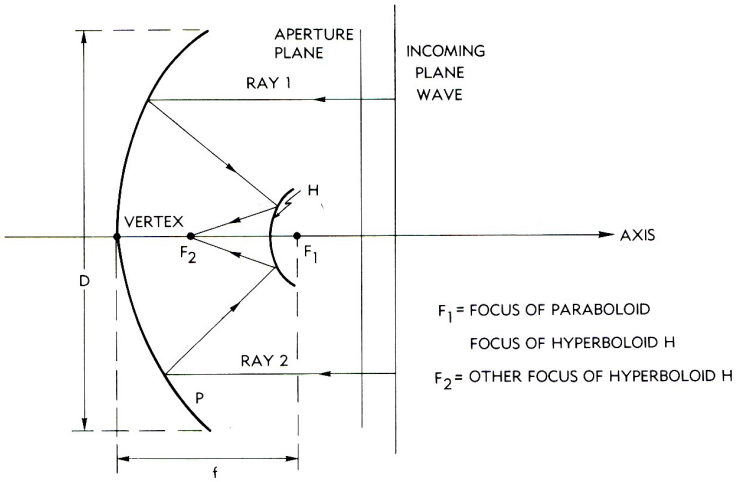

(b) Cassegrain reflector geometry

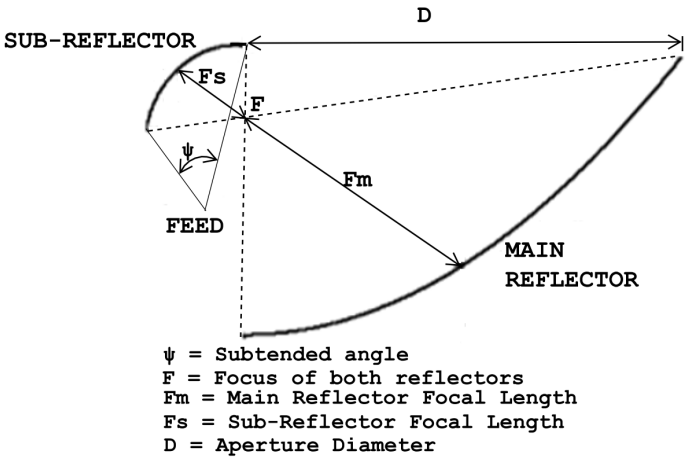

(c) Offset Gregorian reflector geometry

Figure 2.5: High performance reflector antenna geometries.

$\mathbf{BOR_1}$ Efficiency

It describes a measure of rotational symmetry in the feed. The main idea [24] involves comparing the far field function in (2.2.3) with the one that would be obtained when the antenna is excited by an infinitesimal dipole that lies in a direction orthogonal to the axis of symmetry of the antenna. If $\boldsymbol{z}$ is the axis of symmetry and the exciting dipole is $\boldsymbol{y}$-polarised with magnitude Il, then the far field function is given by (2.2.6).

$$\boldsymbol{G_y}(\theta,\phi) = -j\frac{k\eta Il}{4\pi}[(\cos\theta\sin\phi)\hat{\theta} + (\cos\phi)\hat{\phi}]. \tag{2.2.6}$$

A comparison of (2.2.6) with (2.2.4) shows that for BOR_1 antennas, only the $n = 1$ ϕ-modes, referred to as BOR_1 components, are excited. Therefore only the $n = 1$ ϕ-modes contribute to on-axis gain and all higher order ϕ-modes represent power lost in side lobes.

The BOR_1 efficiency is thus defined as the ratio of power in BOR_1 components to the total radiated power and it is given by (2.2.7)

$$\eta_{BOR_1} = \frac{\int_0^{2\pi}\int_0^{\pi}[|G_{\theta 1}|^2 + |G_{\phi 1}|^2]\sin\theta d\theta d\phi}{\int_0^{2\pi}\int_0^{\pi}[|G_{\theta}(\theta,\phi)|^2 + |G_{\phi}(\theta,\phi)|^2]\sin\theta d\theta d\phi} \tag{2.2.7}$$

where [23]

$$G_{\theta 1} = A_1(\theta)\sin\phi + B_1(\theta)\cos\phi$$
$$G_{\phi 1} = C_1(\theta)\cos\phi - D_1(\theta)\sin\phi$$
$$\int_0^{2\pi}\int_0^{\pi}[|G_{\theta 1}|^2 + |G_{\phi 1}|^2]\sin\theta d\theta d\phi = \pi\int_0^{\pi}[|A_1(\theta)|^2 + |B_1(\theta)|^2 + |C_1(\theta)|^2 + |D_1(\theta)|^2]\sin\theta d\theta \tag{2.2.8}$$

Of course, the calculation of BOR_1 efficiency implies that the antenna can be excited in at most 2 polarisations orthogonal to the axis of symmetry. If only one polarisation is excited, then either A_1 and C_1 or B_1 and D_1 will be zero. In line with the notation in [2], for a $\boldsymbol{y}$-polarised excitation, the radiated far field is given by:

$$\boldsymbol{G(r)} = \frac{1}{r}e^{-jkr}[A_1(\theta)\sin\phi\hat{\boldsymbol{a}}_{\boldsymbol{\theta}} + C_1(\theta)\cos\phi\hat{\boldsymbol{a}}_{\boldsymbol{\phi}}]. \tag{2.2.9}$$

From Ludwig's third definition of co- and cross-polarisation [25], the co- and cross-polarised field are obtained from (2.2.9) as

$$E_{co} = \frac{1}{r}e^{-jkr}[CO(\theta) - XP(\theta)\cos(2\phi)] \tag{2.2.10}$$

$$E_{xp} = \frac{1}{r}e^{-jkr}XP(\theta)\sin(2\phi) \tag{2.2.11}$$

where

$$CO(\theta) = [A_1(\theta) + C_1(\theta)]/2 \tag{2.2.12}$$

$$XP(\theta) = [A_1(\theta) - C_1(\theta)]/2 \tag{2.2.13}$$

CO(θ) and XP(θ) are the co- and cross-polarised BOR_1 patterns in the $\phi = 45°$ plane respectively as per the third definition in [25]. The BOR_1 notation for far fields is advantageous in that the ϕ integral is not evaluated during efficiency calculations.

Spillover Efficiency

This is a measure of the amount of power radiated from the feed that is intercepted by the dish in a prime focus paraboloid reflector. i.e. The power within the subtended angle θ_0, denoted by ψ in Fig. 2.5a. It is given by

$$\eta_{sp} = \frac{\int_0^{\theta_0} \left[|CO(\theta)|^2 + |XP(\theta)|^2\right] sin\theta d\theta}{\int_0^{\pi} \left[|CO(\theta)|^2 + |XP(\theta)|^2\right] sin\theta d\theta} \tag{2.2.14}$$

Illumination or Taper Efficiency

This represents a measure of the uniformity of the amplitude distribution of the feed pattern over the surface of the reflector [14], and is given by:

$$\eta_{ill} = 2\cot^2(\theta_0/2) \frac{\left[\int_0^{\theta_0} |CO(\theta)| \tan(\theta/2) d\theta\right]^2}{\int_0^{\theta_0} |CO(\theta)|^2 \sin\theta d\theta} \tag{2.2.15}$$

Polarisation Efficiency

This refers to a measure of the percentage of power in the desired polarisation in the aperture plane and is given by

$$\eta_{pol} = \frac{\int_0^{\theta_0} |CO(\theta)|^2 \sin\theta d\theta}{\int_0^{\theta_0} \left[|CO(\theta)|^2 + |XP(\theta)|^2\right] \sin\theta d\theta} \tag{2.2.16}$$

Phase Efficiency

It is a measure of the uniformity of the radiated field's phase over the reflector's aperture plane, given by

$$\eta_{ph} = \frac{\left|\int_0^{\theta_0} CO(\theta) \tan(\theta/2) d\theta\right|^2}{\left[\int_0^{\theta_0} |CO(\theta)| \tan(\theta/2) d\theta\right]^2} \tag{2.2.17}$$

Diffraction Efficiency

In Cassegrain and offset Gregorian reflector systems, an additional sub-efficiency, accounting for edge diffraction effects at the rim of the sub-reflector, needs to be defined. An analytical formula for the diffraction efficiency is given in [26] for a feed pattern described by a $G_f(\theta) = (n+1)\cos^{2n}(\theta/2)$ family of functions. The value of n is easily determined by fitting $G_f(\theta)$ onto the simulated far field data up to and including the subtended half-angle θ_0. The diffraction efficiency, η_d, is given by

$$\eta_d = \left|1 + \frac{n\sin^2(\theta_0/2)\cos^n(\theta_0/2)}{1-\cos^n(\theta_0/2)} \frac{(j-1)}{\sqrt{2\pi}} \frac{\Delta\rho}{D}\right|^2 \tag{2.2.18}$$

where

$$\Delta\rho = \sqrt{\frac{\lambda(\rho_{m0} + \sigma\rho_{s0})}{\pi} \left|\frac{\rho_{m0}}{\rho_{s0}}\right|} \tag{2.2.19}$$

and D is the projected aperture's diameter. The focal lengths of the main and sub-reflectors are given by ρ_{m0} and ρ_{s0} respectively and the parameter σ is set to 1 for offset Gregorian and -1 for Cassegrain systems.

The subtended angle is related to the geometry of the dish in Fig. 2.5 by

$$f = \left(\frac{D}{4}\right) \cot\left(\frac{\theta_0}{2}\right) \tag{2.2.20}$$

where f is the focal length of the paraboloid.

2.3 Numerical Analysis

Because of the complexity of the antenna's geometry, it is extremely difficult or nearly impossible to analytically characterise its performance (i.e. to solve for radiated fields and S-parameters). Numerical techniques are used instead.

The antenna is simulated using FEKO [27], a commercial method of moments (MoM) 3D full wave EM solver. Accurate solutions can only be obtained if the correct meshing scheme is applied to the model. A coarse mesh produces less accurate results while a fine mesh accurately resolves currents over the antenna's geometry. Fast computation times are achieved with coarse meshing while an exponential increase is observed with increasingly finer meshes. The recommended MoM *mesh step size* for *faces* in [27], is $\lambda/10$, with λ being the wavelength at the highest simulated frequency. The pre-defined *standard* mesh setting ($\lambda/12$) in [27] is thus sufficient as a global mesh setting.

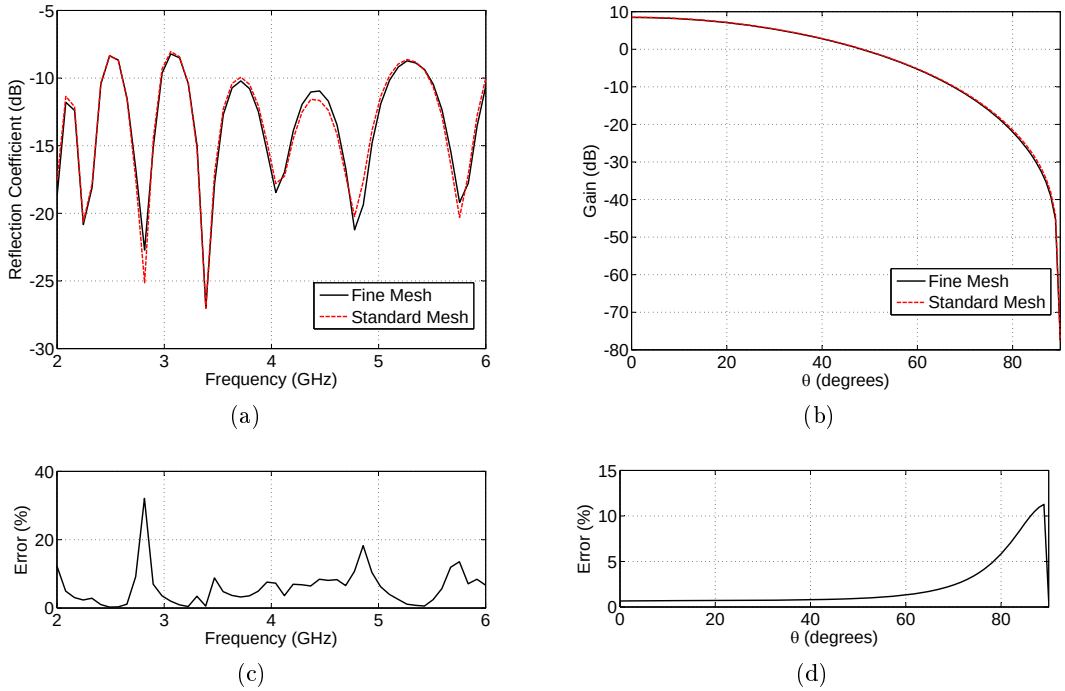

Figure 2.6: Convergence study with different meshing schemes on a sinuous antenna over an infinite ground plane. (a) Comparison of return loss responses between standard and fine meshing. (b) Comparison of simulated radiation patterns at 2 GHz. (c) Error in return loss between fine and standard meshing. (d) Error between simulated patterns at 2 GHz.

A convergence study conducted, showed that results obtained with the *fine* mesh setting ($\lambda/16$) with adaptive point refinement and the *standard* mesh setting were essentially the same for the sinuous antenna model as shown in Fig. 2.6, where the error between the simulated responses of the two meshing schemes is mostly below 15%, with the highest errors being observed at the troughs of the return loss response, where such an error is insignificant. The error function used is of the form $(|x_{fine} - x_{std}|)/x_{std}$, where x_{fine} and x_{std} denote the responses with a fine and standard mesh respectively. Also, for a simple surface like a planar sheet of metal, the *coarse* mesh setting ($\lambda/8$) yields sufficiently accurate results.

Therefore, for all analysed models in subsequent chapters, unless stated otherwise, curved surfaces (e.g. The sinuous antenna) are solved with FEKO's *standard* mesh setting and simple surfaces like a rectangular plate are solved with the EM solver's *coarse* mesh setting.

Chapter 3

Planar Sinuous Antenna

Conventional designs of printed planar sinuous antennas involve the use of an absorber to achieve unidirectional radiation over a very wide bandwidth. The conventional argument is that an absorber-free design is limited to a bandwidth of an octave or so [9], despite offering a better system temperature performance.

A planar sinuous antenna is studied in this chapter with a view to achieving unidirectional radiation whilst not using any absorbing material. A comprehensive parameter study is carried out to explore the design space and an initial goal of a return loss of 10 dB or better, across more than an octave bandwidth, is set. The antenna's performance as a feed for paraboloid and offset Gregorian reflector systems is evaluated with the goal of maximising aperture efficiency.

3.1 The Radiation Problem

While the planar sinuous antenna achieves a very wide instantaneous bandwidth, its radiation pattern is bidirectional by nature as shown in Fig. 3.1, with a peak on-axis gain of typically 4 dB.

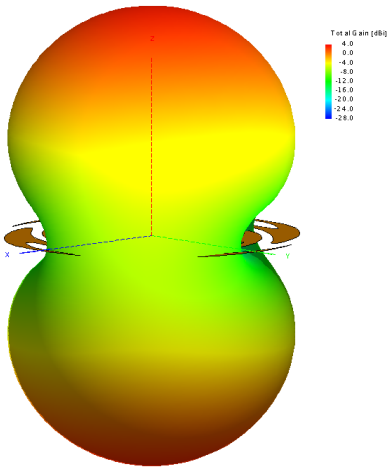

Figure 3.1: Bidirectional radiation pattern of a planar sinuous antenna in free space.

Many applications however require the use of a unidirectional antenna. Most scientific

research and implementation as well as commercially available printed, planar sinuous antennas make use of an absorber lined cavity [28, 29] to achieve unidirectional radiation. Such an implementation is hereafter referred to as conventional planar sinuous antenna. While the conventional antenna exhibits very wide bandwidths with nearly constant input impedance, its radiation efficiency is reduced to about 50% and the absorber contributes to the increase in system temperature by as much as 150 K, which may not be acceptable for noise critical applications. Another method of achieving unidirectional radiation involves using a reflecting ground plane. Simple image theory [22] explains radiation in this scenario. The latter method results in reduced bandwidth when compared to the former. Also, the desirable self-complementarity is lost as a result of the image below the ground plane not being a complement of the antenna [30]. However, the significant noise reduction as a result of not using an absorber makes the latter approach more advantageous over the former. A design with a reflecting ground plane is described in the subsequent sections.

3.2 Directive Sinuous Antenna

In this section, a wideband planar, printed sinuous antenna backed by a lossless cavity is designed and its performance as a feed for a reflector antenna is discussed.

3.2.1 Parameter Study

A systematic parameter study is conducted to understand the effect of each of the design parameters. All simulations are done in FEKO as described in section 2.3. A four-arm antenna with two linear polarisations is considered and the main design parameters are listed in Table 3.1.

Table 3.1: Design Parameters

Parameter	Description
α	Angular Width
δ	Rotation Angle
τ	Growth Rate
h	Distance from Ground Plane

A simplified antenna model with a simple differential feed, shown in Fig. 3.2, as well as an infinite ground plane is used in order to speed up simulations. This model yields accurate simulation results for all except side lobe levels.

Effects of h

As stated in section 3.1, the presence of a ground plane results in an input impedance that varies with frequency. Also, having a finite antenna with a finite ground plane means that the input impedance can not be approximated by Deschamp's formula in (2.1.2). The impedance is instead determined by full-wave EM simulations.

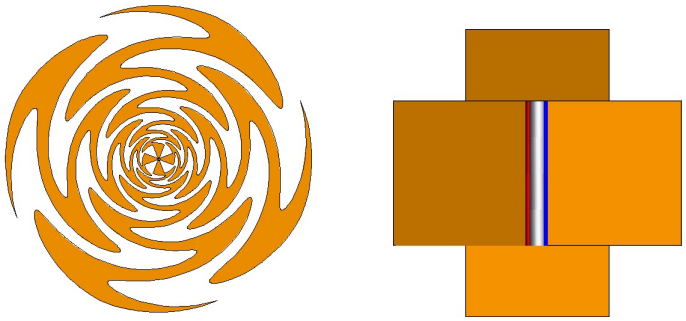

(a) (b)

Figure 3.2: Simple antenna and differential feed used for parameter study. (a) Antenna. (b) Differential edge port definition at the centre of the antenna in FEKO.

The parameter h in Table 3.1 determines the frequency at which a broadside null, due to phase cancellation of reflected fields from the ground plane, occurs and thus effectively determines the bandwidth of the antenna. The distance h is thus chosen such that the pattern null occurs at a frequency outside the band of interest. For a bandwidth in the range $[f_{min}, f_{max}]$, a broadside null occurs at $2f_{min}$ if h equals $\lambda_{min}/4$, where λ_{min} is the wavelength at f_{min}, as shown in Fig. 3.3 for $f_{min} = 5$ GHz.

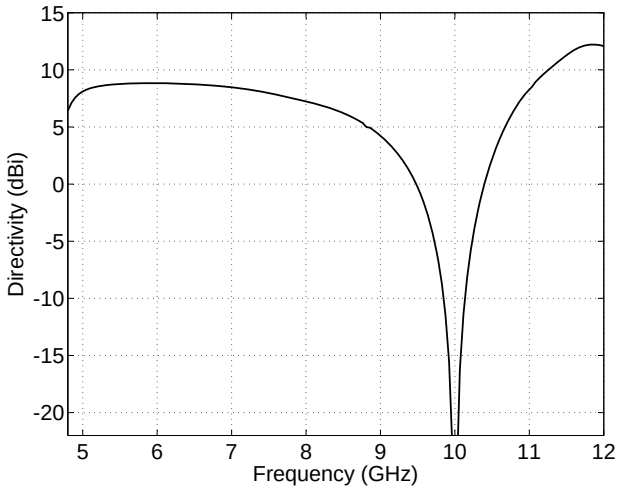

Figure 3.3: Broadside pattern null at $2f_{min}$ for $f_{min} = 5$ GHz. The null results from phase cancellation between radiated fields and fields reflected from the conducting ground plane.

To accommodate the entire band, h is given by (3.2.1)

$$h = \frac{c}{4f} \tag{3.2.1}$$

$$f > \frac{f_{max}}{2} \tag{3.2.2}$$

where f is the frequency and c is the speed of light.

Simulations also show that half-power beam width (HPBW) and cross-polarisation levels of the antenna can be controlled by varying h, with small values of h generally resulting in lower cross-polarisation and smaller variation in HPBW when compared to designs with larger values of h as shown in Fig. 3.4. It is also evident from Fig. 3.4 that significant return loss performance degradation, as can be seen in the reflection coefficient

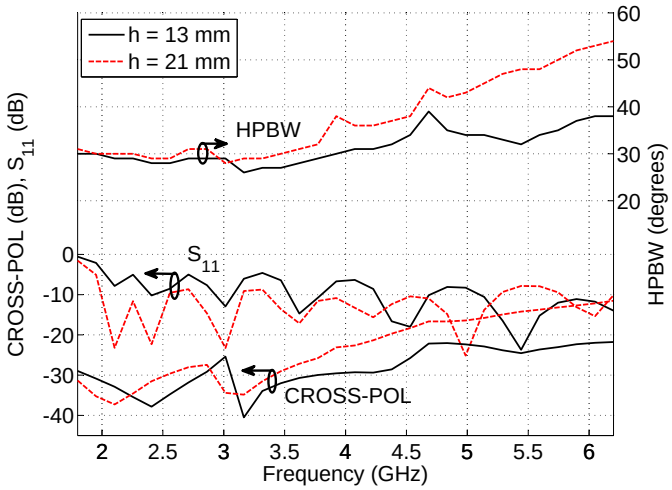

Figure 3.4: Effect of h on HPBW, cross-polarisation and return loss.

plot indicated by S_{11} in Fig. 3.4, results from h being small. This is due to the close proximity of the ground plane to the antenna resulting in a sharp decrease in radiation resistance and thus input impedance at low frequencies and hence the relatively poor return loss.

Angular width and rotation angle

The angular width, α, and the rotation angle, δ, vary the amount of interleaving between sinuous arms. Increased interleaving ($\alpha > 45°$) not only leads to tighter manufacturing tolerances, but it also yields poor return loss performance compared to a design with decreased interleaving ($\alpha < 40°$), as is shown for the conical projection in [9]. The choice of the α/δ ratio has to be sensible as too small a value leads to a geometry that is more of a bow tie antenna than a sinuous one. Examples of antenna models with different levels of interleaving are shown in Fig. 3.5.

(a) $\alpha = 29°$. (b) $\alpha = 50°$.

Figure 3.5: Sinuous antennas with different interleaving, while maintaining the same α/δ ratio.

Growth rate

The growth rate τ influences the number of radiating cells, varying the thickness of sinuous arms and contributing to the overall rotational symmetry of the antenna. It is well known that the log-periodicity of an antenna improves its bandwidth. Therefore, τ_p in (2.1.1) is kept constant (i.e. $\tau_p = \tau$), to achieve a wideband log-periodic sinuous antenna.

Combined effect of τ, α and δ

A study on the effects of α, δ and τ on the return loss and aperture efficiency calculated from the feed's radiation pattern using the formulas in [2], for a prime focus paraboloidal reflector, yields bounds within which the named parameters may be chosen to achieve a given objective, for a design with $25° \leq \alpha < 40°$.

$$1.41 \leq \frac{\alpha}{\delta} \leq 1.91 \tag{3.2.3}$$

$$0.77 \leq \tau \leq 0.85 \tag{3.2.4}$$

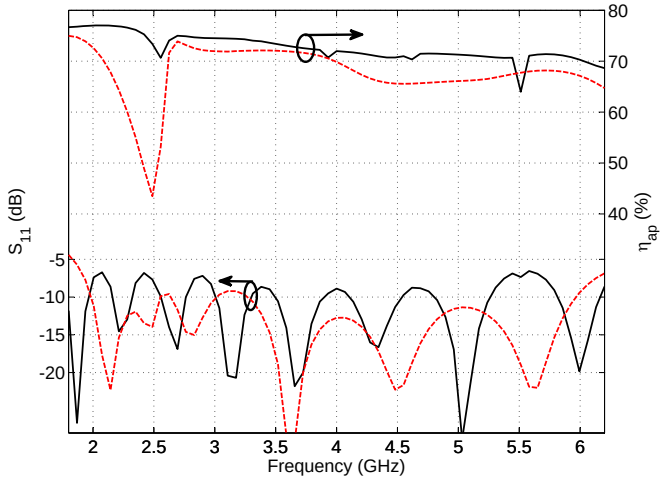

Figure 3.6: Performance bounds on α, τ and δ and their effect on return loss and aperture efficiency for a prime focus reflector antenna. Solid lines: Upper bounds. Dotted lines: Lower bounds

A design with a combination of the lower bounds in (3.2.3) and (3.2.4) leads to an antenna with thick sinuous arms, resulting in a return loss better than 10 dB over a wide bandwidth. This is justified by the fact that the antenna occupies a much larger volume within its radiation sphere, thus resulting in a wide matched bandwidth [14]. The drawback with this combination of α, δ and τ, is a reduced aperture efficiency. A combination of the upper bounds in (3.2.3) and (3.2.4) produces a design with an ideal aperture efficiency that's mostly above 66% across the band while having a somewhat degraded return loss performance. The calculated aperture efficiency excludes feed and struts blockage as well as edge diffraction effects. The performance bounds in (3.2.3) and (3.2.4) can thus be used for performance trade-offs and a good starting point for a given design. Fig. 3.6 illustrates the effects of the performance bounds in (3.2.3) and (3.2.4).

The sharp decrease in aperture efficiency at about 2.5 GHz in Fig. 3.6, as well as ways of minimising this effect, are explained in section 3.3.

Effects of the ground plane's size

The size of the ground plane directly relates to the level of side lobes in the far field pattern. The larger the ground plane, the lower the side lobe level when compared to the main beam's peak. The size of the ground plane, as demonstrated in section 3.3, also has an effect on how good the BOR_1 efficiency at a particular frequency is.

3.3 Electrical Design

Following the study in section 3.2.1, a dual linearly polarised planar antenna over a ground plane is designed and its performance, as a feed for large paraboloid and offset Gregorian reflector antenna systems, is characterised.

Although a small value of h is advantageous in terms of structure compactness, nearly constant beam width as well as relatively low cross-polarisation, as shown in Fig. 3.4, a design with a larger value of h ($h > 18$ mm for a $2-6$ GHz bandwidth) is preferred as the antenna can easily be matched across the bandwidth. The range of possible values of h limits the achievable bandwidth ratio to just over $3:1$.

For a design target of a return loss better than 10 dB and a prime focus paraboloid aperture efficiency of at least 65% across a $3:1$ bandwidth, a ratio $\alpha/\delta = 1.82$ as well as a value of $\tau = 0.83$ are selected from (3.2.3) and (3.2.4). A parameter sweep gives $h = 21$ mm as the optimum value.

To reduce end reflection effects, accentuated by the presence of a reflecting ground plane, the antenna's outer radius given by (2.1.5), is scaled by 12.8% instead of the conventional 20% scaling. The design parameters are summarised in Table 3.2.

Table 3.2: Value of Design Parameters

Parameter	Value
α	29.00°
δ	15.94°
τ	0.830
h	21.00 mm
Diameter	111.2 mm

3.3.1 Feed Network

The realised antenna's feed, in Fig. 3.7, consists of two sets of twin-lead lines enclosed within a cylinder. The cylinder serves the dual purpose of preventing radiation from the feed lines much like in a coaxial line, as h is larger than $\lambda/4$ at 6 GHz, and capacitance compensation for the extra inductance introduced by the feed lines giving a differential input impedance of 200 Ω, that allows easy integration with differential LNAs using commercially available transistors. The required diameter of each line as well as the

separation distance between the lines are determined using full-wave simulations as 0.8 mm and 5 mm respectively. The optimal height of the cylinder is determined as 10.5 mm, by means of a parameter sweep in FEKO.

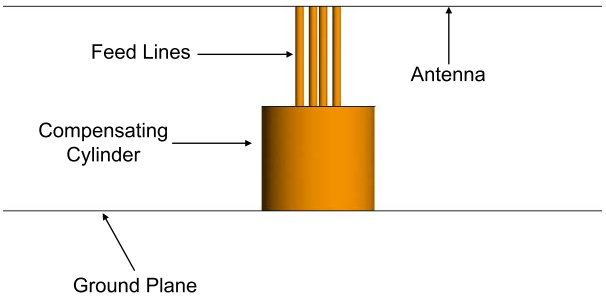

Figure 3.7: Side view of the feed structure showing the four feed lines to each sinuous arm and the cylinder which is connected to the reflecting ground plane.

3.3.2 Simulation Results

An ideal, differentially fed antenna, with a finite reflecting ground plane with a circumference of $2.4\lambda_{min}$ (λ_{min} is the wavelength at $f_{min} = 2$ GHz), was simulated and a return loss of 10 dB or better is achieved from $1.95-6.2$ GHz, a bandwidth ratio better than $3:1$ as shown in Fig. 3.8. The simulated isolation remains well below -35 dB for the entire band, as shown in Fig. 3.9a. For reference, the simulated differential input impedance at the feed, as discussed in section 3.3.1, is shown in Fig. 3.9b, with an average value of $Z_{in} = 220.15 + j3.73\ \Omega$ when normalised to 200 Ω. The antenna's performance, as a feed

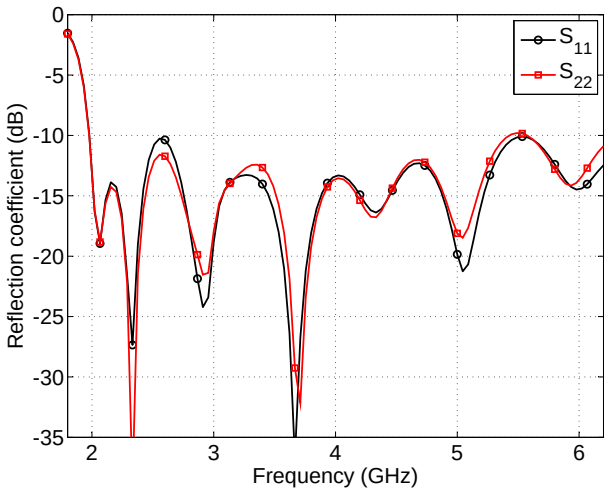

Figure 3.8: Simulated reflection coefficients of the differentially fed antenna with S_{11} and S_{22} indicating the reflection coefficient for each polarisation.

for a large prime-focus and offset Gregorian reflector system, is analysed using equations given in section 2.2.1. The subtended half-angle is chosen such that aperture efficiency is maximised. Fig. 3.10 shows a plot of aperture efficiency and its associated sub-efficiencies as a function of the subtended half-angle, at the mid-band frequency. It is clear from Fig. 3.10 that maximum aperture efficiency (η_{par}) occurs around $\theta_0 = 55°$.

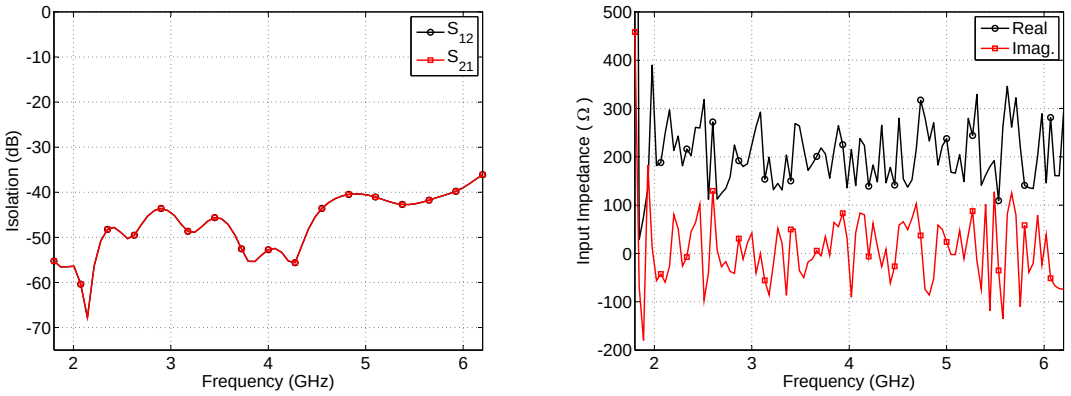

(a) (b)

Figure 3.9: Additional simulation results as a function of frequency: (a) Isolation between the two polarisations. (b) Real and Imaginary parts of the input impedance at the feed, for a 200Ω differential port impedance.

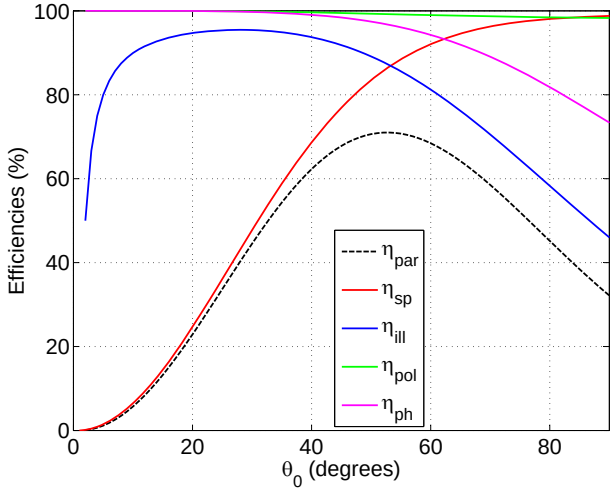

Figure 3.10: Efficiencies as a function of the subtended half-angle θ_0, at 4 GHz.

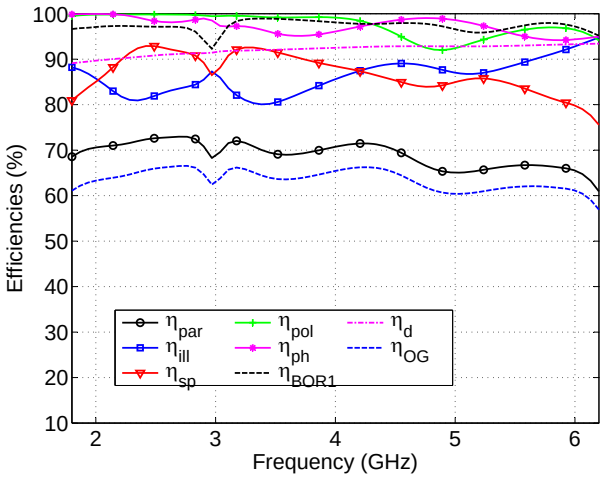

Figure 3.11: Simulated aperture efficiency and sub-efficiencies for a prime-focus paraboloid (η_{par}) and offset Gregorian (η_{OG}) reflector system for a subtended half-angle of 55°.

The aperture efficiency and various sub-efficiencies, including diffraction (η_d), are

shown in Fig. 3.11 as a function of frequency. An aperture efficiency (η_{par}) better than 65% is obtained for a prime-focus paraboloid reflector system, while an efficiency (η_{OG}) larger than 60%, across the entire band from 2−6 GHz, is obtained for an offset Gregorian system by accounting for diffraction effects at the edges of the sub-reflector.
The spillover efficiency remains larger than 80% across the entire band, decreasing as frequency increases. This is due to the broadening of the main beam as frequency increases, especially from about 4.5 GHz, as shown by the HPBW in Fig. 3.12. Spillover efficiency can be improved by slightly altering the reflector's optics, such as the sub-reflector extension method investigated in [31]. The BOR_1 efficiency, which describes the measure of the antenna's rotational symmetry, is larger than 97% for most of the band, except for the dip around 3 GHz, where $\eta_{BOR_1} \approx 92\%$. The reason for this occurrence is explained in section 3.3.3.

All efficiencies are computed for an effective subtended half-angle of 55° and a projected aperture diameter of 13.5 m; and effects of aperture blockage by the feed or struts are ignored. The offset Gregorian reflector system's reflectors have maximum chords of 15.85 m and 3.8 m for the main and sub-reflectors respectively.

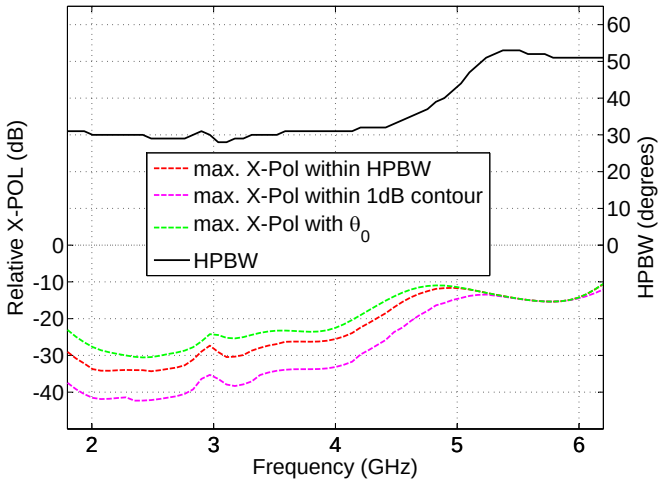

Figure 3.12: Half-power beam width and maximum relative cross-polarisation levels of BOR_1 patterns within 1 and 3 dB contours of the main beam as well as within the subtended half-angle $\theta_0 = 55°$, in the $\phi = 45°$ plane.

Fig. 3.12 shows the simulated HPBW, with a marked increase from 28° to 53° from 4.5 GHz, as a function of frequency. Also shown on the same figure, are the maximum relative cross-polarisation levels calculated within a 1 dB contour of the main beam's maximum, as well as within the HPBW and subtended half-angles. The relative cross-polarisation in all three cases is below −20 dB up to 4 GHz after which it rises to a peak of −11 dB. This increase in cross-polarisation is a direct result of the trade-off in the value of h as discussed in section 3.2.1 and shown on Fig. 3.4.

The designed planar antenna has a high BOR_1 efficiency, as shown on Fig. 3.11, and therefore its radiation pattern can be characterised using BOR_1 patterns given in eq. (2.2.10−2.2.13). The normalised co- and cross-polarisation patterns are shown in Fig. 3.13, at different frequencies across the band, revealing side lobe levels that are below

−20 dB relative to the main beam's peak. Side lobe levels can be further decreased by increasing the size of the reflecting ground plane.

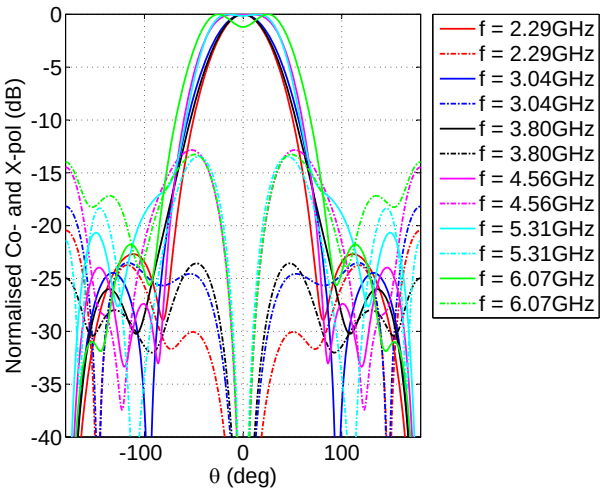

Figure 3.13: Co-polarised (solid lines) and cross-polarised (dashed lines) BOR_1 radiation pattern in the $\phi = 45°$ plane. The broadening of the main beam as frequency increases is more clearly seen here for frequencies above 4.5 GHz.

3.3.3 BOR_1 Efficiency Analysis

The BOR_1 efficiency, η_{BOR_1}, is a measure of rotational symmetry as stated in section 2.2.1. It is related to the physical symmetry of the antenna as well as symmetry in the distribution of surface currents on the structure. The efficiency plots in Fig. 3.11, show η_{BOR_1} to be larger than 96% for most of the simulated band, except for a dip to about 91% around 3 GHz.

It is stated in section 2.1.1, that the active region, from which radiation occurs, is located at about a wavelength from the feed points. This implies that surface currents are concentrated at the edges of the antenna at low frequencies, decaying as frequency increases. A plot of the current densities at the edge of the antenna as a function of frequency is shown in Fig. 3.14a, showing that a decay in surface current density, as a function of frequency, does occur except at around 2.98 GHz where there is significant charge accumulation at the edge, illustrated by the spike in the normalised surface current density plot. Fig. 3.14b shows a screen shot of the distribution of surface current density on the antenna at 2.98 GHz, where it can clearly be seen that the accumulation of surface current at the edges occurs on the vertically oriented pair of arms, while currents on the horizontal pair decay as the radius of the antenna increases, as expected. This lack of symmetry in current distribution, between the two pair of arms, results in the decrease in BOR_1 efficiency around this particular frequency.

A systematic investigation into the probable causes of charge accumulation at the edges of the antenna, as well as its asymmetrical distribution, was carried out by considering a free-standing antenna (i.e. No ground plane) with different levels of interleaving, an antenna with an infinite reflecting ground plane as well as antennas with varying ground plane sizes. Simulations of the free-standing antenna as well as one with an infinite

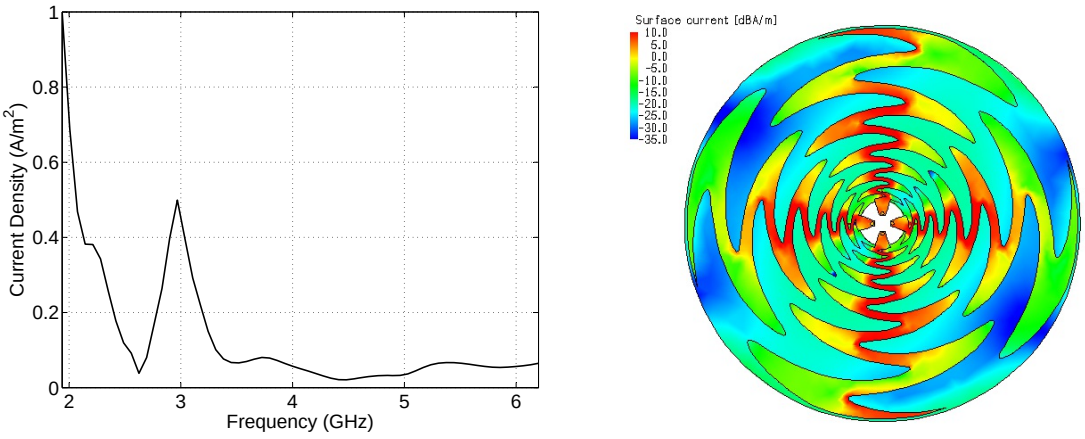

(a) (b)

Figure 3.14: (a) Normalised current density at the outer edge of the antenna as a function of frequency showing a high concentration of charges not only at the lower end of the $2-6$ GHz band, but also around 3 GHz, a frequency corresponding to the dip in BOR_1 efficiency in Fig. 3.11. (b) Screen shot of surface current distribution on the antenna at 2.98 GHz, showing the lack of symmetry in the accumulation of charge at the edges of the antenna's arms.

reflecting ground plane, shown in Fig. 3.15, indicate that charge accumulation at the edges of the antenna around 3 GHz, for a design in the $2-6$ GHz band, is inherent to the structure of the antenna, except that the presence of a reflecting ground plane results in asymmetrical surface current distribution on both sinuous arm pairs, regardless of the amount of interleaving between arms, as can be readily seen on Fig. 3.15b, 3.15c and 3.14.

Next, the effect of the size (perimeter or circumference) of a finite reflecting ground plane on η_{BOR_1} is investigated. For convenience, the size of the ground plane is defined as a factor of λ_{min}, the wavelength at 2 GHz, the design's low frequency bound. The results are summarised in Table 3.3, where an improvement in BOR_1 efficiency is seen for increasingly smaller ground plane sizes.

An investigation into the shape of the reflecting ground plane shows that for larger (i.e. $> 3\lambda_{min}$ in perimeter) sizes, a circular plane performs better than a square plane, in terms of BOR_1 efficiency; while no significant improvement is observed for smaller (i.e. $\leqslant 2.4\lambda_{min}$ in perimeter) reflecting ground planes.

Table 3.3: Effects of ground plane size on BOR_1 efficiency

Size	Worst in-band η_{BOR_1}
$6.14\lambda_{min}$	82.8%
$3.5\lambda_{min}$	88.4%
$2.4\lambda_{min}$	92.3%

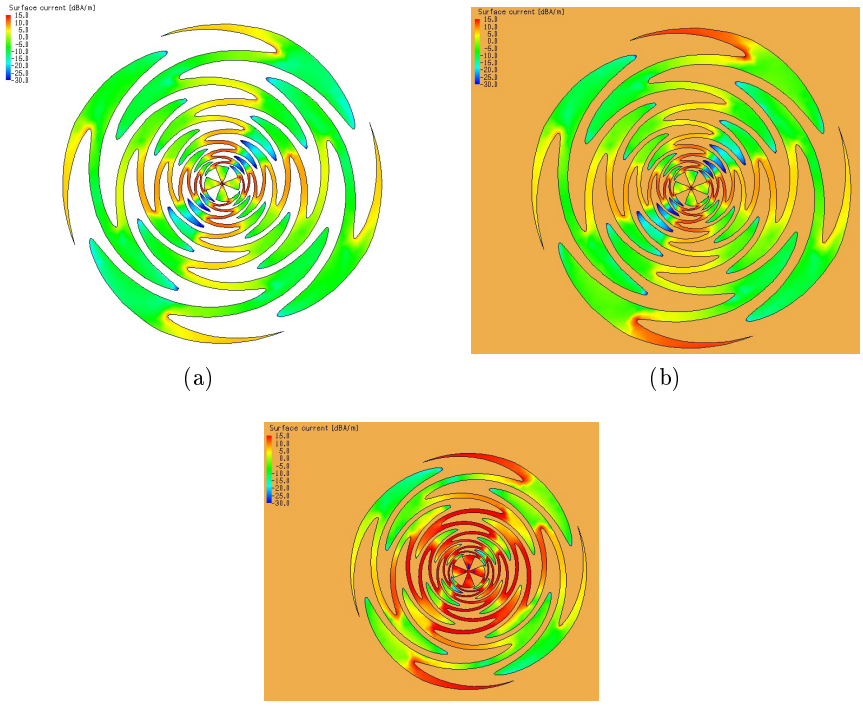

(a) (b)

(c)

Figure 3.15: Surface current distribution at 2.98 GHz on: (a) Free-standing self complementary sinuous antenna. (b) Self-complementary antenna over an infinite reflecting ground plane. (c) Antenna with large interleaving ($\alpha = 53.5°$) over an infinite reflecting plane.

3.4 Construction and Measurement

The sinuous antenna was etched onto a Rogers RO4003 substrate with a dielectric constant of $\epsilon_r = 3.55$, a loss tangent $\tan\delta = 0.0027$ and a thickness of 0.508 mm. The feed detail in Fig. 3.7 was assembled using off-the-shelf components as machining a customised open cylinder increases the complexity of the manufacturing process and is unnecessary. Therefore a slight modification, from parameter values given in Table 3.2, was required to accommodate the dimensions of all components required to build the feed in Fig. 3.7, while maintaining responses similar to the ones in Fig. 3.8 and Fig. 3.11.

The new dimensions of the antenna and feed are listed in Table 3.4, where d_{pin}, d_{cyl} and h_{cyl} are the diameter of the feeding pins, diameter and height of the cylinder respectively as shown in Fig. 3.7 and R_L is the outer radius of the antenna. Inner conductors of standard semi-rigid coaxial lines were used as the feeding pins illustrated in Fig. 3.7.

Table 3.4: Modified antenna and feed dimensions for manufacturing purposes.

Parameter	Value
α	30°
δ	19°
τ	0.83
d_{pin}	0.90 mm
d_{cyl}	11.54 mm
h_{cyl}	10.0 mm
Diameter	99.06 mm

To interface the designed antenna with measurement instruments, a stepped impedance matching network was designed to match the antenna's differential input impedance of 200 Ω to the standard 50 Ω impedance of available Vector Network Analysers (VNA), across the entire design bandwidth. The built antenna is shown in Fig. 3.16, with the matching network's ground plane also serving as the reflecting plane.

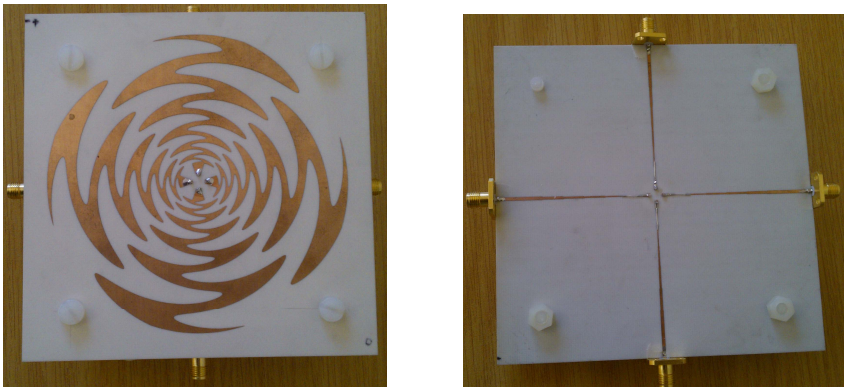

(a) Top view. (b) Bottom view.

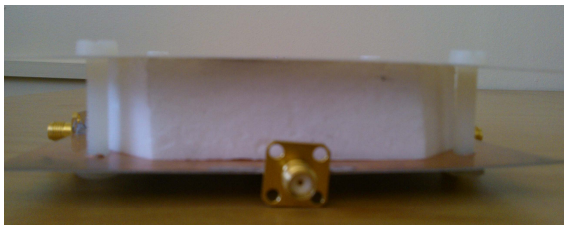

(c) Side view.

Figure 3.16: Photographs of the built and assembled antenna, showing soldered SMA connectors for measurement purposes and screws and polystyrene foam used to maintain the distance between the antenna ground plane at 21 mm as well as for structural support.

Return loss measurements were performed on a calibrated ZVB network analyser from Rhodes&Schwarz. A four port measurement of the antenna was carried out, from which the differential reflection coefficient was extracted using the technique described in [32]. The simulated as well as measured results for both polarisations are shown in Fig. 3.17.

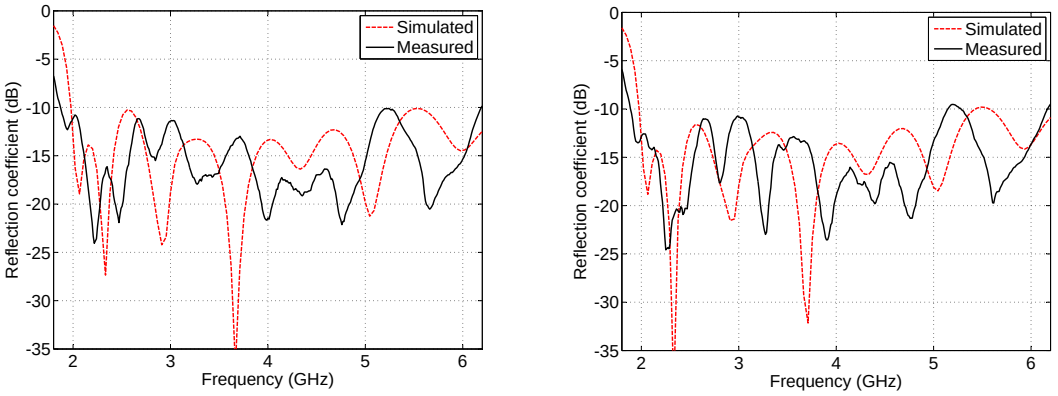

(a) Vertical polarisation. (b) Horizontal polarisation.

Figure 3.17: Simulated versus measured input reflection coefficients for both polarisations of the antenna.

The measured return loss is better than 10 dB for over a $3:1$ bandwidth from $1.9-6.2$ GHz.

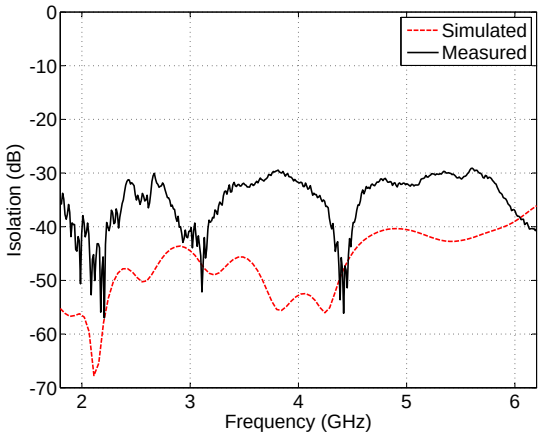

Figure 3.18: Simulated and measured isolation.

The measured isolation between the two polarisations, shown in Fig. 3.18, is well below -29 dB across the design bandwidth and a maximum deviation of 5.62%, in terms of magnitude, is observed when compared to the simulated isolation of a differentially fed antenna.

To verify the antenna's radiation characteristics, two techniques were used. In Technique I, signals from each of the two arms, for one polarisation, were combined at the difference port of a commercial 180° hybrid coupler [33], while all unused ports were terminated by 50 Ω loads. The hybrid has an amplitude and phase imbalance of 0.3 dB and 6° respectively. In Technique II, differential radiation patterns were extracted from single ended pattern measurements by applying basic circuit theory, where the differential mode (E^t_{dm}) and common mode (E^t_{cm}) patterns for the simplified antenna model illustrated in Fig. 3.19, are given by (3.4.1) and (3.4.2) [34],

$$E^t_{dm} = \frac{1}{\sqrt{2}}\Big(E^a(r,\theta,\phi) - E^b(r,\theta,\phi)\Big) \tag{3.4.1}$$

$$E^t_{cm} = \frac{1}{\sqrt{2}}\Big(E^a(r,\theta,\phi) + E^b(r,\theta,\phi)\Big) \tag{3.4.2}$$

where $E^a(r,\theta,\phi)$ is the obtained pattern due to the voltage excitation V_a, in Fig. 3.19, when V_b is replaced by a matched load. The same argument applies for $E^b(r,\theta,\phi)$ and V_b. The factor $(1/\sqrt{2})$, in (3.4.1) and (3.4.2), is introduced to account for the transmission coefficient of an ideal power combiner as given by network theory [35]. Essentially, single ended patterns are combined using an ideal, lossless and constant phase 180° hybrid coupler, implemented in software. This technique is applicable only if the there is symmetry between the two single ended ports.

The antenna's radiation pattern was measured as a two-dimensional ($2D$) scan in the $E-$ and $H-$planes, using a reference log periodic dipole array (LPDA) antenna that's characterised from $0.3-10$ GHz, in the university's anechoic chamber.

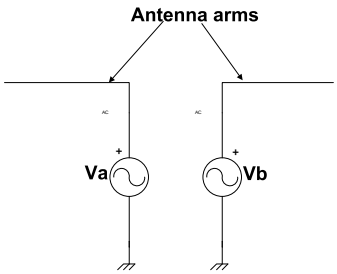

Figure 3.19: Simplified antenna model with single ended excitations.

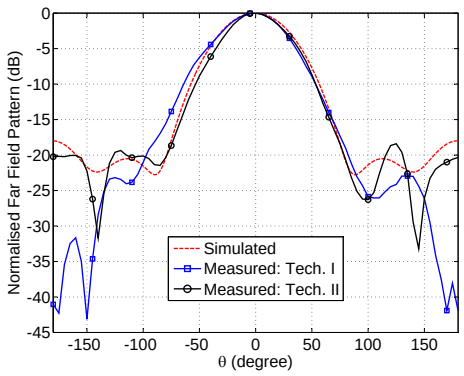

(a) 2 GHz.

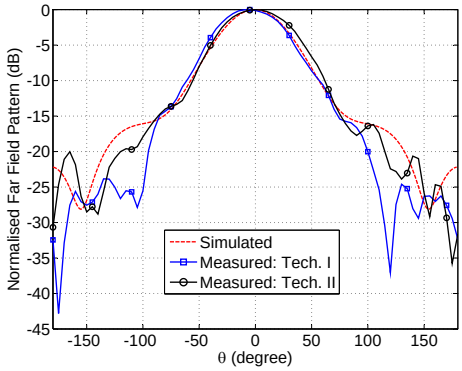

(b) 2.8 GHz.

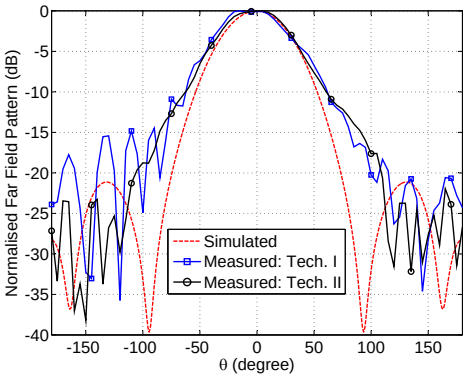

(c) 3.6 GHz.

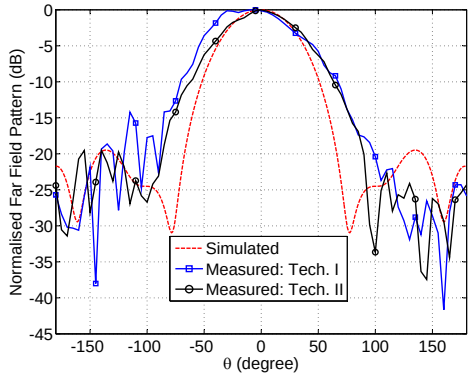

(d) 4.44 GHz.

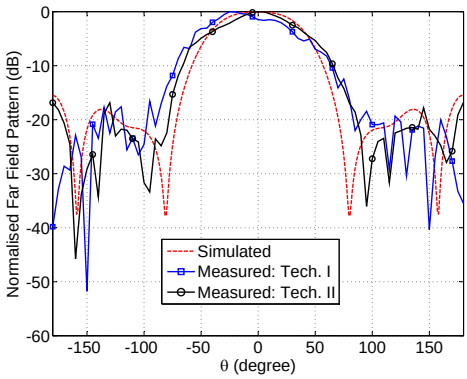

(e) 5.2 GHz.

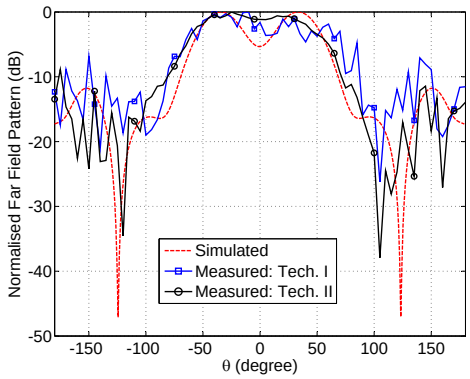

(f) 6 GHz.

Figure 3.20: Simulated and measured H-plane co-polar patterns at selected frequencies within the design's bandwidth.

The normalised simulated and measured H-plane patterns are shown in Fig. 3.20 at various frequencies within the band, revealing a relatively good agreement between

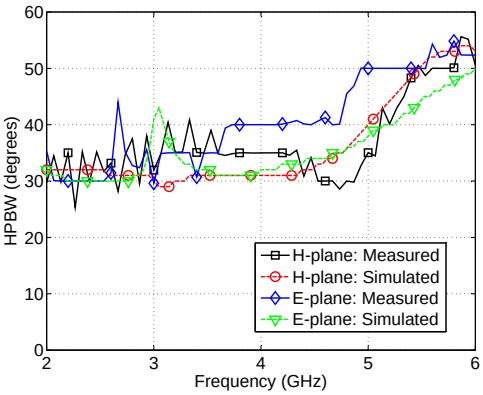

(a) Simulated versus measured HPBW.

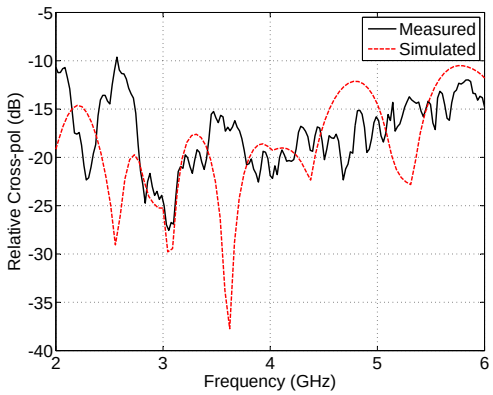

(b) Simulated versus measured relative cross-polarisation within the HPBW angle.

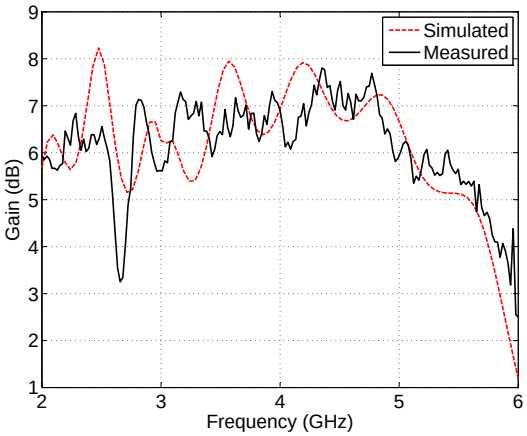

(c) Simulated versus Measured gain.

Figure 3.21: Measured radiation characteristics of the built antenna as a function of frequency.

simulated and measured patterns, as well as an experimentally demonstrated roundness of the main beam's pattern within $[-60°, 60°]$ except at the upper limit of the design bandwidth where a null at $\theta = 0°$ begins to form. It can also be seen in Fig. 3.20, that the patterns measured with both techniques do correlate, especially as far as the beam width is concerned. However, patterns measured with technique II are in much closer agreement with simulation results compared to those obtained with technique I. Also, more symmetrical and round main beam patterns are obtained with technique II, due to the phase and amplitude imbalances of the hybrid coupler used in technique I.

$E-$ and $H-$plane patterns are similar as illustrated by the simulated and measured HPBW plots in Fig. 3.21a, where both sets of curves reveal a widening main beam, from 30° to about 54°, as frequency increases.

The Measured cross-polarisation radiation is shown in Fig. 3.21b, where a higher relative cross-polarisation level, within the HPBW angle, is observed at lower frequencies when compared to the simulated results, also shown on the same plot. A maximum relative cross-polarisation of -9.63 dB is measured at 2.57 GHz. However a similarity between simulation and measurements is observed for frequencies higher than 2.8 GHz, with both simulation and measured results showing the same general trend of increasingly high cross-polarisation levels, with increasing frequency, to -10.5 dB and -12 dB for the simulated and measured relative cross-polarisation respectively.

A three antenna gain measurement method is used to accurately measure the planar antenna's gain. A comparison of the simulated[1] and measured gain is shown in Fig. 3.21c, where a generally good agreement is observed with a maximum deviation of 2 dB between simulated and measured value, at about 2.65 GHz. The maximum simulated gain of 8.2 dB compares favourably to the measured maximum gain of 7.8 dB.

Finally, the measured $E-$ and $H-$plane patterns are used to calculate the efficiencies of the built antenna when used as a feed for a prime focus paraboloidal reflector system with a subtended half-angle of 55°. Because the reference probe, used in measurements, is an LPDA with a phase centre that moves with frequency, phase efficiency results are erroneous especially for frequencies larger than 2.5 GHz. Thus the maximum phase efficiency of 87%, obtained from measured patterns at 2.02 GHz, was assumed for all frequencies. Another assumption made is that the BOR_1 efficiency, for all frequencies, is equal to the worst case value of 92%, obtained from simulations. The calculated efficiencies from the measured pattern are shown in Fig. 3.22b.

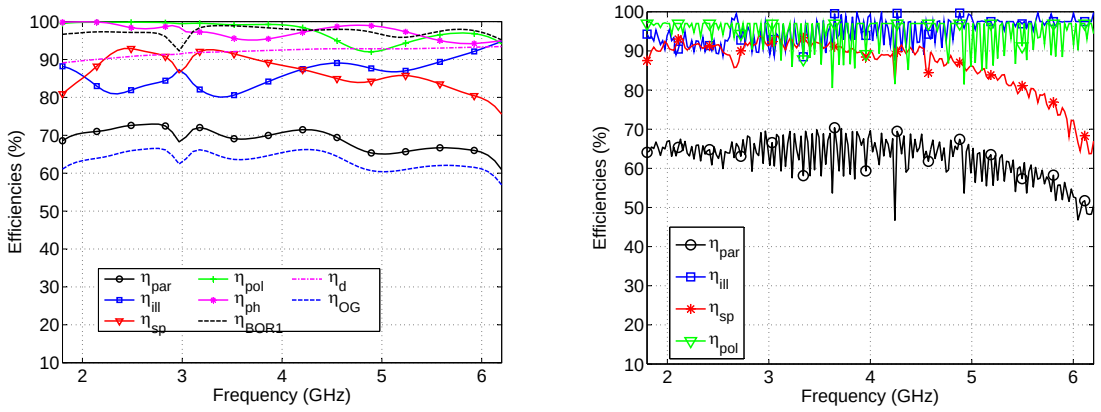

(a) Simulated Efficiencies.

(b) Measured Efficiencies.

Figure 3.22: Predicted feed efficiencies using simulated and measured radiation patterns for a paraboloidal reflector with $\theta_e = 55°$. The calculated aperture efficiencies are: η_{par} - aperture efficiency for a prime focus paraboloid; η_{OG} - aperture efficiency for an offset Gregorian system.

The aperture efficiency from measured patterns varies from $70 - 46\%$, with mean and median values of 62.4% and 64.4% respectively. A comparison between spillover efficiencies in Figs. 3.22a and 3.22b shows a similar trend of decreasing efficiency as frequency increases. This is due to the broadening of the main beam as shown in the HPBW plots of Fig. 3.21a. The illumination efficiency from measured pattern is larger than that in Fig. 3.22a as a result of the HPBW of the measured pattern being generally larger than that of the simulated pattern.

3.5 Performance as a Reflector Feed

To assess the antenna's performance in a reflector system, beyond the predictions of equations in section 2.2.1, a scaled model of the sinuous antenna with an operating frequency of $600 - 1800$ MHz was designed. The antenna's design parameters are listed in Table 3.5

[1] This is the realised gain obtained by accounting for mismatch and dispersion losses.

and a complete account of this particular antenna is given in [11].

Table 3.5: Scaled Antenna Parameters Values

Parameter	Design Value
α	29°
δ	15.9°
τ	0.83
h	70mm
Diameter	370.8mm

A spherical wave expansion of the antenna's radiation pattern was used to illuminate an offset Gregorian reflector system, similar to the proposed MeerKAT [5] telescope, with a projected aperture diameter of 13.5 m, an effective subtended angle of 55°, with the maximum chords of the reflectors being 15.85 m and 3.8 m for the main- and sub-reflectors respectively. The physical optics code GRASP [36] was used for reflector simulations. Fig. 3.23a shows the simulated aperture efficiency, which compares well to the predicted efficiency, shown on the same graph. The predicted aperture efficiency and sub-efficiencies are shown in Fig. 3.23b.

The reduction in efficiency around 850 MHz, for reasons discussed in section 3.3.3, is more clearly visible in the simulated results in Fig. 3.23a, with an average efficiency of just below 60% achieved over the 3:1 bandwidth. The drop in aperture efficiency at the high frequency end is a direct result of the increase in spillover as a result of widening main beam's width as frequency increases as shown in the −12 dB beam width plot in Fig. 3.24. The broadening of the main beam's width can not be significantly reduced without degrading return loss performance as discussed in section 3.2.1. The decrease in spillover efficiency at the high frequency end can be rectified by changing the reflector's optics using techniques such as the sub-reflector extension method described in [31].

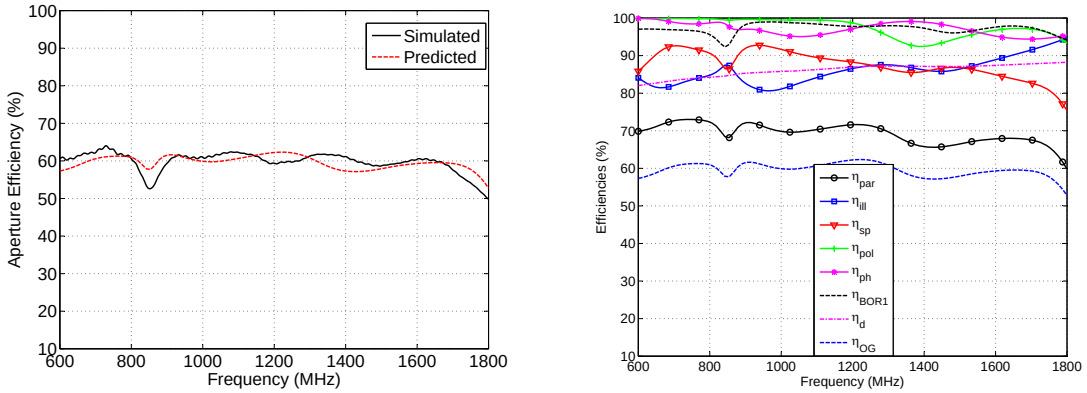

(a) (b)

Figure 3.23: (a) Comparison of aperture efficiencies predicted with efficiency integrals in [2] versus the GRASP simulated aperture efficiency of an offset Gregorian reflector system with the designed sinuous antenna as feed and an effective subtended half-angle of 55°. (b) Calculated aperture efficiency and sub-efficiencies for a subtended half-angle of 55° in a prime focus paraboloid (η_{par}) and offset Gregorian relector systems (η_{OG}).

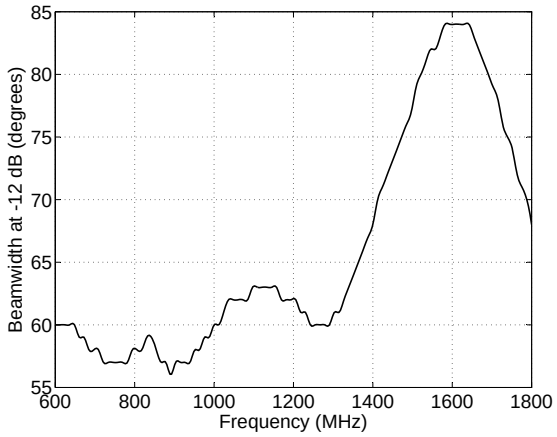

Figure 3.24: Beam width at the -12 dB level from the main beam's peak as a function of frequency, showing a broadening beam as frequency increases.

The first side lobe level (SLL) is shown in Fig. 3.25a, with the sharp increase around 850 MHz due to the beam broadening observed here in the spillover and illumination efficiency results in Fig. 3.23b. This effect should be carefully considered and analysed when designing low side lobe systems. An increase in SLL is also observed at the high end of the frequency band, as a result of the broadening beam width shown in Fig. 3.24. Simulation results discussed thus far in this section are based on a reflector system with a 55° effective subtended angle. Increasing the subtended angle produces slightly improved SLL performance at the low edge of the band through under-illumination. The SLL can, however, not be improved at the high end of the band without significantly degrading the efficiency performance, due to the severe beam broadening observed in Fig. 3.24.

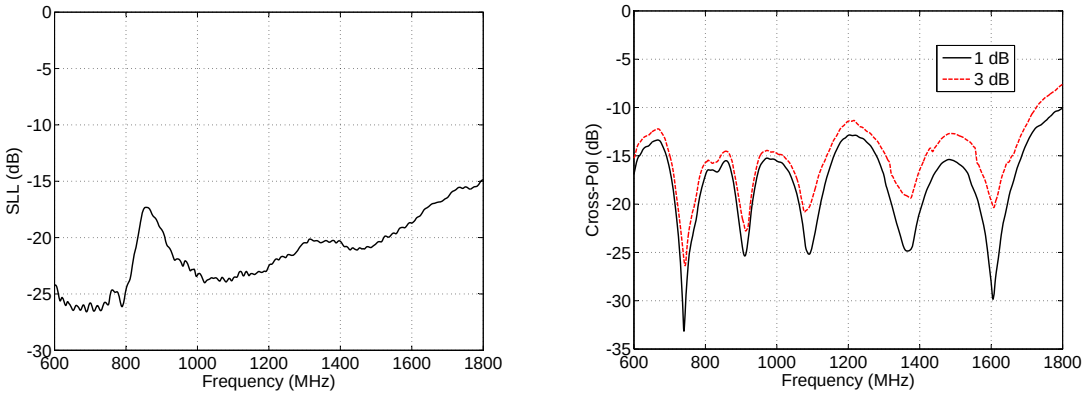

(a) (b)

Figure 3.25: (a) First side lobe levels as a function of frequency of an offset Gregorian reflector system with the designed sinuous antenna as feed. (b) Simulated cross-polarisation of the offset Gregorian system within 1 and 3 dB contours of the main beam's peak.

The cross polarisation performance is shown in Fig. 3.25b, with the levels defined within a 1 dB contour and a 3 dB contour of the main beam's peak. Even though the dishes are designed for zero cross polarisation, the relatively small electrical size causes a marked increase in the cross polarisation level from that observed in the feed pattern [11].

Finally a comparison of the radiometric noise performance between prime focus and offset Gregorian systems of equal projected main reflector diameter is shown in the tipping

curves in Fig. 3.26. For comparison purposes, the noise temperature is calculated using the simple model described in [37] where the ground noise is taken as 270 K, and the sky noise contribution is ignored. The improved performance of the offset Gregorian system is obvious, as well as the increase in noise temperature caused by the broader beam at high frequencies.

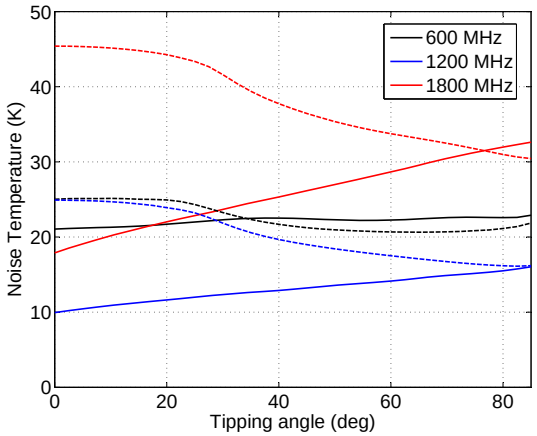

Figure 3.26: Comparison of noise temperatures of a prime focus paraboloid (Dashed lines) and offset Gregorian (Solid lines) reflector antenna illuminated by the sinuous feed, as a function of tipping angle.

Despite a predicted aperture efficiency larger than 58% when used to illuminate either a prime focus or offset Gregorian reflector system, high cross-polarisation and side lobe levels make this antenna unsuitable for use in applications with stringent requirements such as a high fidelity radio telescope feed.

3.6 Conclusion

In this chapter, a planar sinuous antenna is designed, built and evaluated as a feed for a reflector antenna. The antenna is designed to have unidirectional radiation without the use of absorbing materials. A thorough exploration of the design space is carried out and the precise effect of each of the design parameters on the antenna's response, as well as performance bounds on some key parameters are derived.

The designed antenna has a simulated aperture efficiency larger than 65% and 58% when used as a feed for a prime-focus paraboloid and offset Gregorian reflector systems respectively, as well as a measured return loss of 10 dB or better over a bandwidth ratio of more than $3:1$ from $1.9-6.2$ GHz. The return loss results represent a significant improvement over the octave bandwidth that is reported in literature [9] for a planar sinuous antenna without absorber backing.

It is worth mentioning that no optimisation whatsoever was attempted on this structure.

Despite the planar antenna being demonstrated to be ill suited as a feed for high fidelity reflector systems, its other characteristics such as a wide instantaneous bandwidth and a relatively good return loss make it an attractive option as a direct radiating element in applications such as ultra-wideband communication.

Chapter 4

Optimisation Framework

For problems in science and engineering, it is often impractical and expensive to directly experiment on the physical world or device. Instead, complex physics-based simulation codes are used to run experiments on a model of the device or experimental set-up of interest, on computer hardware. While this allows a great deal of flexibility to the engineer or scientist as far as running several experiments under highly controlled conditions is concerned, physics-based simulation codes require a substantial investment in computation time despite recent advances in High Performance Computation (HPC) and multi-core computer architectures. This is especially true for electromagnetic computations where simulation time varies anywhere from a few seconds to a few days depending on the complexity of the problem. Computation time is an even bigger concern for common engineering tasks like optimisation, sensitivity analysis and design space exploration where a large number of simulation runs are typically required.

This chapter focuses on a technique to alleviate optimisation and design space exploration tasks by creating a surrogate model, for the expensive full-wave computational electromagnetic (CEM) model, on which optimisation, design exploration and even sensitivity analysis can be carried out whilst requiring less (by several orders of magnitude) computational time and resources when compared to direct optimisation or space exploration on the actual (expensive) CEM model.

4.1 Surrogate Based Optimisation

Surrogate Based Optimisation (SBO) involves substituting a computationally expensive function to evaluate (e.g. finely meshed full-wave EM simulations), by an equivalent, computationally cheap surrogate model on which optimisation is carried out. Surrogate models are most often used to solve the so-called forward problem in which the practitioner is interested in the response characteristics of a complex system, given a set of input parameters [38].

The most commonly used SBO method in microwave engineering is Space Mapping (SM) [39, 40, 41]. Space Mapping involves constructing a computationally cheap model (usually a circuit model), of the EM device, on which optimisation is carried out and its optimised response is aligned with that of the computationally expensive and more

accurate model of the device. The cheap model is referred to as the *coarse* model whereas the computationally expensive model is called the *fine* model.

Other SBO techniques involve the use of statistical or data-driven surrogate models (also known as meta-models or response surface models). Examples of meta-models include rational functions [42], Gaussian Process (GP) models [43, 44], Radial Basis Functions (RBF) [45], Artificial Neural Networks (ANN) [46] and Support Vector Machines (SVM) [47]. A comprehensive account of response surface models and their application in a range of different scientific disciplines is given in [48].

Data-driven surrogate models have the advantage that the same simulation environment can be used to both generate the model and validate the model after it has been optimised. This is especially advantageous when dealing with a complex system where it is extremely difficult to derive a circuit model, as in SM; or when the optimisation practitioner does not have the required domain specific knowledge of the system being optimised or the system under consideration is simply not well understood. The latter case is referred to as a *black box* optimisation problem and meta-models are particularly well suited to solve such.

Amongst the above mentioned response surface models, this thesis focuses on GP models and in particular Kriging approximation models as they are easy to construct, only requiring standard statistical concepts, and are particularly robust even in the presence of noisy data from computer experiments or measurements[1]. The next section gives a detailed account of kriging meta-modelling.

4.2 Kriging Meta-modelling

Kriging meta-modelling was first described in 1951 by Danie Krige [43] while working on geostatistical problems related to the gold mines of the Johannesburg area of South Africa. A formal and rigorous mathematical description of kriging was described in 1963 by Matheron in [49] and this modelling approach has been common practice in geostatistics ever since. In modern statistics, Kriging is described as a subset of the broad range of Gaussian Processes.

Kriging is a form of an interpolation function that exploits the spatial correlation between data points in order to predict the overall function's behaviour at an arbitrary point. Therefore careful consideration of the type of correlation function used is necessary in order to improve the quality of the approximation. Different ways to build Kriging meta-models are described in [50], including the geostatistics approach, the original description as given in [43] and another approach based on Maximum Likelihood Estimates (MLE). The MLE approach is more suited for the Design and Analysis of Computer Experiments (DACE) because it is possible to exert some measure of control on the parameters of the correlation function. We proceed to describe the MLE approach to Kriging as it is relevant to our intended application (antenna optimisation).

[1] In this case, a simple moving averages procedure is first applied to the noisy data and Kriging meta-modelling can then be applied satisfactorily on the smoothed data.

A deterministic function $y(x)$ can be written in vector-matrix notation as

$$y(x) = f(x)^T\beta + z(x) \tag{4.2.1}$$

where $z(x)$ is the approximation error and x is an $m-$dimensional input vector. Strictly speaking, the function $f(x)$ should be the sole outcome of $y(x)$. However, the assumption in (4.2.1) is that a proper choice of β results in $z(x)$ behaving like white noise [51].

The function $y(x) = [y_1 \dots y_M]$ can then be approximated by its Kriging model as

$$\hat{y}(x) = F(x)\beta + Z(x), \quad \text{where } F(x) = f(x)^T \tag{4.2.2}$$

where $F(x)$ is an $M \times q$ matrix of regression polynomials (typically of low order[2]) and β is a $q \times 1$ vector of regression coefficients. $Z(x)$ represents all x of $y(x)$ not modelled by $\hat{y}(x)$ and thus represents the error between the true function and its Kriging approximation. It follows that if $\hat{y}(x)$ is continuous, then $Z(x)$ is also continuous since regression terms are always continuous. Unlike in regression analysis where neighbouring points are assumed to be uncorrelated, Kriging takes the relationship between neighbouring points into account. This relationship is embedded in the error function $Z(x)$ which is modelled as a random process with zero mean, non-zero covariance and a variance given by σ^2.

The distance between sample points is defined as a weighted Euclidean distance given by

$$d(x^i, x^j) = \sum_{k=1}^{m} \theta_k \left| x_k^i - x_k^j \right|^p, \quad \text{where } p \in \{1, 2\}, \tag{4.2.3}$$

and the correlation function between two sample points is given by

$$R(x^i, x^j) = \exp(-d(x^i, x^j)) = \prod_{k=1}^{m} e^{-\theta_k \left| x_k^i - x_k^j \right|^p}, \quad \text{where } p \in \{1, 2\}, \tag{4.2.4}$$

while the covariance is given by

$$E\left[Z(x^i)Z(x^j)\right] = \sigma^2 R(x^i, x^j), \tag{4.2.5}$$

where $E[\cdot]$ is the standard statistics definition of the expectation of a random variable.

A few important facts about the expression in (4.2.4) are discussed below:

1. $\left| x_k^i - x_k^j \right|$ is the Euclidean distance between the points x^i and x^j for the k^{th} variable of the vector x.

2. The correlation function for all m variables is defined as the product of the correlation functions of the individual variables, thus accounting for the interaction between all variables in the input vector x. It can easily be seen in (4.2.4) that a high correlation is obtained if x^i and x^j are close and a low correlation if they are far apart.

[2] The order of the polynomial is dictated by q, where $q = 1$ when regression polynomials are constants (i.e. $F(x) = ones(M, 1)$); $q = 2$ for first order polynomials and $q = 3$ for second order polynomials.

3. θ_k is a positive parameter and its value indicates the impact of a variable x_k, in x, on the behaviour of the function such that, a low correlation may be obtained if θ_k is large, even if two neighbouring points are very close together as illustrated in Fig. 4.1. That is, for a high impact variable x_k, very small values of the Euclidean distance between neighbouring points, $\left|x_k^i - x_k^j\right|$, result into large differences in the function values at x_k^i and x_k^j. Thus, the corresponding value of θ_k needs to be large, enforcing low correlation, to account for such an impact of x_k on the function. In essence, the value of θ_k indicates whether the modelled function is fast varying between x_k^i and x_k^j.

4. The value of p simply specifies what kind of correlation function is being used, with $p = 1$ and $p = 2$ corresponding to an exponential and Gaussian correlation functions respectively.

5. The definition of the correlation function captures enough information about the impact and distribution of input variables x, such that the regression term in (4.2.2) can be modelled by a constant vector β without losing much accuracy as shown in Fig. 4.3d.

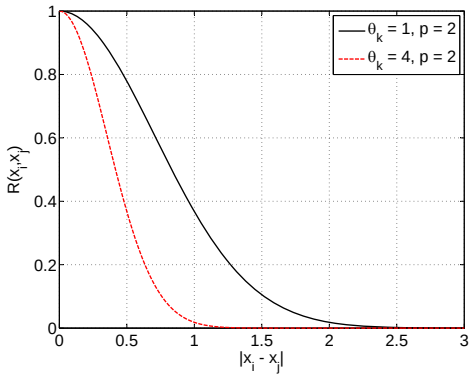

Figure 4.1: Effect of the θ_k on the correlation function in eq. (4.2.4).

In subsequent sections, methods for building a Kriging model and making predictions based on the model, are discussed in depth.

4.2.1 General Solution

Consider a weighted prediction $\hat{y} = c^T Y$, where c^T is the weighting vector and Y is a random process given by (4.2.2). The error between the prediction and the true function is

$$\begin{aligned} \hat{y}(x) - y(x) &= c^T(F(x)\beta + Z(x)) - (f(x)^T\beta + z(x)) \\ &= c^T Z(x) - z(x) + \beta(F(x)^T c - f(x))^T \end{aligned} \tag{4.2.6}$$

In what follows, the $x-$dependence of $\hat{y}, y, f, F$ and Z is assumed and $y(x)$ is thus simply written as y, ditto for $\hat{y}, f, F$ and Z.

Minimising the effect of the weighting factor on the error in (4.2.6) requires that $F(x)^T c - f(x) = 0$. Taking this constraint into account, the mean square error of the Kriging prediction becomes

$$\begin{aligned}\hat{s}^2 &= E[(\hat{y} - y)^2] \\ &= E[(c^T Z - z)^2] \\ &= E[z^2 - 2c^T Zz + c^T ZZ^T c] \\ &= E[z^2] - 2E[c^T Zz] + E[c^T ZZ^T c] \\ &= \sigma^2(1 - 2c^T r + c^T Rc)\end{aligned} \tag{4.2.7}$$

where R is the correlation between pre-existing input sample points, x, and r is the correlation between the new sample, the Kriging model is being evaluated at, and the pre-existing input samples.

To minimise the mean square error in (4.2.7), subject to $F^T c - f = 0$, the required Lagrangian functional is given by

$$L(c, \lambda) = \sigma^2(1 + c^T Rc - 2c^T r) - \lambda^T(F^T c - f), \tag{4.2.8}$$

where λ is the Lagrange multiplier, and its derivative with respect to c is easily found using matrix calculus as

$$\frac{\partial L(c, \lambda)}{\partial c} = 2\sigma^2(Rc - r) - F\lambda. \tag{4.2.9}$$

The Karush-Kuhn-Tucker (KKT) conditions [52] for optimality, with respect to the weighting factor c, of this problem are

$$\begin{aligned}\frac{\partial L(c, \lambda)}{\partial c} &= 0. \\ \lambda(F^T c - f) &= 0.\end{aligned}$$

Solving the KKT conditions gives

$$\begin{aligned}\hat{\lambda} &= (F^T R^{-1} F)^{-1}(F^T R^{-1} r - f) \\ c &= R^{-1}(r - F\hat{\lambda}) \\ \hat{\lambda} &= -\frac{\lambda}{2\sigma^2}\end{aligned} \tag{4.2.10}$$

and the prediction $\hat{y} = c^T Y$ is thus found as

$$\begin{aligned}\hat{y} &= (r - F\hat{\lambda})^T R^{-1} Y \\ &= r^T R^{-1} Y - (F^T R^{-1} r - f)^T (F^T R^{-1} F)^{-1} R^{-1} F,\end{aligned} \tag{4.2.11}$$

since R is a symmetric matrix and the mean square error expression in (4.2.7) is then found by substituting (4.2.10) into (4.2.7) as [53]

$$\hat{s}^2 = \sigma^2 \left[1 - r^T R^{-1} r + \frac{(f - F^T R^{-1} r)^2}{F^T R^{-1} F}\right]. \tag{4.2.12}$$

4.2.2 Generalised Least Squares Solution

Consider the Kriging model in (4.2.2) and the following cases:

1. Assume that the different sample values are uncorrelated and have the same variance. Since $Z(x)$ is said to have zero mean and covariance given by (4.2.5), then $\sigma^2 = 0$ since input variables are uncorrelated and $R = I$, the identity matrix. (4.2.2) then reduces to

$$Y = F\beta, \tag{4.2.13}$$

and the least squares solution of β is found as

$$\begin{aligned} F^T Y &= F^T F\beta \\ \beta &= (F^T F)^{-1} F^T Y. \end{aligned} \tag{4.2.14}$$

2. Assume that the different sample values are uncorrelated and have different variance, such that $E[Z(x_i)Z(x_i)] = \sigma_i^2$ and $E[Z(x_i)Z(x_j)] = 0$. Here the correlation function is then given by the diagonal matrix

$$R = \text{diag}\left(\frac{\sigma_1^2}{\sigma^2} \dots \frac{\sigma_m^2}{\sigma^2}\right), \tag{4.2.15}$$

from the formula of covariance in (4.2.5).

For the weighted prediction $\hat{y} = c^T Y$, with c^T chosen such that $(c^T)^2 = R^{-1}$ [51] i.e. $(c^T)^2 = \text{diag}\left(\frac{\sigma}{\sigma_1} \dots \frac{\sigma}{\sigma_m}\right)$, the mean of the weighted error is still equal to zero, and its covariance is given by

$$\begin{aligned} E[Z_w Z_w^T] &= E[c^T Z c Z^T] \\ &= c^T E[ZZ^T]c = \sigma^2 I, \end{aligned} \tag{4.2.16}$$

and thus resulting in a situation similar to case 1. Thus β is found as the least squares solution of

$$\begin{aligned} c^T Y &= c^T F\beta \quad \text{as} \\ \beta &= (F^T R^{-1} F)^{-1} F^T R^{-1} Y. \end{aligned} \tag{4.2.17}$$

3. The arbitrary case where the errors are correlated and the correlation matrix, R, is not diagonal, the covariance of the weighted Kriging prediction is given by $E[Z_w Z_w^T] = E[c^T Z c Z^T] = \sigma^2 c^T R c$. Since R is a symmetric matrix and the covariance is positive for $c \neq 0$, R can then be factorised into its Cholesky factors as $R = C^T C$ [51] (i.e. C is an upper or lower triangular matrix). By choosing $c^T = C^{-1}$, the covariance expression becomes similar to (4.2.16) and β is then given by

$$\beta = (F^T C^{-1} C^{-T} Y)/(F^T C^{-1} C^{-T} F). \tag{4.2.18}$$

Knowing the expression for β, the least squares expression for a Kriging prediction is obtained by substituting (4.2.18) into (4.2.11) to give

$$\begin{aligned}\hat{y} &= r^T R^{-1} Y - (F^T R^{-1} r - f)^T \beta \\ &= f^T \beta + r^T R^{-1}(Y - F\beta),\end{aligned} \tag{4.2.19}$$

and the generalised least squares solution of an arbitrary Kriging prediction is thus given by (4.2.19).

4.2.3 Maximum Likelihood Estimation

Sections 4.2.1 and 4.2.2 presented ways of evaluating the Kriging prediction and solving for the regression parameter respectively. However, the full Kriging model is not complete as there are still important unknowns such as the variance (σ^2), necessary to determine the prediction error in (4.2.6), and the value of the parameter θ, in the correlation function in (4.2.4).

The variance is found by Maximum Likelihood Estimate (MLE), described as follows: if the Kriging prediction is treated as the realisation of a normally distributed random variable $Y = [y_1 \dots y_M]$, i.e. Y (see eq. (4.2.2)) is a random variable with M known samples (true function samples), the MLE of variance is obtained by maximising the Probability Density Function (PDF) of Y and is given by

$$\begin{aligned}\text{Maximise} \quad & \prod_{i=1}^{M} \frac{1}{\sqrt{2\pi\sigma^2}} e^{-\frac{(y_i - f\beta)^2}{2\sigma^2}} \\ \text{Maximise} \quad & \left(\frac{1}{\sqrt{2\pi\sigma^2}}\right)^M e^{-\frac{1}{2\sigma^2}\sum_i^M (y_i - f\beta)^2}.\end{aligned} \tag{4.2.20}$$

The variance is found by equating the derivative of (4.2.20) with respect to σ to zero and solving the resulting equation for σ, giving

$$\sigma^2 = \frac{1}{M}\sum_{i=1}^{M} (y_i - f\beta)^2, \tag{4.2.21}$$

which is written in vector-matrix notation as

$$\sigma^2 = \frac{1}{M}(Y - F\beta)^T (Y - F\beta), \tag{4.2.22}$$

for the simple case where the sample values are uncorrelated (see case 1 in section 4.2.2). As was shown in case 3 of section 4.2.2, for the arbitrary case where there is correlation, the least squares solution was found by scaling the prediction with the inverse of the correlation matrix R. Thus the MLE variance expression for an arbitrary Kriging prediction is simply found by replacing Y and F in (4.2.22) by their scaled versions $R^{-1}Y$ and $R^{-1}F$ respectively, giving the general expression of MLE variance as

$$\sigma^2 = \frac{1}{M}(Y - F\beta)^T R^{-1} (Y - F\beta). \tag{4.2.23}$$

Similarly, the value of θ is obtained by maximising the PDF of the correlated sample values as

$$\text{Maximise} \quad \left(\frac{1}{(\sqrt{2\pi\sigma^2})^M |R|}\right) \exp\left\{-\frac{1}{2\sigma^2}(Y - F\beta)^T R^{-1}(Y - F\beta)\right\}. \tag{4.2.24}$$

Substituting (4.2.23) into (4.2.24) gives

$$\text{Maximise} \quad \left(\frac{1}{(\sqrt{2\pi\sigma^2})^M |R|}\right) \exp\left\{-\frac{M}{2}\right\}$$

which, by taking the logarithm and ignoring constant terms, becomes

$$\text{Maximise} \quad -\frac{M\ln(\sigma^2) + \ln(|R|)}{2}, \tag{4.2.25}$$

where σ^2 and R are functions of θ given by (4.2.23) and (4.2.4) respectively and $|R|$ is the determinant of the correlation matrix R.

The Kriging models in this thesis are built using the popular and freely available DACE Matlab Kriging toolbox [51] and an implementation of the simple method in [54] , in which computationally tractable versions of the theoretical Kriging expressions derived in this chapter are used to efficiently handle the case where a Kriging model of large data sets is being built or when the correlation matrix R is ill-conditioned. Some numerical subtleties are highlighted in Appendix A.

4.2.4 Kriging Example

To demonstrate the effectiveness of Kriging meta-modelling, the Kriging model of the simple $y = \sin(x)$ function is presented in a chronological manner, with $x \in [0, 360]$. For simplicity, we begin by building a Kriging model with 3 sample points $x \in \{85, 150, 235\}$, where the regression polynomials are set to 1. The known parameters in (4.2.2) are: the input vector is $x = [85, 150, 235]$, the output vector $Y = [0.9962, 0.5, -0.819]$ and $F(x) = [1, 1, 1]$. The Kriging model is then derived as follows :

1. The first step of Kriging meta-modelling is to normalise all data by subtracting the mean and dividing by the standard deviation for each variable in x and $y(x)$ as

$$D_n = \frac{D - \mu}{\sigma}, \tag{4.2.26}$$

where D_n and D are the normalised and raw data respectively, and μ and σ are the mean and standard deviation of D respectively. (4.2.26) consists of a mapping of the raw data to a distribution with zero mean and a standard deviation of 1, which has better numerical and statistical properties [51]. This step guarantees more accurate solutions when a model of a large data set is being constructed or when the system is ill-conditioned. It is however not a mandatory step. Equations derived in the previous 3 sections can generally be directly applied to the raw data D without severe loss of accuracy. Experiments showed this to be the case for problems with dimension $\geqslant 2$.

2. The pair-wise Euclidean distances between input data points are computed and (4.2.25) is maximised using a standard constrained optimisation function. For this example $\theta = 0.3937$.

3. Having found θ, the correlation matrix, R, between known input data points is computed from (4.2.4) as

$$R = \begin{bmatrix} 1 & 0.6271 & 0.0833 \\ 0.6271 & 1 & 0.4502 \\ 0.0833 & 0.4502 & 1 \end{bmatrix} \tag{4.2.27}$$

and β is then found by factorising R and solving (4.2.18) to give $\beta = -0.2241$. The variance is then found in a straight forward manner as $\sigma^2 = 0.7807$.

4. The Kriging model thus constructed can be used to predict function values at untried sites by solving (4.2.19) where r^T is the correlation between the untried point x^* and known data points $x_1, \cdots, x_n$ and is given by

$$r^T = [R(x^*, x_1) \cdots R(x^*, x_n)]^T, \tag{4.2.28}$$

where $R(\cdot, \cdot)$ is the correlation function given by (4.2.4). Evaluating the Kriging model at $x^* = 50$ gives $r^T = [0.918, 0.499, 0.092]^T$ and the predicted function value is $\hat{y} = 0.8803$, as calculated from (4.2.19).

5. Finally, a measure of error in the prediction is found in a straight forward manner from (4.2.12) as $\hat{s}^2 = 0.00585$.

The model's prediction for the entire domain, its predicted mean square error (MSE) as well as the true function are shown in Fig. 4.2, where a large MSE is observed for values of $x < 85$ and $x > 235$. Also, the distribution of the sample points is such that the variation of the function is not accurately captured by the correlation hyper-parameter θ. This fact combined with the large value of σ^2 result in excessively large MSE outside the range of the 3 sample points and thus calls for an increase in the number of samples.

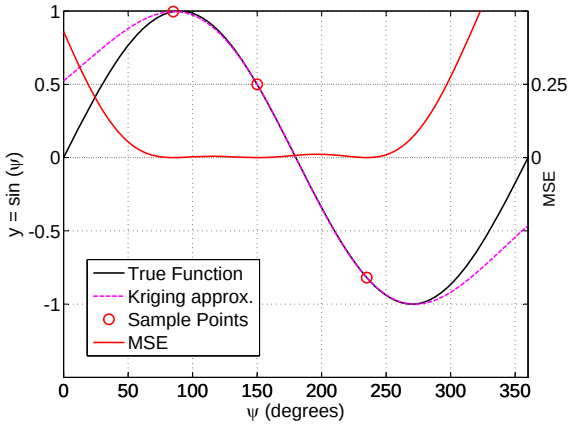

Figure 4.2: Kriging prediction of the sine function from 3 sample points.

A design with $x \in \{85, 150, 235, 340\}$, shown in Fig. 4.3b, gives an improved variance of $\sigma^2 = 0.54522$, which, in combination with $\theta = 0.9921$, result in an improved fit as illustrated by the reduction in MSE, also shown on the same graph. Finally, a model with near zero MSE is obtained with $x \in \{15, 85, 175, 230, 250, 340\}$, as shown in Fig. 4.3c.

It is demonstrated that for a poor distribution of samples, a Kriging model obtained by setting the regression functions to constants, performs better than one constructed with low order polynomials (i.e. 1^{st} or 2^{nd} order) as shown in Fig. 4.3 where the values of θ are 0.625 and 20 for the model in Fig. 4.3b and Fig. 4.3a respectively. The plotted MSE values as well as the values of θ indicate a better fit for the model with constants as regression functions. Therefore Kriging models with constants as regression terms were used throughout the optimisation of the antenna, described in chapter 5.

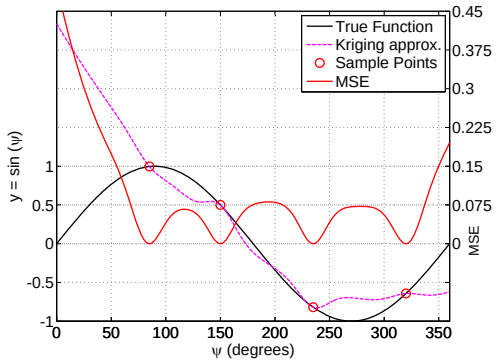

(a) Poor fit obtained with 2^{nd} order regression polynomials.

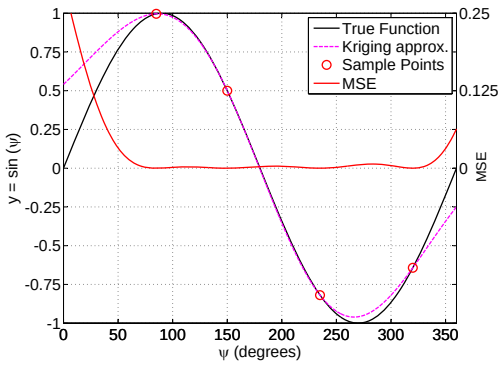

(b) Improved fit with constants as regression functions.

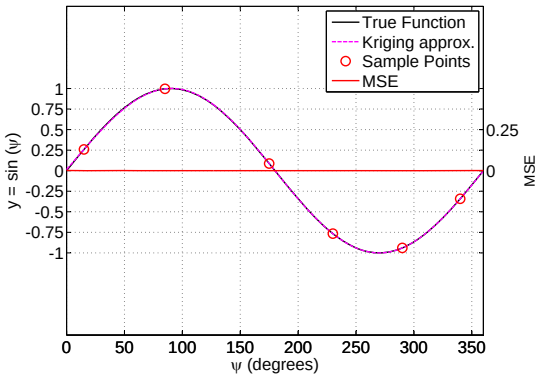

(c) Good fit.

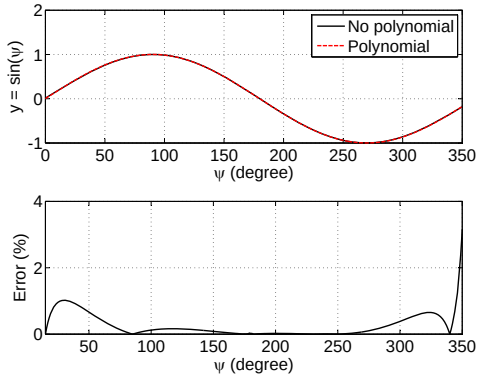

(d) Comparison of different MLE Kriging models.

Figure 4.3: Kriging meta-models of the sine function. It is shown in (d) that for a well sampled model (such as in (c)), an implementation with $F(x)$ in eq. (4.2.2) being a set of n regression polynomials (n is the number of sample points); and one where $F = 1$, the error is less than 3% in the entire domain.

Fig. 4.3d shows two Kriging models of the sine function: one built with 2^{nd} order regression polynomials and the other with constants as the regressions functions. Both models are built using the same sample points as for the good fitting model in Fig. 4.3c. Fig. 4.3d reveals the error between the two Kriging approaches to be less than 3% across the range of the input variable.

Though the example presented here is a very simple one, Kriging can be used to create models of functions with up to 20 variables and 10000 data points [38]. A more

complex example of a Kriging model is given in section 4.4 where the function's samples are determined by an infill criterion described hereafter.

4.3 Surrogate-based Infill Optimisation

Surrogate models can be built upfront to accurately mimic the performance of the physics-based simulation code over the entire design space. They can then be used for optimisation afterwards. Another approach to building surrogate models includes the model building process in the optimisation loop, such that the expensive function evaluations are done at the optimum values of the surrogate model. The surrogate model is then updated with new results from the physics-based simulator in an iterative manner as shown by the flowchart in Fig. 4.4. The criterion used to select new points to evaluate the expensive function at, is called an *infill sampling* criterion.

The former approach requires a dense sampling grid for all variables involved and in some cases, a priori knowledge of the underlying system's behaviour in order to accurately model the system in question. This approach is disadvantageous in that it requires significantly more computation time to construct an accurate model. However its advantage lies in the fact that the built surrogate model can be used to optimise the system for different cost functions.

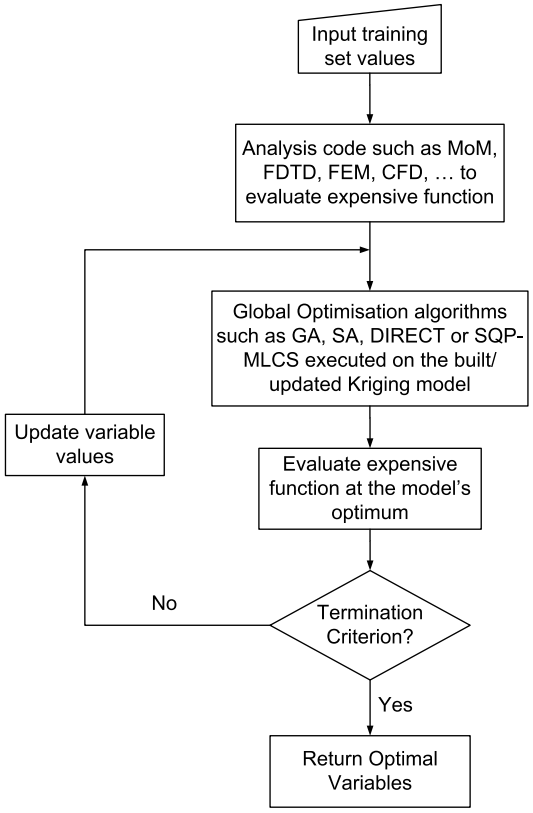

Figure 4.4: Flowchart of surrogate based optimisation of complex systems. The algorithms listed are: Genetic Algorithm (GA), Simulated Annealing (SA), DIviding RECTangles (DIRECT) and Sequential Quadratic Programming (SQP). SQP is combined with a multi-level coordinate search (MLCS) method for global optimisation [3].

The latter approach is significantly more efficient, in terms of computation time. At first glance, integrating model building in the optimisation loop may seem to favour *exploitation* (i.e. focusing on model accuracy around the optimum of a given cost function) over *exploration* (i.e. building a globally accurate surrogate model). However, the efficient algorithm in [53] uses the revolutionary concepts of Expected Improvement (EI) and Probability of Improvement (PoI) to build an optimised globally accurate surrogate model, striking a perfect balance between exploitation and exploration of the design space.

If the prediction from the surrogate model at a sample point x is treated as the realisation of a normally distributed random variable $Y(x)$ with prediction mean square error $\hat{s}^2$, then the PoI evaluates the likelihood that the predicted value is better than the current minimum f_{min}. In essence, the PoI evaluates the cumulative distribution function (CDF) of the random variable $Y(x)$ as

$$\begin{aligned} PoI(x) &= P\{Y(x) \leq f_{min}\} = \int_{-\infty}^{f_{min}} Y(x)dY \\ &= \Phi\left(\frac{f_{min} - \hat{y}}{\hat{s}}\right) \end{aligned} \tag{4.3.1}$$

where $\Phi(\cdot)$ is the CDF of $Y(x)$ and is given by

$$\Phi(t) = \frac{1}{2}\left[1 + \text{erf}\left(\frac{t}{\sqrt{2}}\right)\right], \tag{4.3.2}$$

where $\text{erf}(\cdot)$ is the standard error function given by

$$\begin{aligned} \text{erf}(x) &= \frac{2}{\sqrt{\pi}}\int_0^x e^{-t^2}dt, \quad \text{which is expanded as} \\ \text{erf}(x) &= \frac{2}{\sqrt{\pi}}\left[x - \frac{x^3}{3\cdot 1!} + \frac{x^5}{5\cdot 2!} - \frac{x^7}{7\cdot 3!} + \cdots\right]. \end{aligned} \tag{4.3.3}$$

While the PoI measures the likelihood of finding a better minimum, it does not quantify how much better the new minimum is compared to the function's current minimum and thus poses a selection problem when several candidate points yield a prediction better than f_{min}. The EI resolves this selection problem by calculating the first moment of the improvement $I(x)$ of the random variable $Y(x)$ as

$$E[I(x)] = \int_{-\infty}^{f_{min}} I(x)Y(x)dY \tag{4.3.4}$$

where

$$I(x) = \max(f_{min} - Y(x), 0) \tag{4.3.5}$$

In essence, the EI criterion assigns weights to the PoI of different candidate points, with the point with the highest PoI being assigned the highest weighting factor.

Applying integration by parts to the expression in (4.3.4) yields the closed form expression for EI given by [48, 53]

$$E[I(x)] = \begin{cases} (f_{min} - \hat{y})\Phi\left(\frac{f_{min} - \hat{y}}{\hat{s}}\right) + \hat{s}\phi\left(\frac{f_{min} - \hat{y}}{\hat{s}}\right) & \text{if } \hat{s} > 0 \\ 0 & \text{if } \hat{s} = 0 \end{cases} \tag{4.3.6}$$

where $\phi(\cdot)$ is the probability density function (PDF) of a normally distributed random variable given by

$$\phi(t) = \frac{1}{\sqrt{2\pi}} \exp\left\{-\frac{t^2}{2}\right\}, \tag{4.3.7}$$

and $\Phi(\cdot)$ is the CDF given by (4.3.2).

It is easily seen that the closed form EI expression in (4.3.6), is maximised if the prediction, $\hat{y}$, from the Kriging model, is better than the current true function's minimum f_{min} or if there are large uncertainties in the Kriging model $Y(x)$, depicted by a large prediction root mean square error $\hat{s}$, as illustrated in Fig. 4.5a where uncertainties are depicted by the shaded region around the Kriging model's prediction mean. Thus, the first term of (4.3.6) is responsible for the *exploitation* part of the algorithm while the second term is responsible for the *exploration* part, which is accomplished by space filling. It can also be noticed in the EI expression in (4.3.6) that the prediction mean ($\hat{y}$, the actual outcome of the evaluated Kriging model at an untried site) and deviation ($\hat{s}$) of $Y(x)$ are required to determine the expected improvement of a new sample point x. This fact makes Kriging meta-modelling very attractive for EI implementations as the prediction mean and mean square error estimates are its by-products.

The goal of EI is thus to find the value of x that maximises (4.3.6). The prediction x that maximises (4.3.6) is found by either using a grid-search approach or using a global optimiser such as the dividing rectangles (DIRECT) algorithm in [44] or a genetic algorithm as in [54]. It must be noted that a local optimisation routine is not desirable to solve for the prediction that maximises EI because the expression in (4.3.4) is typically a function with many local maxima as demonstrated in [53]. Thus using EI as an infill sampling criterion results in a densely sampled model in the region around the optimum and sparse sampling in regions where the function varies slowly, as shown in Fig. 4.5. It is this nature of the EI expression in (4.3.4) that makes both exploitation and exploration of the design space possible, making the EI algorithm useful for optimisation, design space exploration as well as sensitivity analysis.

To illustrate, in a clear manner, the concepts discussed thus far, EI infill sampling is applied to the simple $y = \sin(x)$ function, shown in Fig. 4.5. EI is computed for all values in the domain and the point with maximum improvement is selected to evaluate the sine function at. For clarity, EI values are shown in Figs. 4.5c and 4.5d for the first two sample distributions in Figs. 4.5a and 4.5b respectively. The optimum is found after only four iterations , at which point the error between the analytical function and its Kriging model is below 2.29% as shown in Fig. 4.6. Subsequent iterations of the EI algorithm further improve the global accuracy of the model to an error less than 0.03%, after which the algorithm is terminated. Fig. 4.5f is typical of models constructed with EI, with dense sampling around the optimum while the function is sparsely sampled elsewhere.

The Kriging predictions in Fig. 4.5 are built using the DACE Toolbox [51], while data points are selected using an implementation of Kriging and EI according to [54].

The effectiveness of EI is further illustrated in the rapidly decreasing error function, at an initial rate of about 10% per new sample, such that the error is already below 5% when the function's minimum is found, enforcing the reliability of results obtained with

EI.

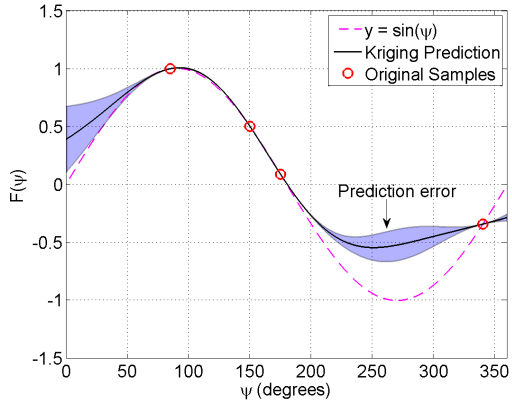

(a) Model with initial samples.

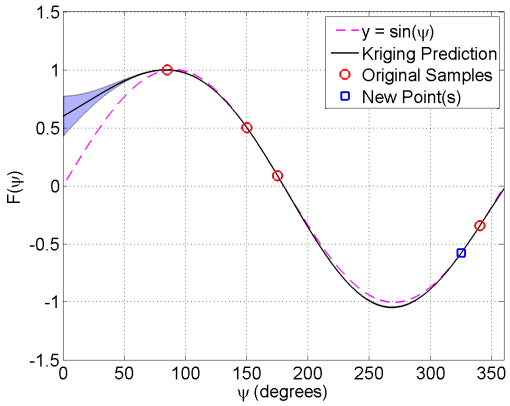

(b) 1 new sample point.

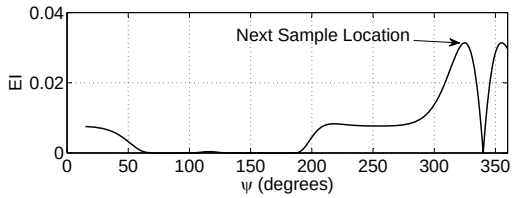

(c) EI Values from original distribution.

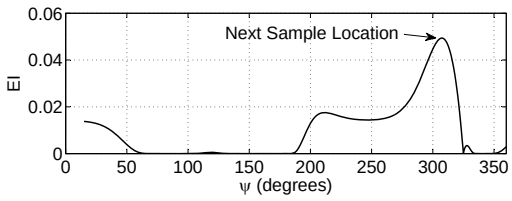

(d) EI Values after one new sample.

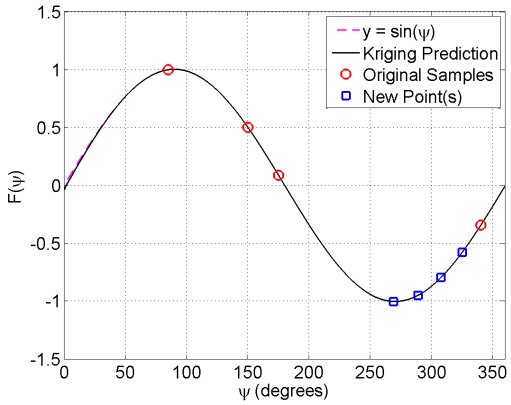

(e) 4 new sample points (Minimum found).

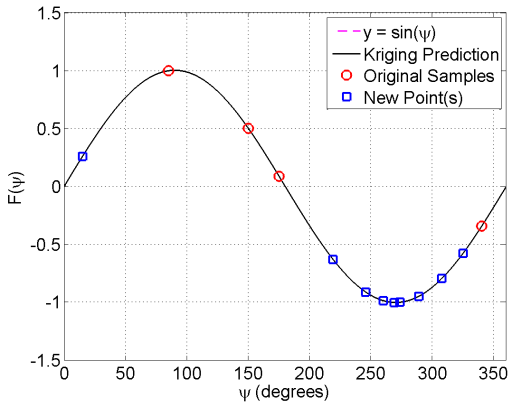

(f) Final model (9 new samples).

Figure 4.5: Reconstruction of the sine function with EI guiding the selection of new samples. Notice the density of samples around the minimum (which is found after 4 iterations), and the sparsity of sample points elsewhere.

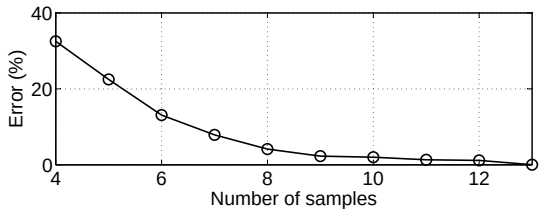

Figure 4.6: Maximum error between the Kriging model and the true function as a new samples are continuously added by means of EI.

It is important to mention that EI is only applicable to minimisation problems and any maximisation will have to be cast as a minimisation problem in order to use EI as an infill optimisation criterion.

A complete mathematical account of expected improvement as well as a step by step guide towards its implementation in software is given in [54].

4.4 Design and Analysis of Computational Experiments

The computational experiment of interest in this thesis is optimisation. More precisely a data-driven SBO approach to optimising an antenna for various goals, using kriging meta-modelling coupled with expected improvement as described in sections 4.1 and 4.3, is of concern here. This section describes the steps necessary for successful data-driven SBO.

4.4.1 Model Training

An efficient strategy in SBO is to have a preliminary model built up-front from a limited number of unbiased simulations that are representative of the complete design space. This preliminary model is then used in the optimisation loop as shown in Fig. 4.4. This step is necessary in order to ensure the accuracy of the surrogate model and its predictions during the initial stages of the optimisation. In this thesis, this stage is referred to as the *training* stage.

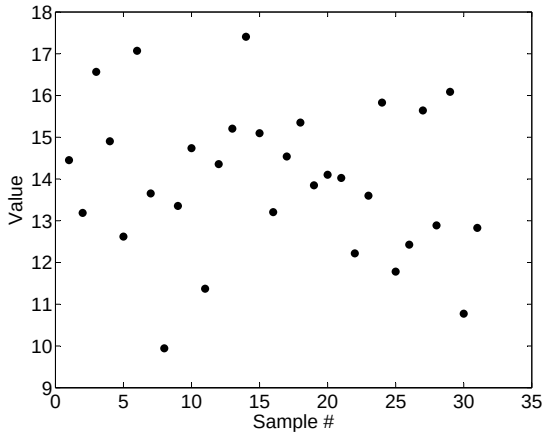

Figure 4.7: 31 samples generated with LHS for a variable with a mean of 14 and a standard deviation of 1.75.

As was shown for the simple case of a sine function in Fig. 4.3 and Fig. 4.5, it is of utmost importance to properly sample the design space in order to obtain an accurate model and improve its convergence rate towards the minimum. A near optimal unbiased collection of initial data is accomplished using Latin Hypercube Sampling (LHS) [48]. LHS provides an efficient way of randomly sampling variables from their distributions. Given the mean and standard deviation of a variable, the LHS algorithm generates n random numbers centred around the variable's mean as illustrated in Fig. 4.7. A Latin hypercube is constructed by dividing each dimension in the design space into n equally sized intervals

(or having the intervals sized according to a normal distribution) and placing exactly one point in each interval for each dimension.

The idea is to generate a sufficient number of samples for the variables on which optimisation will be carried out and use the simulation code to evaluate the expensive function at those points. The advantage of this approach is that this initial data collection stage is only done once and subsequent optimisations will be considerably faster and more accurate.

The minimum number of samples required to build the initial unbiased model is strongly dependent on the computational experiment under consideration and should typically be kept small. A rule of thumb for the required number of training samples is given in [53] as

$$n = 11k - 1 \tag{4.4.1}$$

where k is the number of variables to be optimised and n is the total number of training samples.

4.4.2 Cost Function Selection

The next and perhaps most important stage in any optimisation problem is selecting the cost function. This step is important in that it has direct implications on how well the optimisation algorithm performs. Further, it is important to incorporate a measure of how important an optimisation goal is into the cost function. i.e. A parameter that casts the cost function as continuous (smooth) or discontinuous (step-function-like) around the target cost value.

Popular cost functions include the Mean Square Error (MSE), Root Relative Square Error (RRSE), Average Relative Error (ARE) and Maximum Relative Error (MRE) [48]. In this thesis the cost function in (4.4.2) [55] is used. The parameter C changes the steepness of the gradient around the targeted threshold value as shown in Fig. 4.8, effectively asserting how stringent the requirement on the optimisation goal is.

$$\boldsymbol{g(\rho)} = -\frac{1}{2} + \frac{1}{\pi}\arctan\left[C\left(|\boldsymbol{\rho}| - |\rho_{ref}|\right)\right] \tag{4.4.2}$$

The expression in (4.4.2) represents a minimisation cost function where ρ_{ref} is the targeted threshold value of the optimised response and $\boldsymbol{\rho}$ is a vector of the simulated responses. For a maximisation case, (4.4.2) is written as

$$\boldsymbol{g(\rho)} = \frac{1}{2} - \frac{1}{\pi}\arctan\left[C\left(|\rho_{ref}| - |\boldsymbol{\rho}|\right)\right] \tag{4.4.3}$$

where (4.4.3) is still a minimisation problem, but the optimised response is maximised for a certain target. The mean of $\boldsymbol{g(\rho)}$ is then taken as the overall cost for all points in the vector $\boldsymbol{\rho}$. Experiments showed that the optimisation converged faster and yielded a better result, when the cost value of an iteration is defined as the mean of $\boldsymbol{g(\rho)}$, compared to the *minimax* cost function approach, as shown in Fig. 4.9 where only 49 simulation runs are required to find the optimum with the cost function in (4.4.2) compared to 80 runs with a minimax type of cost function. The expressions in (4.4.2) and (4.4.3) are also advantageous when it comes to weighted sums multi-objective optimisation since no

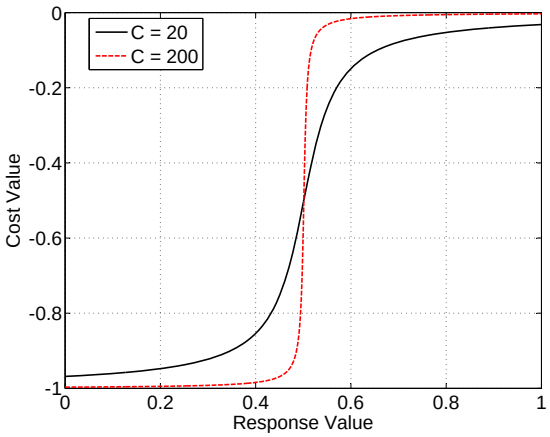

Figure 4.8: Examples of cost function variation around the target for cases where $C = 20$ and $C = 200$.

further rescaling is required as all goals are automatically scaled between $(-1, 0)$. The weights can thus be chosen in a more intuitive manner.

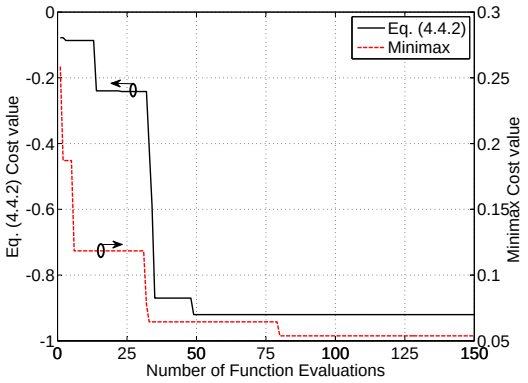

(a) Cost function convergence.

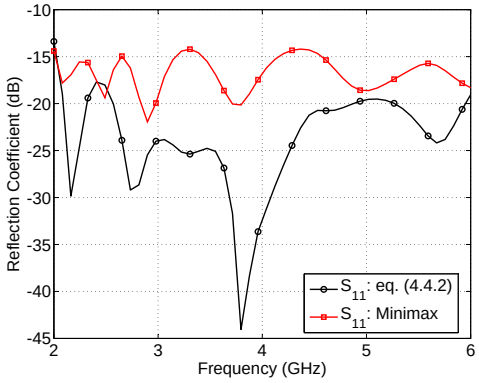

(b) Optimal responses.

Figure 4.9: Comparison between minimax cost function and the function in eq. (4.4.2) for the optimisation of a conical sinuous antenna for return loss (More details are provided in chapter 5).

4.4.3 Numerical Example #1

To demonstrate the effectiveness of the surrogate modelling and optimisation approach described in previous sections, expected improvement is applied to sample and optimise Ackley's function with two input parameters. Ackley's function is given by

$$F(x) = -20\exp\left\{-0.2\sqrt{\frac{1}{d}\sum_{i=1}^{d}x_i^2}\right\} - \exp\left\{\frac{1}{d}\sum_{i=1}^{d}\cos(2\pi x_i)\right\} + 20 + \exp\{1\} \qquad (4.4.4)$$

where d is the problem's dimension (2 in this case). Ackley's function was particularly chosen because it has many local minima, as shown in Fig. 4.10a, and it is one of the standard benchmark functions for many optimisation algorithms.

The number of initial unbiased samples for this experiment is given by (4.4.1) as 21. A Latin hypercube sampling algorithm is used to generate the initial samples and Kriging in conjunction with expected improvement are used to select subsequent points in an

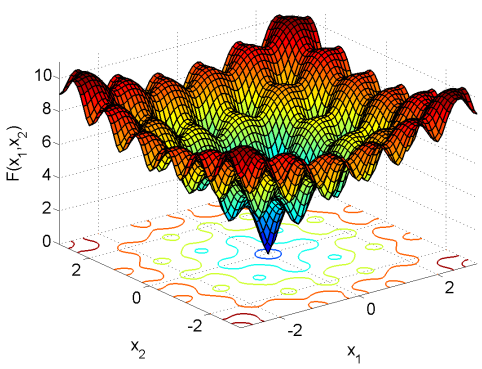

(a) Analytical Ackley's function.

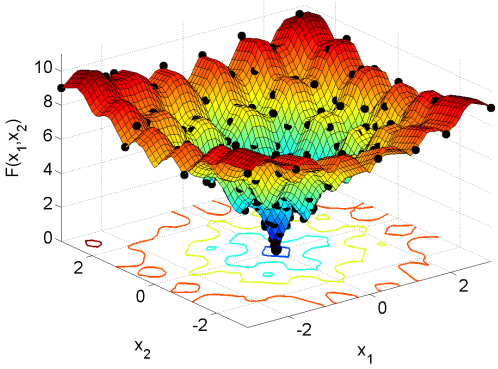

(b) Kriging model of Ackley's function.

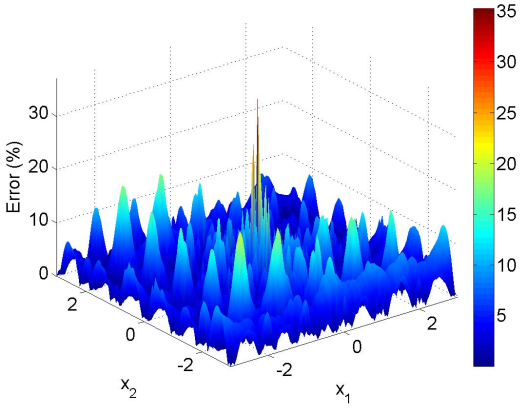

(c) Error between the analytical Ackley's function and its Kriging model.

Figure 4.10: Analytical and reconstructed Ackley functions and the error between the two. The function in (b) is reconstructed using a Kriging model with an exponential correlation function using 200 samples (black dots) selected with EI as the infill criterion.

iterative manner as shown by the flowchart in Fig. 4.4, with the maximum number of function evaluations being set to 200. The Kriging model's hyper-parameters (θ) as well as the EI criterion in (4.3.6) are optimised using a genetic algorithm with a population of 60 over 100 generations.

The built Kriging model, after 200 evaluations, is shown in Fig. 4.10b, and the error between the analytical function and its Kriging model is shown in Fig. 4.10c, where the error is mostly below 10% across the entire sample space, with a mean and median errors of 3.03% and 2.12% respectively; and a maximum error of 35.18%. The maximum error between the Kriging model and the analytical function can, of course, be reduced by increasing the number of samples, at an increased computational cost.

Table 4.1: Comparison of the minima of Ackley's function and its Kriging model.

Function	Minimum point	Minimum value
Analytical	$(0.00000, 0.00000)$	0.00000
Kriging model	$(0.00078, -0.00190)$	0.00592

The minimum of the analytical function and its Kriging model are shown in Table 4.1, where the obtained Kriging model values are within 0.59% of the analytical values.

The ability to accurately model a given function across the input parameter space with low errors as shown in Fig. 4.10c, as well as to simultaneously locate the minimum of a given function with accuracy levels as shown in Table 4.1, prove that surrogate based optimisation coupled with expected improvement (SBO-EI) can indeed be used to solve complex mixed integer optimisation as well as design space exploration and sensitivity analysis problems in a single optimisation run[3].

The next example demonstrates that SBO-EI of an antenna, performs better than a direct optimisation of the EM model. Therein, the direct optimisation is performed with the fast converging Particle Swarm Optimisation (PSO) algorithm while a genetic algorithm, with a population of 60 over 100 generations, is used in SBO-EI.

4.4.4 Numerical Example #2

The effectiveness of the EI approach and the outlined optimisation strategy on an actual EM structure, a conical sinuous antenna, described more thoroughly in the next chapter, is demonstrated by optimising the antenna for return loss. Further, the design space exploration capability of SBO-EI is also demonstrated in this example. A genetic algorithm, with a population of 60 over 100 generations, is used for hyper-parameter optimisation of the kriging model (see eq. (4.2.25)) as well as to optimise the EI criterion (see eq. (4.3.4)). The details of the optimisation problem are listed in Table 4.2. The parameter C in the cost function's expression in (4.4.2) is set to 200.

Table 4.2: Optimisation Problem Details

Parameter	Description
Number of variables	4
Optimisation type	Single objective
Return loss goal	$\geqslant 15$ dB
Frequency range	$2 - 6$ GHz

The number of unbiased simulations required for this problem is given by (4.4.1) as 43. However, an investigation into a relaxation of the minimum number of required unbiased simulations revealed that 31 simulations were sufficient for a conical antenna optimisation problem with 4 variables. Therefore, for this example and the ones discussed in chapter 5, the number of unbiased simulations was kept at 31. SBO-EI was applied to the preliminary kriging model built with 31 unbiased simulations. The goal of the optimisation was achieved with just 65 simulation runs (with the initial unbiased simulations included) as shown in Fig. 4.11a.

A comparison of the cost functions as well as the simulated optimal return loss obtained with the EI optimisation approach with that obtained with a direct optimisation of the antenna using Particle Swarm Optimisation (PSO), as implemented in FEKO, is shown in Fig. 4.11. PSO was chosen over the genetic algorithm in FEKO, as PSO has been shown

[3]Of course it is understood here that a single optimisation run consists of a limited number expensive function evaluations.

to achieve faster convergence rates (i.e. requiring fewer function evaluations) whilst having the same level of accuracy as a genetic algorithm [56].

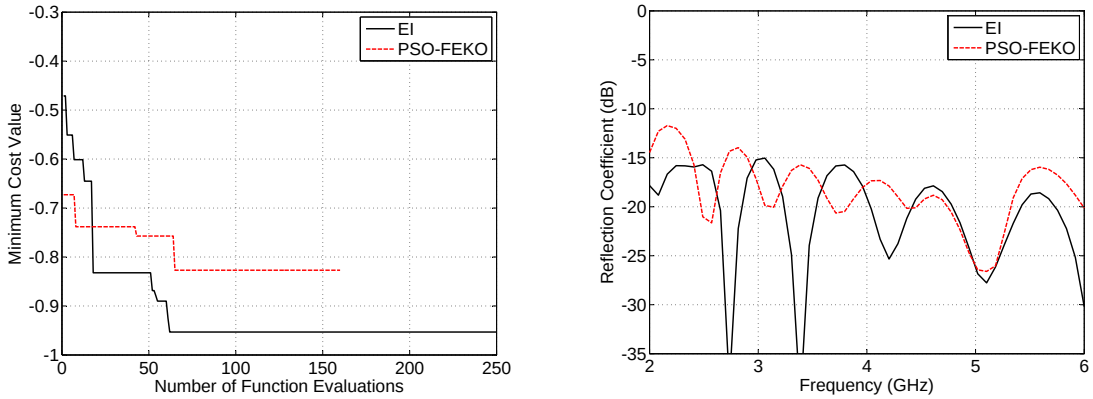

(a) Cost function variation. (b) Optimum return loss.

Figure 4.11: Cost function variation and optimal return loss results for the SBO with EI and direct optimisation on the EM model in FEKO using PSO. The FEKO optimisation was stopped after 160 iterations due to time constraints. Still a better minimum was found with EI long before stopping the direct optimisation in FEKO.

Clearly, a better optimum is obtained within fewer function evaluations with the surrogate modelling approach compared to direct optimisation of the EM model in FEKO, thus justifying the effectiveness of performing optimisation tasks on a surrogate model and only using the EM model to validate results from surrogate based optimisation.

A secondary advantage of SBO with EI is that design space exploration is carried out in tandem with optimisation as shown in Fig. 4.12 for the antenna's rotation angle, δ, where its evolution throughout the optimisation as well as a complete coverage of the whole design space can be clearly seen.

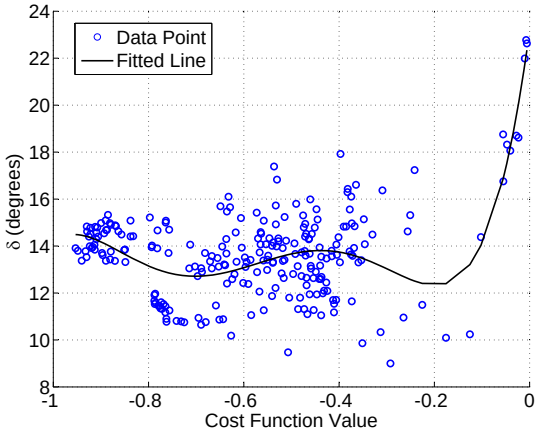

Figure 4.12: Example of the capability to carry out design space exploration on δ with SB with EI.

4.5 Conclusion

This chapter presented a surrogate modelling and optimisation technique that can be used to optimise computationally expensive functions, such as finely meshed EM struc-

tures. Kriging meta-modelling was introduced and was shown to be suitable to be used in conjunction with expected improvement for efficient optimisation as well as design space exploration tasks as shown in Fig. 4.12. The outlined optimisation strategy is used to optimise a conical sinuous antenna for various goals. This is discussed in detail in the next chapter.

Chapter 5

Optimisation of a Conical Sinuous Antenna

The planar sinuous antenna, discussed in chapter 3, was demonstrated to be band limited, with a maximum bandwidth ratio of about 3 : 1 when designed without absorber backing. The planar antenna's wideband performance is limited by the distance between the antenna and the reflecting ground plane.

A configuration that circumvents this problem is the inverted conical sinuous antenna over a reflecting ground plane [9], hereafter referred to as the conical antenna, where the high frequency radiating elements are closest to the ground plane while the low frequency elements are farther away from the ground plane. This configuration is virtually not bandwidth limited as it does not suffer from phase cancellation issues that the planar antenna in chapter 3 suffers from. A return loss of 9 dB or better was achieved for the conical antenna in [9], by studying the effects of the angular width and rotation angle on the return loss performance of the antenna.

In this chapter, the optimisation routine presented in chapter 4 is used to optimise the conical antenna for various performance goals, including return loss, aperture efficiency for a prime focus paraboloid, relative cross-polarisation as well as a combination of all three mentioned goals. Also, the relationship between the main parameters and their effects on the conical antenna's response is derived from the optimisation results. The conical antenna's geometry and its optimisation is presented in the subsequent sections.

5.1 Conical Sinuous Antenna

The Conical antenna is obtained by projecting the planar sinuous antenna onto a truncated right circular cone. The antenna was first introduced in the original sinuous antenna patent [12] where the taper on the cone was used to increase the sinuous antenna's front-to-back ratio and thus achieving unidirectional radiation. The most recent investigation [9] does not rely on the improved front-to-back ratio that a cone with a small aperture provides, but it uses a reflecting ground plane to achieve unidirectional radiation. The conical antenna in [9] offers advantages such as a stable phase centre and the potential for easy integration with active components such as LNAs, as these and the simple (compared

to the feed in section 3.3.1) feed network are conveniently located behind the reflecting ground plane where there is ample space.

The antenna is shown in Fig. 5.1 and its design parameters are described in Table 5.1. The cone's aperture half-angle is given by θ and varies from about $20° - 85°$.

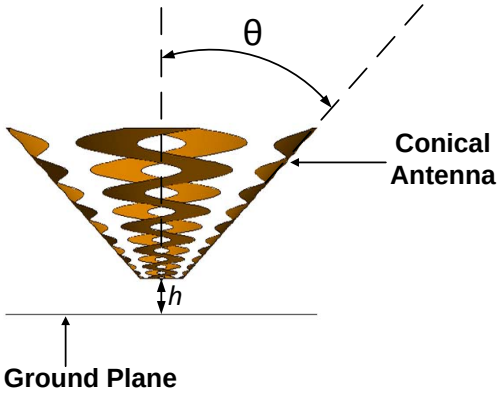

Figure 5.1: Inverted conical sinuous antenna over a reflecting ground plane.

Table 5.1: Conical Sinuous Antenna Design Parameters.

Parameter	Description
θ	Cone's aperture half-angle
α	Angular width
δ	Rotation angle
τ	Growth rate
h	Distance from the ground plane

To effectively and efficiently optimise any system, the number of significant variables has to be reduced as much as possible. This is necessary in order to speed up the optimisation process, by narrowing the search space, as well as to reduce the number of required training samples as given by (4.4.1). Of the 5 parameters in Table 5.1, all are optimised except for h. Then the effect of varying h, on the optimised response, is demonstrated afterwards. The distance, h, from the ground plane to the apex of the cone is maintained at 5 mm for all optimisation problems described in subsequent sections, after a brief parametric study. Also, as was demonstrated in section 3.3.3 for the planar antenna, the size of the ground plane should be kept as small as possible so as not to deteriorate the antenna's BOR_1 efficiency. Therefore, the circumference of the ground plane is made equal to that of the conical sinuous antenna, as viewed from the top, throughout this chapter. The implication of this choice being that side lobe levels at the low frequency end will be slightly higher. A finite ground plane is required in our optimisation runs as the use of an infinite ground plane yields low BOR_1 efficiency values.

The study in [9] only involved investigating the effects of varying the level of interleaving (α and δ) and the growth rate (τ) on the conical antenna's return loss. In the subsequent sections the cone's aperture half-angle, θ, is included in the optimisation and

is shown to be an important parameter in determining the overall performance of the antenna.

5.2 Single Objective Optimisation

In this section, the optimisation method and strategy described in chapter 4, is used to optimise the conical antenna for return loss, aperture efficiency for a prime-focus paraboloid reflector as well as cross-polarisation. Also, the use of EI for design space exploration will be demonstrated. The variables in the optimisation cases discussed in subsequent sections are all constrained between an upper and lower bound as listed in Table 5.2.

Table 5.2: Constraints on optimisation parameters.

Parameter	Min.	Max.
θ	45.0°	75.0°
α	21°	35.0°
δ	9.00°	23.0°
τ	0.80	0.86

5.2.1 Aperture Efficiency Optimisation

The conical sinuous antenna is optimised for maximum ideal aperture efficiency when used to illuminate a prime-focus paraboloid reflector with a subtended half-angle equal to 55°. The optimisation problem is summarised in Table 5.3.

Table 5.3: Aperture Efficiency Optimisation Problem Details

Parameter	Description
Number of variables	4
Optimisation type	Single objective
Efficiency goal	$\geqslant 65\%$
Frequency range	$2 - 6$ GHz

The results of the optimisation in Fig. 5.2a, show that the objective was achieved within 50 simulation runs. It must be noted that the optimisation was undertaken using a pre-built kriging model from the unbiased training samples, and therefore, the actual number of simulation runs to optimise the conical antenna for this section's goal is only 19 simulations. An optimal aperture efficiency of about 70% is obtained across the specified frequency band as shown in Fig. 5.2b and the optimised values yielding the response in Fig. 5.2b are listed in Table 5.4.

As mentioned in section 4.3, both exploration and exploitation are achieved with expected improvement and tasks such as design space exploration and sensitivity analysis can be accomplished using optimisation results of a given cost function.

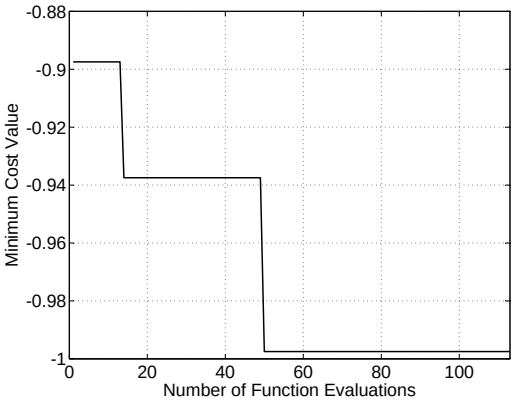

(a) Cost function variation.

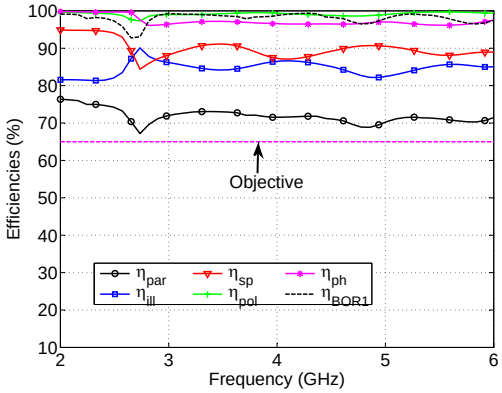

(b) Optimal efficiency for $\theta_e = 55°$.

Figure 5.2: Aperture efficiency optimisation.

Table 5.4: Optimised values for maximum aperture efficiency.

Parameter	Value
θ	68.99°
τ	0.847
δ	17.09°
α	30.79°

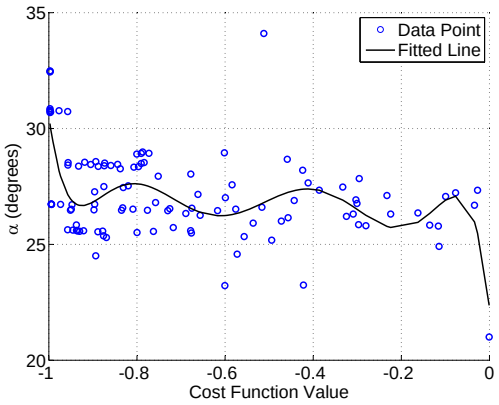

(a) Effect of α variation.

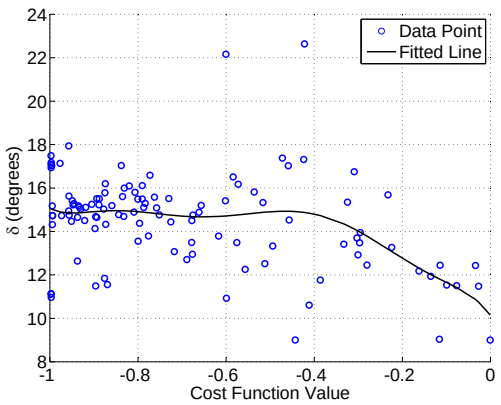

(b) Effect of δ variation.

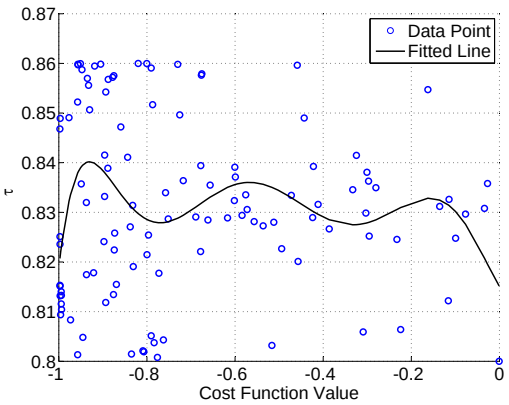

(c) Effect of τ variation.

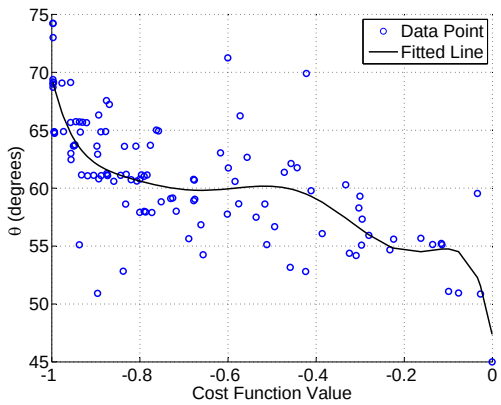

(d) Effect of θ variation.

Figure 5.3: Design space exploration for a design with the goal of maximising aperture efficiency.

In Fig. 5.3, plots of the distribution of the variable values against the cost function are shown. The fitted trend lines, which are 7^{th} order polynomial approximations of the data collected during optimisation, show that the values of α and τ have less impact on the overall efficiency performance of the conical antenna as they oscillate around a constant value for different cost values, except near the minimum, as can be seen in Fig. 5.3a and 5.3c respectively. The trend line in Fig. 5.3b shows that the cost value is only sensitive to values of δ less than about 15°, where a linear increase in cost value is observed with decreasing δ values. The cost function's variation is most affected by the value of the cone's aperture half-angle, θ, with cost values decreasing as θ increases as shown by the trend line in Fig. 5.3d, suggesting that a large aperture half-angle is crucial to the antenna's aperture efficiency performance. This observation is validated for different subtended angles in the multi-objective optimisation cases in section 5.4.

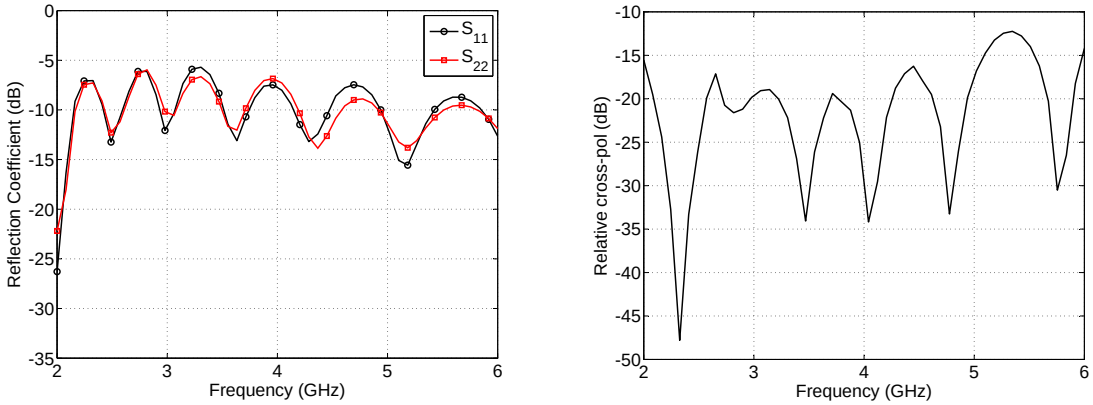

(a) Return loss. (b) Relative cross-polarisation.

Figure 5.4: Corresponding return loss and relative cross-polarisation responses for the conical antenna optimised for aperture efficiency.

Return loss and relative cross-polarisation performances of the optimised antenna in this section, are shown in Fig. 5.4, where it can clearly be seen that a conical antenna optimised for aperture efficiency yields a unacceptably large return loss (nearly 5 dB) levels while relative cross-polarisation levels are mostly below −15 dB across the band with a peak value of −12.7 dB.

5.2.2 Relative Cross-polarisation Optimisation

The next figure of merit to be optimised is the absolute relative cross-polarisation within the HPBW, in the $\phi = 45°$ plane. Ludwig's third definition [25] is used in calculating cross-polarisation and the variables θ, α, δ and τ are also optimised with SBO-EI as described in chapter 4. The optimisation problem is described in Table 5.5.

The results of the optimisation are shown in Fig. 5.5, where a maximum relative cross-polarisation of −18.12 dB is obtained across the band after 194 simulation runs as shown in Fig. 5.5a. The optimised cross-polarisation results do not satisfy the goal of −23 dB stated in Table 5.5, within the allocated computational budget of 220 full-wave EM simulations. It can therefore be concluded that a maximum in band cross-polarisation of −23 dB can not be achieved with the optimisation set-up in Table 5.5 and the cost

Table 5.5: Relative Cross-polarisation Optimisation Problem Details

Parameter	Description
Number of variables	4
Optimisation type	Single objective
Cross-polarisation goal	$\leqslant -23$ dB
Frequency range	$2-6$ GHz

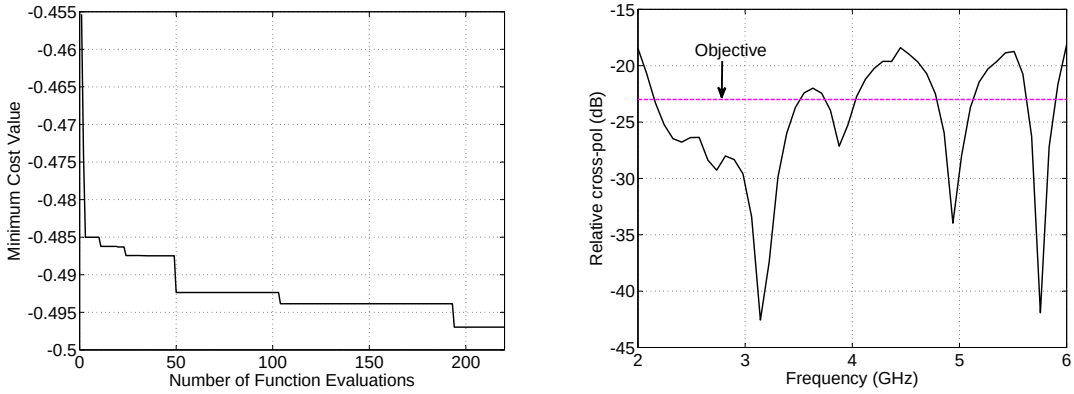

(a) Cost function variation. (b) Optimal relative cross-polarisation.

Figure 5.5: Relative cross-polarisation optimisation in the $\phi = 45°$ plane.

function in (4.4.2). Such a level of cross-polarisation could possibly be achieved by using a superior and more efficient optimisation technique or increasing the number of variables in the optimisation process, which would result in a significant increase in computation cost. The optimised radiation patterns at selected frequencies are shown in Fig. 5.6, where it can clearly be seen that the maximum cross-polarisation within the HPBW ($\approx 28.1°$.) corresponds to the one shown on Fig. 5.5b.

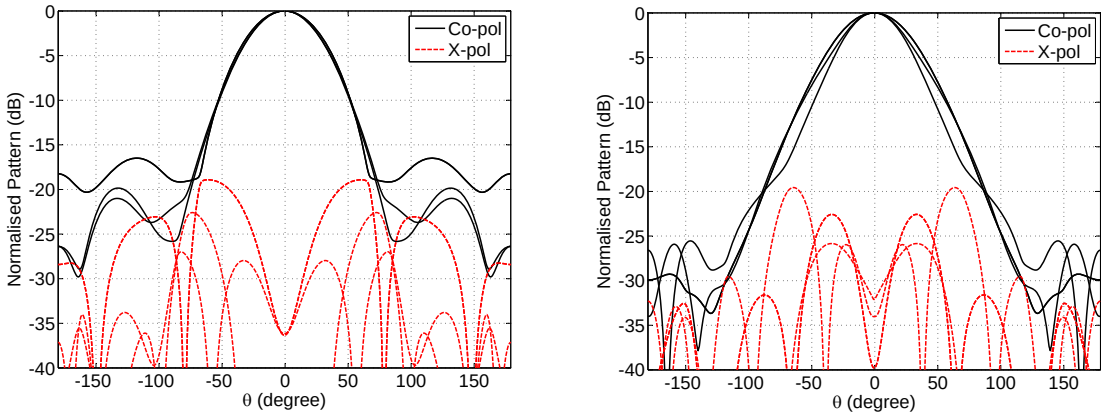

(a) $f \in \{2.16, 2.90, 3.14\}$ GHz. (b) $f \in \{4.04, 4.86, 5.67\}$ GHz.

Figure 5.6: Optimised co- and cross-polar patterns at selected frequencies in the $\phi = 45°$ plane.

In the same manner as in section 5.2.1, the optimisation results in this section are used for parametric study purposes. The distribution of the values of each of the four design variables during optimisation is shown in Fig. 5.7. The optimal values are listed in Table 5.6.

Table 5.6: Optimised values for minimum relative cross-polarisation.

Parameter	Value
θ	56.40°
τ	0.821
δ	14.33°
α	27.24°

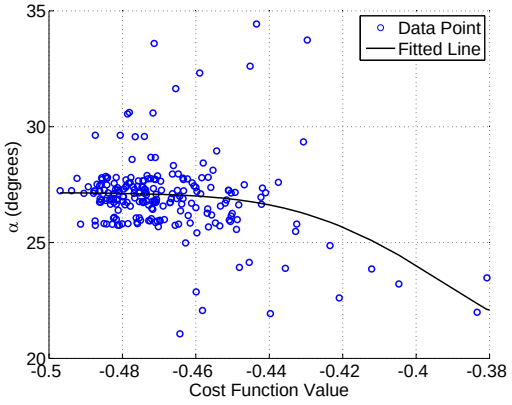

(a) Effect of α variation.

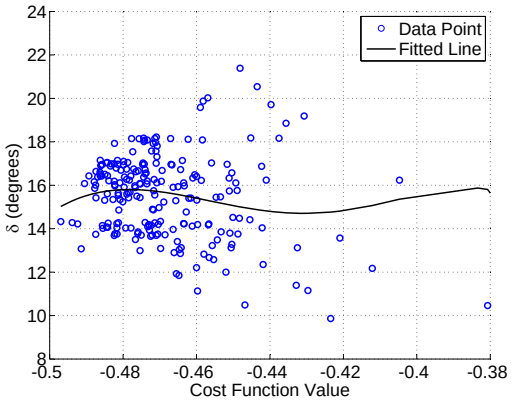

(b) Effect of δ variation.

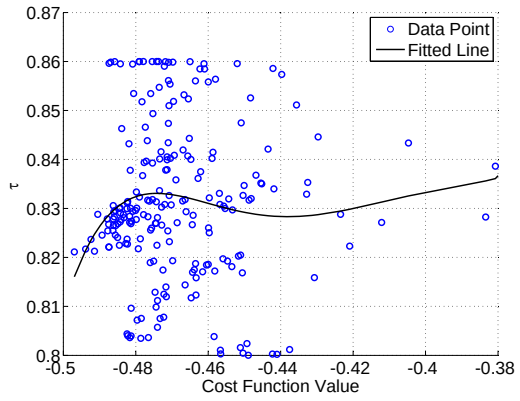

(c) Effect of τ variation.

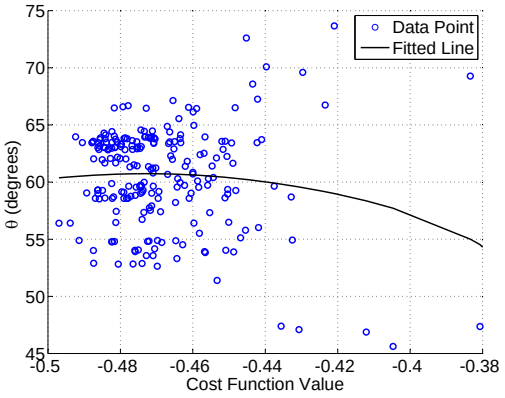

(d) Effect of θ variation.

Figure 5.7: Design space exploration for a design with the goal of minimising relative cross-polarisation.

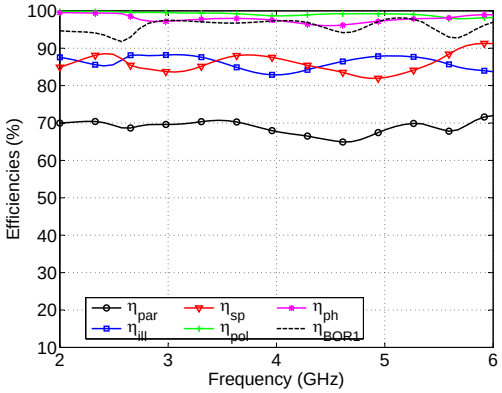

(a) Aperture efficiency.

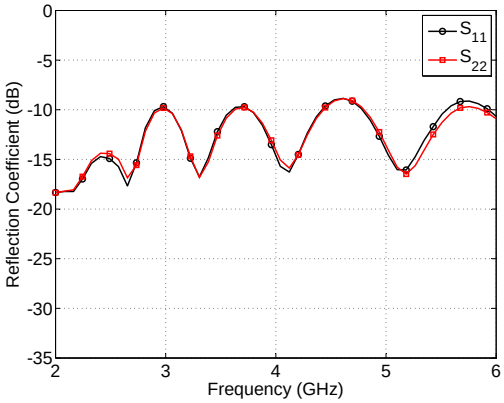

(b) Return loss.

Figure 5.8: Corresponding return loss and aperture efficiency responses for the conical antenna optimised for cross-polarisation.

It can be seen from Fig. 5.7 that the cost function is affected by values of $\alpha \leqslant 26°$ and $\tau \leqslant 0.83$, with θ and δ having negligible influence on the cost values as illustrated by the 5^{th} order polynomial fitting lines in Fig. 5.7b and 5.7d. Also, by observing the rapid variation of the fitting line near the minimum cost value, it can be concluded from the plots in Fig. 5.7 that, τ is the most significant variable in the vicinity of the optimum while α is dominant elsewhere in the design space, as is demonstrated in section 5.3.

The corresponding return loss and aperture efficiency responses for the optimised antenna in this section are shown in Fig. 5.8, where an acceptable aperture efficiency of 64% or better is obtained across the entire bandwidth. The high aperture efficiency obtained here is justified by the large values of the conical antenna's aperture angle, θ, at the optimum as shown in the design space exploration plots in Fig. 5.7d and Fig. 5.3d, for the optimisation goals of minimum relative cross-polarisation and maximum aperture efficiency respectively. A relatively good[1] return loss is obtained across the band with minimum values of 8.5 dB. A usable antenna is thus obtained by optimising for relative cross-polarisation alone.

5.2.3 Return Loss Optimisation

The last of the single objective optimisations involves return loss for a differential impedance of 300 Ω at the input port. The optimisation problem is given in Table 5.7. As in previous sections, 4 of the parameters in Table 5.1 are included in the optimisation and the stored 31 simulation samples are used for model training as described in section 4.4.1. The maximum number of simulations is set to 220.

Table 5.7: Return Loss Optimisation Problem Details

Parameter	Description
Number of variables	4
Optimisation type	Single objective
Return loss goal	$\geqslant$ 18 dB
Frequency range	2 – 6 GHz

Only 59 simulations (including the training samples) are required to reach the optimum results as shown in Fig. 5.9a. It can be seen in Fig. 5.9b that the objective stated in table 5.7 was not achieved across the entire frequency range, especially at frequencies below 2.14 GHz where the optimal design is to a large extent affected by end reflection effects. As stated before, the results in Fig. 5.9 were obtained for an input impedance of 300 Ω which was selected after a parameter study. However it is not certain that 300 Ω is the optimal input impedance and therefore the optimisation results in this section could greatly benefit from the inclusion of the input impedance as a variable to be optimised. It follows that such an endeavour would result in increased computational cost due to the increase in the size of the search space.

As was done for the cases in the previous two sections, the optimisation results in this section are used for parametric studies. The distribution of the values of each of the four

[1] A good return loss is defined as 10 dB or greater in this document.

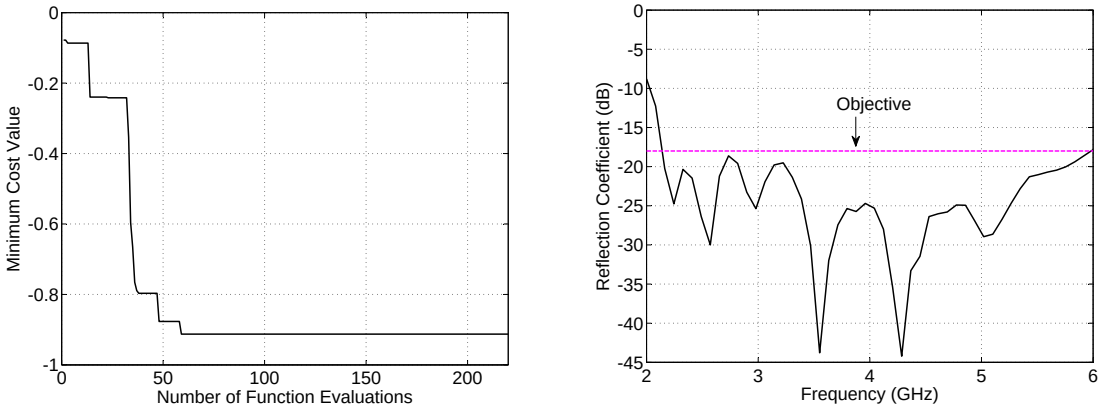

(a) Cost function variation.

(b) Optimal return loss.

Figure 5.9: Return loss optimisation results.

design variables during optimisation is shown in Fig. 5.10. The optimal values are listed in Table 5.8.

Table 5.8: Optimised values for the return loss objective in Table 5.7.

Parameter	Value
θ	48.89°
τ	0.860
δ	13.79°
α	21.01°

Also shown in Fig. 5.10 are line plots of 9^{th} order polynomial fitting functions for each of the four optimisation variables. Unlike in the previous two cases, there is more than one dominant variable in the optimisation case in this section. Indeed, the trend lines in Fig. 5.10 show that the values of α, δ and θ decrease with decreasing cost function values. An initial rapid decrease in the values of δ and θ, to values around 13° and less than 50° respectively, is observed, while α gradually decreases towards its optimum value. Given the variation of the trend lines in Figs. 5.10a, 5.10b and 5.10d, a rigorous global quantitative sensitivity analysis[2] is required to determine the most significant design variable.

It is however clear that all 3 variables are necessary for this optimisation unlike in sections 5.2.1 and 5.2.2 where the optimal results could be found with fewer variables.

Aperture efficiency as well as relative cross-polarisation results of the optimal antenna are shown in Fig. 5.11, where a very poor aperture efficiency is obtained, with efficiencies as poor as 38% being obtained within the optimised band, while the minimum cross-polarisation discrimination is about 11.6 dB.

[2]Global sensitivity analysis is beyond the scope of this work. It can however be carried out on a Kriging model of the data collected during the optimisation process, using Monte Carlo simulations.

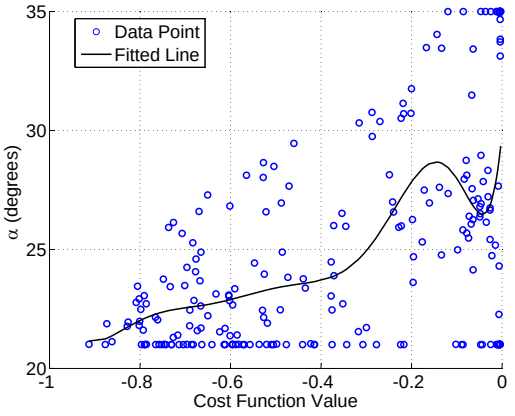

(a) Effect of α variation.

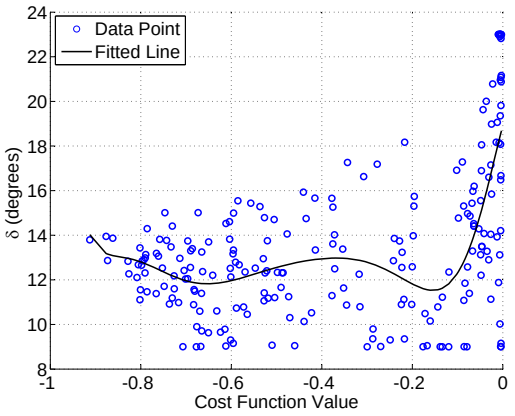

(b) Effect of δ variation.

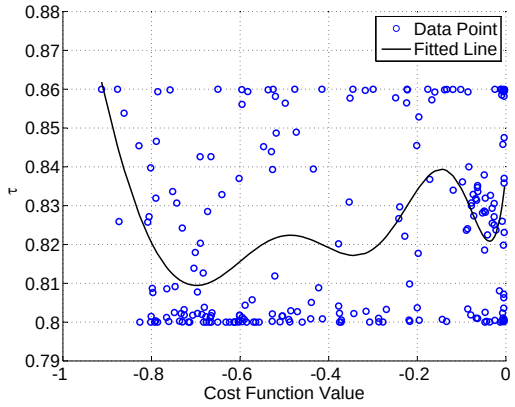

(c) Effect of τ variation.

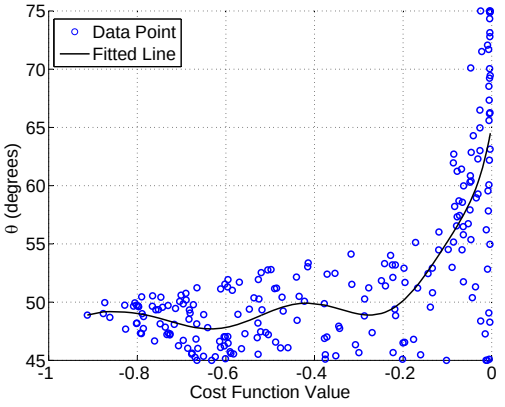

(d) Effect of θ variation.

Figure 5.10: Design space exploration for a design in Table 5.7.

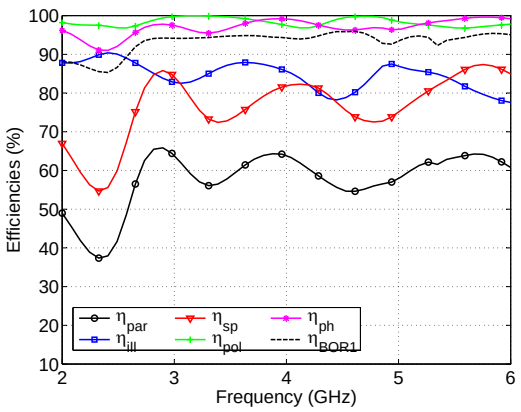

(a) Aperture efficiency.

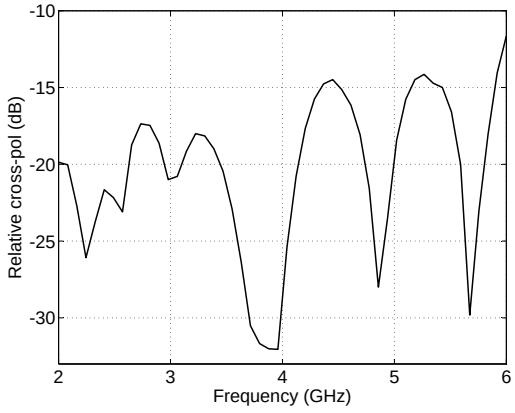

(b) Relative cross-polarisation.

Figure 5.11: Corresponding aperture efficiency and relative cross-polarisation responses for the conical antenna optimised for aperture efficiency.

5.3 Local Sensitivity Analysis

As mentioned in chapter 4, results obtained with SBO-EI can be used for design space exploration (see section 5.2) and sensitivity analysis, which is the focus of this section.

The goal of sensitivity analysis is to determine the extent to which a change in a variable affects the system's response. Local sensitivity analysis (LSA) involves the evaluation of the response's partial derivative when one input variable is perturbed by a small value

p, while the others are kept constant as

$$S_v = \frac{\partial f}{\partial x} = f'(x) \tag{5.3.1}$$

and the partial derivative $f'(x)$ is evaluated using the central difference formula as

$$f'(x) = \frac{f(x+p) - f(x-p)}{2p}. \tag{5.3.2}$$

To ensure uniformity of results, all four variables, used in the optimisations of section 5.2, are perturbed by $p = 0.1$. This requires all variable values within the range listed in Table 5.2 to be mapped to a standard domain for the amount of perturbation to be the same for all variables. The Kriging model is then evaluated at the perturbed values and the gradient in (5.3.2) is then calculated. The algorithm used is illustrated in Fig. 5.12a and the resulting sensitivities are shown in Fig. 5.12b.

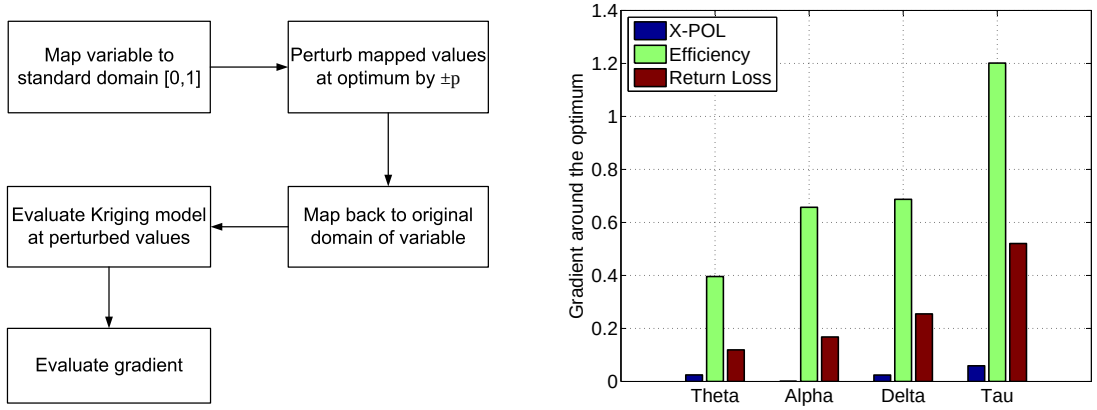

(a) Sensitivity analysis algorithm.

(b) Sensitivities for different cases.

Figure 5.12: Sensitivity analysis algorithm and resulting local sensitivity values around the optima of the return loss, aperture efficiency and relative cross-polarisation responses, perturbed by $p = \pm 0.1$.

It can be seen in Fig. 5.12 that cross-polarisation results are barely affected by changes in α. Also, the variables whose change around the optimum greatly impact the antenna's response are, in increasing order, θ, α, δ and τ as can be readily seen in Fig. 5.12b. It must be noted that the gradient values for different cases (return loss, X-pol, efficiency) in Fig. 5.12b should not be compared against each other. i.e. it would be incorrect to deduce, from Fig. 5.12b, that the antenna's aperture efficiency response is more susceptible to changes in τ than its return loss response as the two are fundamentally different.

5.4 Towards Multi-Objective Optimisation

A good feed for a reflector antenna must have a number of characteristics including high cross-polarisation discrimination (XPD), aperture efficiency, return loss and low system temperature for noise critical applications like the meerKAT and SKA radio telescopes [5, 4].

Antenna design, like many other real world problems, involves the application of acceptable trade-offs among several conflicting design objectives. To put this in perspective,

let us consider aperture efficiency and return loss optimisation results from section 5.2. It is apparent in Fig. 5.3 and 5.10 that the two optimisation goals are indeed conflicting, with values that lead to a minimum solution for one goal, maximising the other goal as shown for the angular width, α in Fig. 5.3a and 5.10a, and the cone's aperture half-angle, θ in Fig. 5.3d and 5.10d, respectively. Therefore, the goal of the optimisation is to find a set of equivalent solutions to all goals. This set is often referred to as the Pareto front [57, 58], from which the best solution is selected.

5.4.1 Surrogate Based Multi-Objective Optimisation

The efficiency of SBO was demonstrated for single objectives in chapter 4 and section 5.2, where it was coupled with expected improvement (SBO-EI) and was shown to be better than a direct optimisation of the EM model. For a multi-objective problem, three different approaches can be taken:

1. Building a globally accurate surrogate model for each of the optimisation goals (SBO-EI is applicable here) and using a constrained multi-objective global optimisation algorithm to find the Pareto front and selecting the best solution from the Pareto set by applying some constraints [58].

2. Building an optimised multi-objective surrogate model. This approach is not trivial and only recently, the expected improvement sampling criterion was effectively extended to a multi-objective SBO [57]. Although this approach might be the most efficient, the statistics involved is very complex and thus could not be implemented for this project.

3. The most commonly used method for multi-objective optimisation consists of aggregating different cost functions as weighted sums into one cost function, given in (5.4.1) where f_i is the cost of the i^{th} function and α_i its associated weight, and an optimised surrogate model of the aggregate cost function can thus be built using the technique described in chapter 4. The implication of this method being that the obtained optimal result is strongly dependent on the selected values for the weighting factors α_i.

$$f_c = \sum_{i=1}^{N} \alpha_i f_i. \tag{5.4.1}$$

The simplicity of method 3, listed above, justifies its use for all multi-objective optimisation cases considered hereafter in this chapter. In what follows combined return loss and aperture efficiency optimisations are presented as well as one with cross-polarisation included.

5.4.2 Optimisation Case I

Herein, the conical sinuous antenna is optimised for return loss and aperture efficiency. Both optimisation goals are equally important and therefore the weights $\alpha_i = 1 \ \forall i$ in (5.4.1) and the cost function values are given by (4.4.2) as described in section 4.4.2 and

the height, h, above the ground plane is kept at 5 mm . The details of the optimisation are listed in Table 5.9 and as in previous sections, the total number of full-wave evaluations is limited to 200, during optimisation.

Table 5.9: Return loss and aperture efficiency optimisation problem details

Parameter	Description
Number of variables	4
Optimisation type	Multi-objective
Return loss goal	$\geqslant 11.25$ dB
Efficiency goal	$\geqslant 64\%$
Frequency range	$2-6$ GHz

The aperture efficiency is optimised for different values of the subtended half-angle, namely for $\theta_e = 48°, 50°, 55°$ and $58°$ and the optimal results are shown in Fig. 5.13, where degradation in aperture efficiency is observed with increasing subtended half-angle, beyond $\theta_e = 50°$.

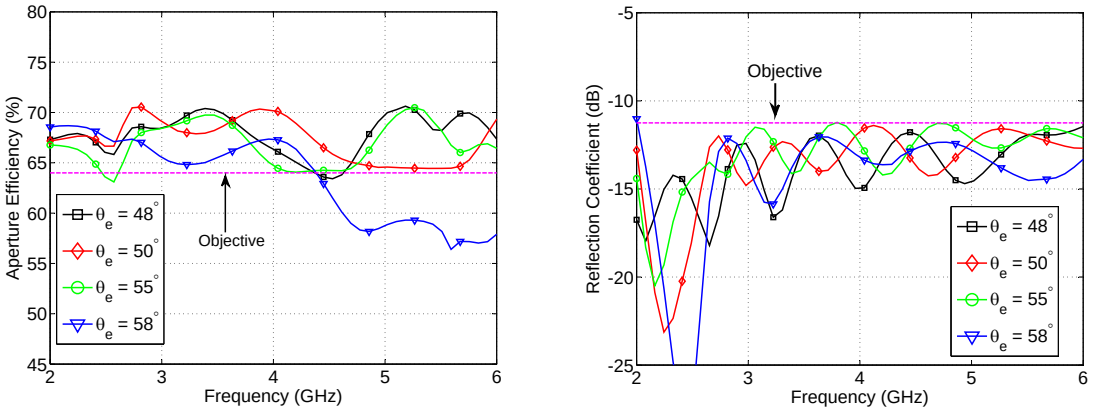

(a) (b)

Figure 5.13: Optimal aperture efficiency and return loss for different values of the subtended half-angle, θ_e.

The corresponding return loss responses are shown in Fig. 5.13b, where it can be seen that the objective is achieved across the design bandwidth for all different θ_e cases. Also, cost function variations for each of the four θ_e cases are shown in Fig. 5.14. It is clear from Fig. 5.14 that the conical sinuous antenna performs better as a feed for a paraboloid reflector with a subtended half-angle in the range of $[48°, 50°]$ as justified by the fast convergence of the cost function towards a better minimum. Indeed, the cost function plots in Fig. 5.14 show that the minimum cost value gets increasingly worse for values of $\theta_e > 50°$. Also evident in this optimisation, is the ease with which the antenna can be optimised for a given return loss than for aperture efficiency when the two goals are combined. Optimal parameters for all four cases are shown in Table 5.10, where the poor aperture efficiency performance for $\theta_e = 58°$ is further justified by the relatively small cone aperture angle θ which was shown in section 5.2 to favour return loss over aperture efficiency performance.

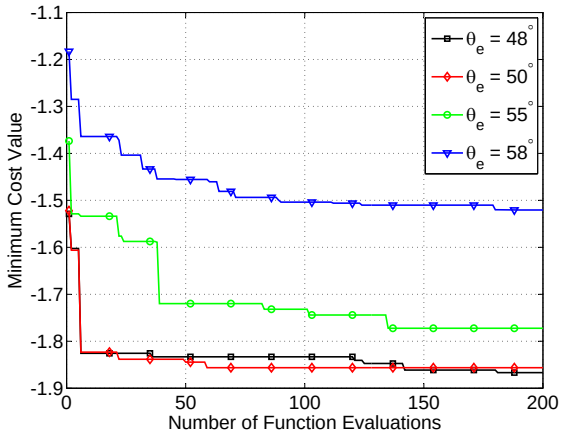

Figure 5.14: Cost function variation for different values of the subtended half-angle, θ_e.

Table 5.10: Optimal parameter values at different subtended angles (θ_e).

Parameter	$\theta_e = 48°$	$\theta_e = 50°$	$\theta_e = 55°$	$\theta_e = 58°$
α	24.91°	24.51°	24.89°	26.84°
δ	14.10°	15.12°	15.18°	15.39°
θ	56.58°	56.73°	56.82°	53.63°
τ	0.814	0.812	0.826	0.814

Shown in Fig. 5.15 are the optimisation variable versus cost function values for individual return loss and aperture efficiency optimisations as well as the optimum values of an equally weighted combined return loss and efficiency optimisation for a subtended half-angle of $\theta_e = 55°$. It is evident from Fig. 5.15 that the optimum values of the combined optimisation are indeed a compromise between the two distinct goals. The next section discusses a combined return loss, aperture efficiency and relative cross-polarisation optimisation.

5.4.3 Optimisation case II

This section focuses on the optimisation of the conical antenna for return loss, aperture efficiency as well as cross-polarisation. As in section 5.4.2, an equally weighted sum of all goals is used as the cost function to optimise. The problem details are summarised in Table 5.11.

Table 5.11: Return loss, relative cross-polarisation and aperture efficiency optimisation problem details.

Parameter	Description
Number of variables	4
Optimisation type	Multi-objective
Return loss goal	$\geqslant 11.25$ dB
Efficiency goal	$\geqslant 64\%$
Relative cross-pol goal	$\leqslant -18$ dB
Frequency range	$2 - 6$ GHz

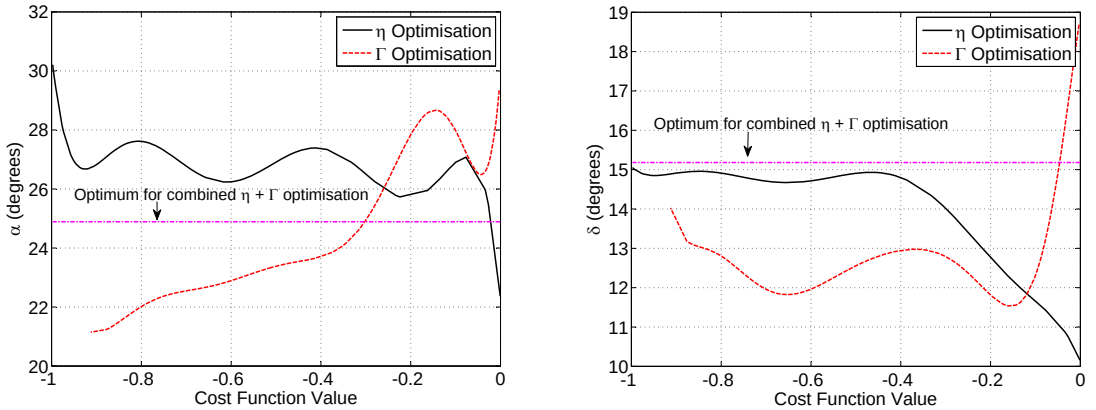

(a) Effect of α variation.

(b) Effect of δ variation.

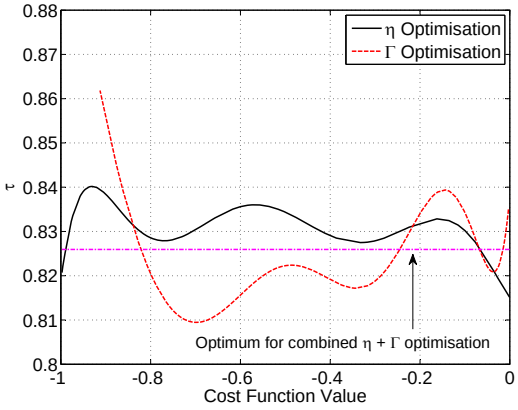

(c) Effect of τ variation.

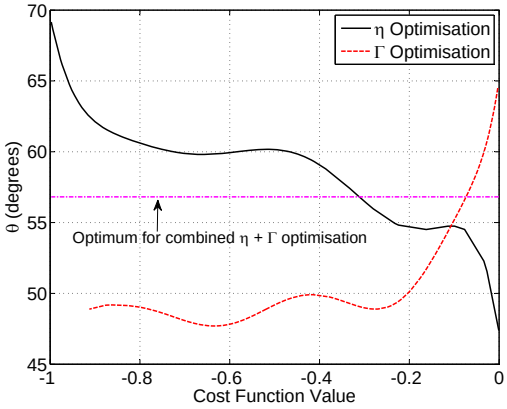

(d) Effect of θ variation.

Figure 5.15: Evolution of optimisation parameters versus cost function for return loss and aperture efficiency optimisation for $\theta_e = 55°$. Aperture efficiency optimisation results are denoted by η and return loss results by Γ.

The antenna is optimised for different subtended half-angles $\theta_e \in \{48°, 50°, 52°, 55°, 58°\}$ and the worst case results for each optimisation goal are shown in Fig. 5.16 as a function of the subtended half-angle.

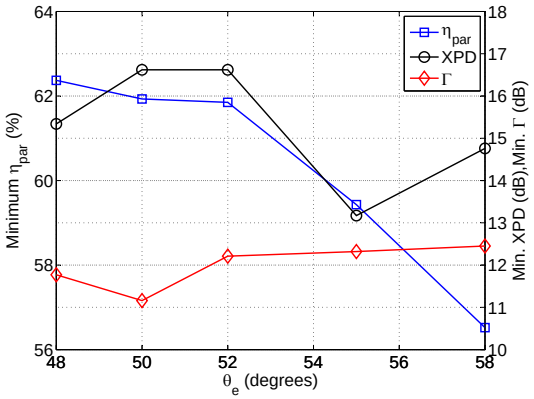

Figure 5.16: Worst case results for aperture efficiency (η_{par}), return loss (Γ) and cross-polarisation discrimination (XPD) for different subtended angles θ_e.

It can be easily seen in Fig. 5.16 that aperture efficiency deteriorates with increasing subtended angle, while return loss increases. This is due to the antagonistic relationship

between return loss and aperture efficiency with respect to the cone's aperture angle, θ and the antenna's angular width α, as discussed in section 5.4.2. XPD values are generally better for a subtended angle less than about 52°. The optimal results for each subtended angle are shown in Table 5.12.

Table 5.12: Optimal parameter values at different subtended angles (θ_e).

Parameter	$\theta_e = 48°$	$\theta_e = 50°$	$\theta_e = 52°$	$\theta_e = 55°$	$\theta_e = 58°$
α	27.26°	23.87°	25.40°	25.37°	26.27°
δ	13.58°	15.28°	15.38°	13.80°	13.41°
θ	54.48°	55.09°	53.94°	54.38°	53.56°
τ	0.828	0.825	0.825	0.818	0.817

All things considered, optimal results are obtained for $\theta_e \in [48°, 52°]$. However, we choose the results for $\theta_e = 48°$, because of its superior aperture efficiency, while results for both return loss and XPD are acceptable.

The optimal responses for $\theta_e = 48°$ are shown in Fig. 5.17 for the entire $2 - 6$ GHz bandwidth, where it is clearly seen that the return loss goal, in Table 5.11, is exceeded while aperture efficiency and cross-polarisation goals are not met across the entire bandwidth. This is due to the conflicting nature of the various optimisation goals.

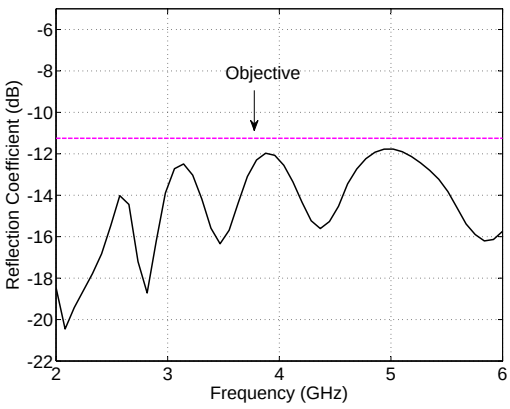

(a) Return loss.

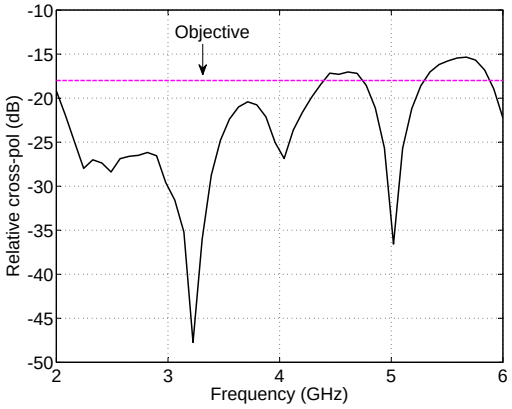

(b) Relative cross-polarisation.

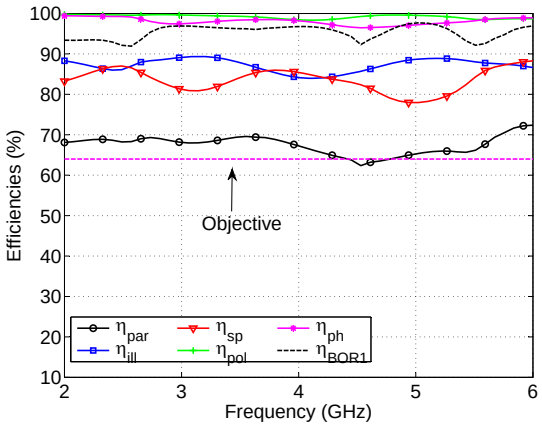

(c) Predicted efficiencies.

Figure 5.17: Optimal responses of the conical for a prime-focus paraboloid with a subtended angle $\theta_e = 48°$.

5.5 Effects of varying the distance from the ground plane

The optimisation cases presented thus far had the distance, h, between the conical antenna's apex and the reflecting ground plane maintained at 5 mm. In this section the effects of varying h are demonstrated by considering the optimal result of section 5.4.3 for different cases of $h \in \{3.5, 5, 6, 7, 8.5, 10\}$ mm. Fig. 5.18 shows that values of $h < 5$ mm result in poor return loss because of the close proximity of the antenna to the ground plane resulting in a sharp decline in input impedance. Furthermore, aperture efficiency decreases with increasing values of h, while return loss values are low for too small or too large distances from the reflecting ground plane, with a value around 5 mm being the optimal for h. XPD results also get progressively worse for values of $h > 5$ mm.

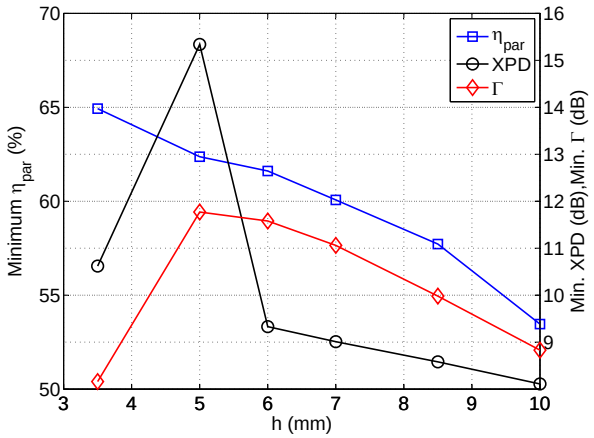

Figure 5.18: Worst case results for aperture efficiency (η_{par}), return loss (Γ) and cross-polarisation discrimination (XPD) for different values of h.

5.6 Construction and Measurements

The optimal model from section 5.4.3 is used as a starting point to build the antenna. Unlike in chapter 3 where the distance between the antenna and ground plane was larger than a quarter of a wavelength (12.5 mm) at the highest frequency, the distance here is much smaller than 12.5 mm, leading to relatively simpler feeding scheme illustrated in Fig. 5.19. Indeed, four pins with a diameter of 0.5 mm each, are used to feed the antenna. The pins used here are the inner conductors of standard semi-rigid coaxial lines and thus no special manufacturing is required. The model with pins included is then optimised for the

Table 5.13: Optimal parameters for the final conical antenna model to be built.

Parameter	Value
θ	56.48°
δ	14.95°
α	24.85°
τ	0.842

goals in Table 5.11 and the results are shown in Fig. 5.20, where a marked improvement

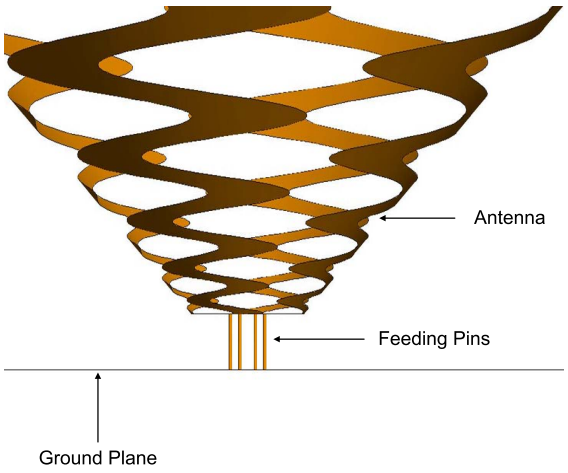

Figure 5.19: Feed detail of Conical antenna.

in both aperture efficiency and relative cross-polarisation can be seen, with a -20 dB cross-polarisation level for 87% of the optimised bandwidth. Indeed, addition of feeding pins results in a conical antenna that achieves two of the three optimisation goals in Table 5.11. The optimal parameters of the final model are shown in Table 5.13.

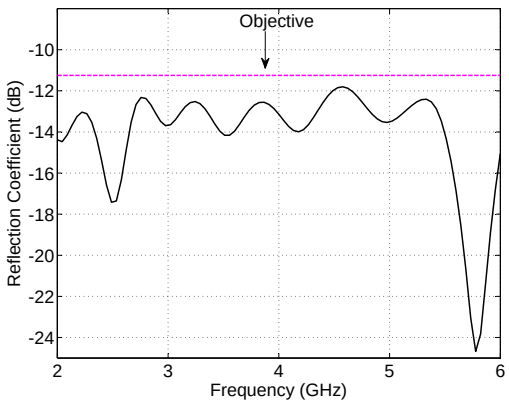

(a) Differential return loss.

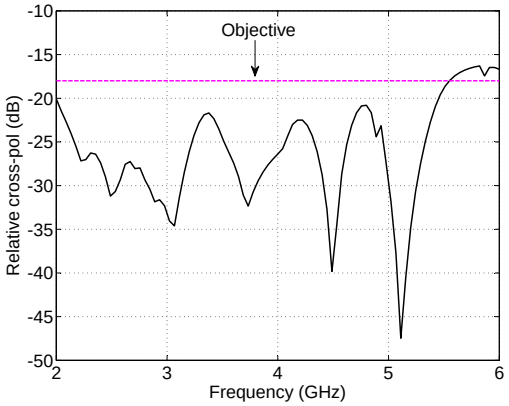

(b) Relative cross-polarisation.

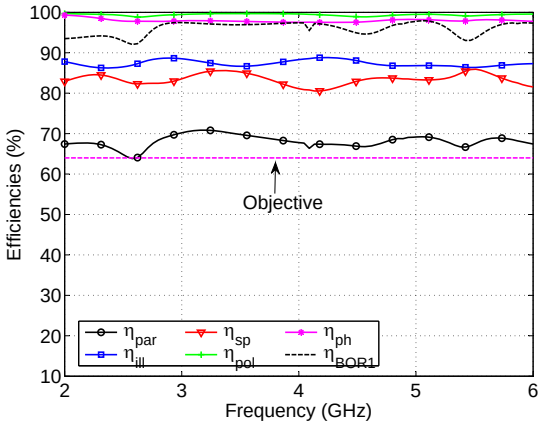

(c) Predicted efficiencies for a subtended half-angle $\theta_e = 48°$.

Figure 5.20: Optimal responses of the conical for a prime-focus paraboloid with a subtended angle $\theta_e = 48°$.

5.6.1 Sensitivity Analysis

Local sensitivity analysis is carried out on the model to be constructed, in a procedure similar to the one in section 5.3 with the exception that the optimal values in Table 5.13 are perturbed by $p = \pm 0.05$, which translates to $\theta \in \{57.33°, 55.63°\}$, $\alpha \in \{25.50°, 24.20°\}$, $\delta \in \{15.34°, 14.57°\}$ and $\tau \in \{0.845, 0.8369\}$.

Plots of response variations as a result of perturbations in optimal values are shown in Fig. 5.21, where it can clearly be seen that a one degree deviation in θ results in large deviations in return loss and relative cross-polarisation compared to the optimal response, also shown on the same graph. It is also evident from Fig. 5.21, that changes in δ affect return loss and aperture efficiency responses, especially at the high-frequency end.

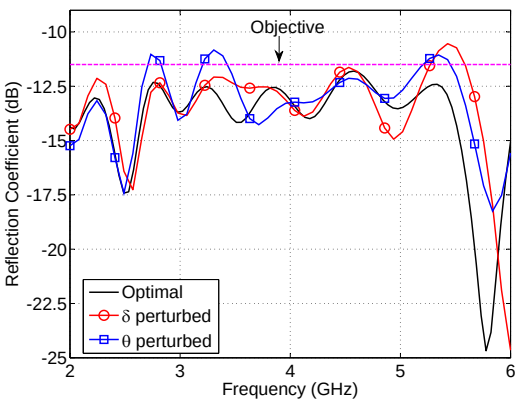

(a) Return loss deviation.

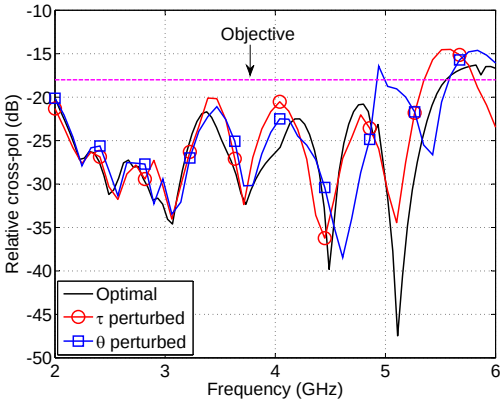

(b) Relative cross-polarisation variation.

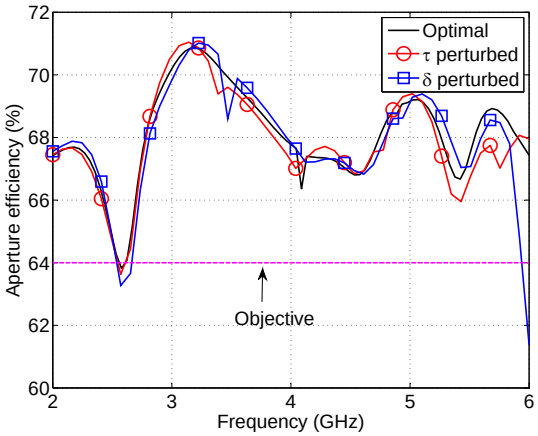

(c) Aperture efficiencies for $\theta_e = 48°$.

Figure 5.21: Worst case results for a small perturbation, $p = 0.05$, in optimal values.

Therefore, the potential sources of manufacturing problems are the conical antenna's aperture half-angle and its rotation angle with tolerances within 1° and 0.5° respectively.

5.6.2 Measurements

The antenna is etched onto a Rogers RO4003C substrate with thickness $t = 0.2032$ mm, dielectric constant $\epsilon_r = 3.38$ and loss tangent $\tan\delta = 0.0027$ while the ground plane is built on a substrate with similar dielectric properties but with thickness $t = 1.529$ mm. As

in chapter 3, a stepped impedance matching network is designed to match the antenna's differential input impedance of 300 Ω to the measurement instruments' 50 Ω.

Difficulties associated with building a conical sinuous antenna are apparent in Fig. 5.22a where the built model displays some level of interleaving between the arms, compared to the FEKO model shown in Fig. 5.22b. Also, the printed sinuous arms do not adhere to the cone's shape, especially around the feed area at the centre of the structure, with maximum deviations of about 5°, due to the substrate being very brittle in the presence of very little copper cladding.

(a) Top view of built conical sinuous antenna. (b) Top view of FEKO model.

Figure 5.22: Final model and built conical sinuous antennas.

The significant deviations from the optimised EM model resulted in severe return loss performance degradation as shown in Fig. 5.23a where a minimum return loss of about 5 dB is measured.

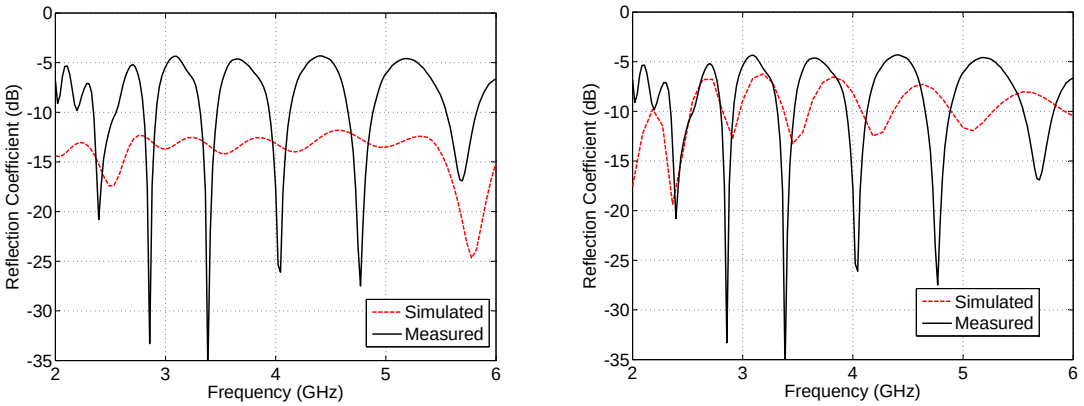

(a) (b)

Figure 5.23: Simulated and Measured differential return loss of the built conical sinuous antenna: (a) Comparison with optimised model. (b) Comparison with a simulation with added defects observed in the manufactured antenna in Fig. 5.22a.

Simulation results, of a model incorporating the observed defects in the built antenna, are shown in Fig. 5.23b, where it is evident that such defects indeed severely affect the antenna's return loss performance. It is expected from the discussion in section 5.2.3,

clearly illustrated in Fig. 5.15d, that a large deviation in the cone's taper results in severe degradation of return loss performance.

The radiation pattern performance of the built antenna is shown in Fig. 5.24 where the measured and simulated HPBW are in good agreement while the measured cross-polarisation is much higher than the simulated result.

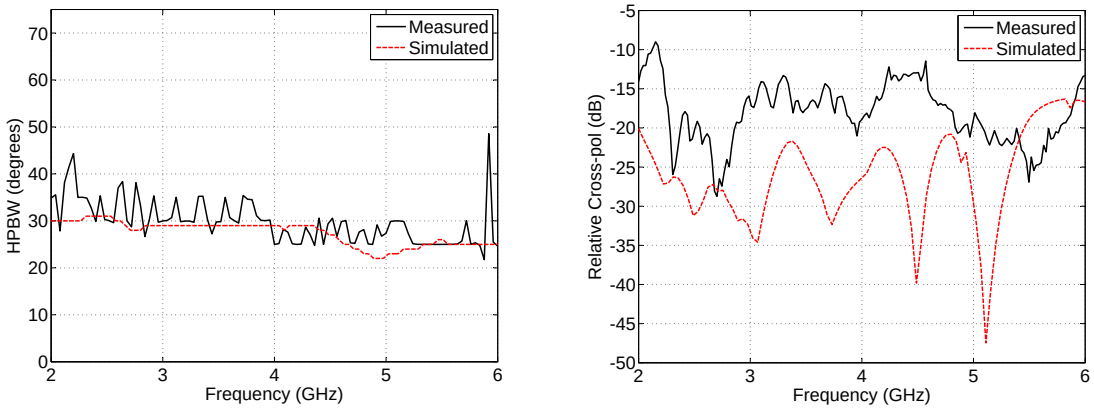

(a) HPBW. (b) Relative cross-poalrisation.

Figure 5.24: Simulated and measured radiation characteristics.

Therefore, improved construction methods are required to build an antenna that matches the performance levels of the accurate simulations presented in previous sections. Work towards this goal is currently on-going.

Chapter 6

Conclusion

> There are known knowns. These are things we know that we know. There are known unknowns. That is to say, there are things that we know we don't know. But there are also unknown unknowns. There are things we don't know we don't know.
>
> Donald Rumsfeld(US politician).

6.1 Summary of Results

An extensive study of both the planar and conical sinuous antennas has been presented in this thesis. A parametric study approach is followed in designing the planar sinuous antenna while an effective and efficient optimisation based strategy is used to study the conical antenna.

A thorough parametric study is carried out on the planar sinuous antenna, from which some design guidelines are derived for various design objectives. A planar, unidirectional sinuous antenna without absorber lining is designed, achieving a measured bandwidth of more than a $3:1$ at a return loss of 10 dB from $1.9-6.2$ GHz, representing a significant improvement over the octave bandwidth previously achieved with a similar antenna. The designed antenna features a simple and yet very effective feeding structure.

Furthermore, an efficient modelling and optimisation algorithm is developed to fully study a conical sinuous antenna. SBO-EI is used to simultaneously optimise the conical antenna for various goals and carry out design space exploration, from which various design guidelines are derived. Local sensitivity analysis is then carried out by means of perturbations around the optimal for each of the design goals considered. The developed strategy is efficient in that design space exploration, optimisation and sensitivity analysis tasks are conducted on a mathematical model of the antenna and thus rendering the mentioned tasks fast and computationally cheap compared to a case where they are performed using full-wave simulations.

A comprehensive study of the conical sinuous antenna is undertaken by optimising the antenna for various goals and establishing some performance limitations of this particular antenna.

6.2 Recommendations for Further Research

Challenges regarding the manufacturing of the conical sinuous antenna were discussed in chapter 5. A variant of the sinuous antenna that might be easier to build consists of a projection onto a pyramid such that the antenna can be assembled using planar petals, much like in the eleven feed [6]. It might be of interest to fully study and optimise such an antenna. We suspect that performances similar to the conical sinuous antenna can easily be achieved or exceeded.

The challenge of the weighted sum multi-objective optimisation carried out in chapter 5, is that the obtained optimal result is strongly dependent on the weights used. There is thus need to devise a method of determining optimal weightings for each of the goals in the aggregated cost function so as to yield a truly optimal result. Possible techniques include:

1. Run the first few iterations of the optimisation using randomised weights, within a certain range, of all goals and determine optimal settings by applying some functional constraint on one or many of the design goals.

2. Using different cost functions with different penalty levels for each of the goals and thereby reducing the effects of the weights on the aggregated cost function's optimum.

Another approach would be to use weight insensitive global optimisation algorithms such as the Non-dominated Sorting Genetic Algorithm-II (NSGA-II). This approach requires globally accurate surrogate models for each of the optimisation goals.

Feeding the dual-polarised sinuous antennas has been a major challenge in this thesis. The short distance between the antenna and the reflecting ground plane as well as the position of sinuous arms require the development/improvement of compact baluns that operate over a very wide bandwidth.

Appendices

Appendix A

Numerical Subtleties pertaining to Kriging

In this appendix, a few computational issues and remedies thereof, are discussed. First, let us consider the expression for calculating β in (4.2.17), repeated here for clarity.

$$\beta = (F^T R^{-1} F)^{-1} F^T R^{-1} Y. \tag{A.0.1}$$

(A.0.1) involves inversion of the correlation matrix R. To avoid ill-conditioning issues, the correlation matrix has a small number added to its diagonal entries. This number is equal to the *machine error* (i.e. The accuracy level of the computing engine), which in MATLAB, is given by $\epsilon = 2.2204 \times 10^{-16}$. The MATLAB command `eps` gives the machine error and thus the modified $M \times M$ correlation matrix is given by

$$R = R + D \tag{A.0.2}$$

where D is an $M \times M$ diagonal matrix with entries equal to ϵ.

Inverting the modified correlation matrix is efficiently done by means of Cholesky factorisation[1]. The MATLAB command `chol` factorises R as

$$R = UU^T \tag{A.0.3}$$

where U is an upper triangular matrix, and $R^{-1} = U^{-1}(U^T)^{-1}$. With the factorisation in mind and by using back substitution instead of matrix inversion, (A.0.1) is neatly written in MATLAB as `beta = (F'*(U\(U'\Y)))/(F'*(U\(U'\F)));` and the variance in (4.2.23) is easily calculated in a straight forward manner.

As demonstrated in chapter 4, the Best Linear Unbiased Predictor (BLUP), where the polynomial fitting functions, F, are simply made equal to a vector of *ones*, is as accurate as the more complex case. Therefore the computational complexity is even further reduced by adopting the BLUP framework to determine the Kriging model.

[1] Of course this is subject to R not being ill-conditioned. If R is ill-conditioned the matrix will have to be inverted in the traditional manner.

Bibliography

[1] D. Filipovic and T. Cencich, *Antenna Engineering Handbook*, 4th ed., J. Volakis, Ed. McGraw-Hill, 2007.

[2] P.-S. Kildal, "Factorization of the feed efficiency of paraboloids and cassegrain antennas," *IEEE Antennas and Propagation Magazine*, vol. AP-33, no. 8, pp. 903–908, August 1985.

[3] W. Huyer and A. Neumaier, "Global optimization by multilevel coordinate search," *Journal of Global Optimization*, vol. 14, pp. 331–355, 1999.

[4] SKA Telescope Speficications. [Online]. Available: http://www.skatelescope.org

[5] J. Jonas, "MeerKAT-the South African array with composite dishes and wide-band single pixel feeds," *Proceedings of the IEEE*, vol. 97, no. 8, pp. 1522 –1530, aug. 2009.

[6] J. Yang, M. Pantaleev, P.-S. Kildal, B. Klein, Y. Karandikar, L. Helldner, N. Wadefalk, and C. Beaudoin, "Cryogenic $2-13$ GHz eleven feed for reflector antennas in future wideband radio telescopes," *Antennas and Propagation, IEEE Transactions on*, vol. 59, no. 6, pp. 1918–1934, 2011.

[7] G. Cortes-Medellin, "Non-planar quasi-self-complementary ultra-wideband feed antenna," *Antennas and Propagation, IEEE Transactions on*, vol. 59, no. 6, pp. 1935–1944, 2011.

[8] G. Engargiola and W. J. Welch, "Log-periodic antenna," U.S. Patent 6 677 913, January, 2004.

[9] R. Gawande and R. Bradley, "Towards an ultra wideband low noise active sinuous feed for next generation radio telescopes," *Antennas and Propagation, IEEE Transactions on*, vol. 59, no. 6, pp. 1945 –1953, june 2011.

[10] A. H. Akgiray, "New technologies driving decade bandwidth radio astronomy: quad-ridge flared horn and compound semiconductor LNAs," Ph.D. dissertation, California Institute of Technology (Caltech), 2013.

[11] N. Mutonkole and D. I. L. de Villiers, "A 3:1 bandwidth planar, lossless cavity sinuous antenna for reflector feed applications." in *IEEE Africa Conference (AFRICON)*, September 2013, pp. 1–5.

[12] R. H. DuHamel, "Dual polarized sinuous antennas," U.S. Patent 4 658 262, April, 1987.

[13] V. H. Rumsey, "Frequency independent antennas," *IRE National Convention Record*, vol. 1, pp. pp. 114–118, March 1957.

[14] C. Balanis, *Antenna Theory: Analysis and Design*. Wiley - Interscience, 2005.

[15] Y. Mushiake, "The input impedance of a slit antenna," *Joint Convention of Tohoku Section of IEE and IECE of Japan*, pp. 25–26, 1948.

[16] M. C. Buck and D. S. Filipovic, "Two-arm sinuous antennas," *IEEE Transactions on Antennas and Propagation*, vol. 56, no. 5, pp. 1229–1235, May 2008.

[17] S. Lizhong, C. Guojin, and H. Huanfeng, "Simulation and analysis of a hemispherical conformal sinuous antenna with four arms," in *Ultra-Wideband (ICUWB), 2010 IEEE International Conference on*, vol. 1, sept. 2010, pp. 1 –4.

[18] M. Vahdani and X. Begaud, "A directive ultra wideband sinuous slot antenna," in *Antennas and Propagation, 2006. EuCAP 2006. First European Conference on*, nov. 2006, pp. 1 –6.

[19] A. Manna, P. Baldonero, and F. Trotta, "Novel UWB low-profile sinuous slot antenna," in *Antennas and Propagation (EUCAP), Proceedings of the 5th European Conference on*, april 2011, pp. 783 –786.

[20] M. Buck and D. Filipovic, "Split-beam mode four-arm slot sinuous antenna," *Antennas and Wireless Propagation Letters, IEEE*, vol. 3, no. 1, pp. 83 –86, dec. 2004.

[21] H. Booker, "Slot aerials and their relation to complementary wire aerials (babinet's principle)," *Electrical Engineers - Part IIIA: Radiolocation, Journal of the Institution of*, vol. 93, no. 4, pp. 620 –626, 1946.

[22] C. A. Balanis, *Advanced Engineering Electromagnetics*. John Wiley & Sons, Inc., 1989.

[23] J. Yang, S. Pivnenko, and P.-S. Kildal, "Comparison of two decade-bandwidth feeds for reflector antennas: The eleven antenna and quadridge horn," in *Antennas and Propagation (EuCAP), 2010 Proceedings of the Fourth European Conference on*, april 2010, pp. 1 –5.

[24] P.-S. Kildal and Z. Sipus, "Classification of rotationally symmetric antennas as types BOR-0 and BOR-1," *IEEE Antennas and Propagation Magazine*, vol. 37, no. 6, pp. 114–117, December 1995.

[25] A. Ludwig, "The definition of cross polarization," *Antennas and Propagation, IEEE Transactions on*, vol. 21, no. 1, pp. 116 – 119, jan 1973.

[26] D. I. L. de Villiers, "Offset dual-reflector antenna system efficiency predictions including subreflector diffraction," *Antennas and Wireless Propagation Letters, IEEE*, vol. 10, pp. 947 –950, 2011.

[27] FEKO. EM Software & Systems (Pty) Ltd. Stellenbosch, South Africa. [Online]. Available: www.feko.info

[28] Sinuous Antennas. L3 Communications: Randtron Antenna Systems. Menlo Park, California 94025. [Online]. Available: http://www.l-3com.com/randtron/dcpantenna.htm

[29] A. Jafargholi and M. Kamyab, "A new approach for feeding sinuous antenna," *International Journal of Electronics and Communications*, vol. 65, pp. 312–319, 2011.

[30] Y. Mushiake, "Self-complementary antennas," *IEEE Antennas and Propagation Magazine*, vol. 34, pp. 23–29, December 1992.

[31] D. I. L. de Villiers and R. Lehmensiek, "Sub-reflector extensions for reduced noise temperature in low-side sub-reflector offset Gregorian systems," in *Antennas and Propagation (EUCAP), 2012 6th European Conference on*, march 2012, pp. 3438 –3441.

[32] W. Fan, A. Lu, L. Wai, and B. Lok, "Mixed-mode S-parameter characterization of differential structures," in *Electronics Packaging Technology, 2003 5th Conference (EPTC 2003)*, 2003, pp. 533–537.

[33] ETI Industries. 180 degree hybrid coupler, J-28-180. [Online]. Available: www.etiworld.com

[34] D. S. Prinsloo, P. Meyer, R. Maaskant, and M. V. Ivashina, "Design of an active dual-mode antenna with near hemispherical field of view coverage," in *International Conference on Electromagnetics in Advanced Applications (ICEAA), Turin, Italy*, September 2013, pp. 1064–1067.

[35] D. M. Pozar, *Microwave engineering*, 3rd, Ed. John Wiley and Sons., 2005.

[36] GRASP. TICRA. Copenhagen, Denmark. [Online]. Available: www.ticra.com

[37] D. I. L. de Villiers and R. Lehmensiek, "Efficient simulation of radiometric noise in offset Gregorian antenna systems," in *European Conference on Antennas and Propagation (EuCAP)*, 2013, pp. 3357–3359.

[38] I. Couckuyt, F. Declercq, T. Dhaene, H. Rogier, and L. Knockaert, "Surrogate-based infill optimization applied to electromagnetic problems," *International Journal of RF and Microwave Computer-Aided Engineering*, vol. 20, no. 5, pp. 492–501, 2010. [Online]. Available: http://dx.doi.org/10.1002/mmce.20455

[39] M. Bakr, J. Bandler, K. Madsen, and J. Sondergaard, "An introduction to the space mapping technique," *Optimization and Engineering*, vol. 2, no. 4, pp. 369–384, 2001.

[40] J. Bandler, R. Biernacki, S. H. Chen, P. Grobelny, and R. Hemmers, "Space mapping technique for electromagnetic optimization," *Microwave Theory and Techniques, IEEE Transactions on*, vol. 42, no. 12, pp. 2536–2544, 1994.

[41] J. Zhu, J. Bandler, N. Nikolova, and S. Koziel, "Antenna optimization through space mapping," *Antennas and Propagation, IEEE Transactions on*, vol. 55, no. 3, pp. 651–658, 2007.

[42] R. Lehmensiek and P. Meyer, "Creating accurate multivariate rational interpolation models of microwave circuits by using efficient adaptive sampling to minimize the number of computational electromagnetic analyses," *Microwave Theory and Techniques, IEEE Transactions on*, vol. 49, no. 8, pp. 1419–1430, 2001.

[43] D. G. Krige, "A statistical approach to some mine evaluations and allied problems at the Witwatersrand," Master's thesis, University of Witwatersrand, Johannesburg, South Africa., 1951.

[44] E. S. Siah, M. Sasena, J. Volakis, P. Papalambros, and R. Wiese, "Fast parameter optimization of large-scale electromagnetic objects using direct with kriging metamodeling," *Microwave Theory and Techniques, IEEE Transactions on*, vol. 52, no. 1, pp. 276–285, 2004.

[45] H.-M. Gutmann, "A radial basis function method for global optimization," *Journal of Global Optimization*, vol. 19, pp. 201–227, 2001.

[46] J. Rayas-Sanchez, "EM-based optimization of microwave circuits using artificial neural networks: the state-of-the-art," *Microwave Theory and Techniques, IEEE Transactions on*, vol. 52, no. 1, pp. 420–435, 2004.

[47] Y. Nan, W. Ming, and C. Xiang, "Support vector machine in application of modeling of electromagnetic pulse field coupling on electronic devices," in *Signal Processing Systems (ICSPS), 2010 2nd International Conference on*, vol. 3, 2010, pp. V3–230–V3–233.

[48] D. Gorissen, "Grid-enabled adaptive surrogate modeling for computer aided engineering," Ph.D. dissertation, Ghent University, Ghent, Belgium, 2010.

[49] G. Matheron, "Principles of geostatistics," *Economic Geology*, vol. 58, pp. 1246–1266, 1963.

[50] L. Lebensztajn, C. Marretto, M. Costa, and J. L. Coulomb, "Kriging: a useful tool for electromagnetic device optimization," *Magnetics, IEEE Transactions on*, vol. 40, no. 2, pp. 1196–1199, 2004.

[51] DACE: A MATLAB Kriging Toolbox. [Online]. Available: http://www2.imm.dtu.dk/~hbni/dace/

[52] Lecture notes on Karush-Kuhn-Tucker conditions for optimality of a solution. [Online]. Available: http://myweb.clemson.edu/~pbelott/bulk/teaching/lehigh/ie426-f09//lecture20.pdf

[53] D. Jones, M. Schonlau, and W. Welch, "Efficient global optimisation of expensive black-box functions," *Journal of Global Optimization*, vol. 13, pp. 455–492, 1998.

[54] A. Forrester, A. Sobester, and A. Keane, *Engineering Design via Surrogate Modelling: A Practical Guide*. Wiley, 2008.

[55] A. Arkko and J. Rahola, "On the optimization of mobile terminal antenna isolation using the genetic algorithm technique," in *Antennas and Propagation, 2007. EuCAP 2007. The Second European Conference on*, 2007, pp. 1–6.

[56] R. Hassan, B. E. Cohanim, and O. L. de Weck, "Comparison of particle swarm optimization and the genetic algorithm," in *46th AIAA/ASME/ASCE/AHS/ASC Structures, Structural Dynamics, and Materials Conference*, no. AIAA-2005-1897. Austin, Texas: American Institute of Aeronautics and Astronautics, April 18-21 2005.

[57] I. Couckuyt, D. Deschrijver, and T. Dhaene, "Towards efficient multiobjective optimization: Multiobjective statistical criterions," in *Evolutionary Computation (CEC), 2012 IEEE Congress on*, 2012, pp. 1–8.

[58] C. Gazda, H. Rogier, D. Vande Ginste, I. Couckuyt, and T. Dhaene, "Time domain analysis of a common-mode suppression filter subjected to a multi-objective optimization," in *Electromagnetic Compatibility (EMC EUROPE), 2012 International Symposium on*, 2012, pp. 1–6.